

Ultraviolet Radiation Fields in Star-Forming Disk Galaxies: Numerical Simulations with TIGRESS-NCR

NORA B. LINZER,¹ JEONG-GYU KIM,^{2,3,1} CHANG-GOO KIM,¹ AND EVE C. OSTRIKER^{1,4}

¹*Department of Astrophysical Sciences, Princeton University, 4 Ivy Lane, Princeton, NJ 08544, USA*

²*Division of Science, National Astronomical Observatory of Japan, Mitaka, Tokyo 181-0015, Japan*

³*Korea Astronomy and Space Science Institute, Daejeon 34055, Republic of Korea*

⁴*Institute for Advanced Study, 1 Einstein Drive, Princeton, NJ 08540, USA*

ABSTRACT

With numerical simulations that employ adaptive ray-tracing (ART) for radiative transfer at the same time as evolving gas magnetohydrodynamics, thermodynamics, and photochemistry, it is possible to obtain a high resolution view of ultraviolet (UV) fields and their effects in realistic models of the multiphase interstellar medium. Here, we analyze results from TIGRESS-NCR simulations, which follow both far-UV (FUV) wavelengths, important for photoelectric heating and PAH excitation, and the Lyman continuum (LyC), which photoionizes hydrogen. Considering two models, representing solar neighborhood and inner galaxy conditions, we characterize the spatial distribution and time variation of UV radiation fields, and quantify their correlations with gas. We compare four approximate models for the FUV to simulated values to evaluate alternatives when full ART is infeasible. By convolving FUV radiation with density, we produce mock maps of dust emission. We introduce a method to calibrate mid-IR observations, for example from JWST, to obtain high resolution gas surface density maps. We then consider the LyC radiation field, finding most of the gas exposed to this radiation to be in ionization-recombination equilibrium and to have a low neutral fraction. Additionally, we characterize the ionization parameter as a function of environment. Using a simplified model of the LyC radiation field, we produce synthetic maps of emission measure (EM). We show that the simplified model can be used to extract an estimate of the neutral fraction of the photoionized gas and mean free path of ionizing radiation from observed EM maps in galaxies.

1. INTRODUCTION

Ultraviolet (UV) radiation from young stars represents the largest energy input to the interstellar medium (ISM), exceeding that from supernovae (SNe) by a factor of ~ 100 (e.g. [Leitherer et al. 1999](#); [Kim et al. 2023b](#)). This radiation directly affects the physical state of the ISM, notably by heating and ionizing the gas, and produces observational diagnostics in both gas and dust. Because radiation fields vary in time and space ([Parravano et al. 2003](#)), it is important to include a time-dependent treatment of radiation in numerical ISM simulations.

Far-UV (FUV) radiation is critical to gas thermodynamics, with the equilibrium thermal pressure P_{th} in diffuse, neutral gas proportional to the FUV radiation field through photoelectric (PE) heating (e.g. [Bakes & Tielens 1994](#); [Wolfire et al. 1995, 2003](#); [Herrera-Camus](#)

[et al. 2017](#)); this relationship is key to the feedback loop that self-regulates star formation on large scales ([Ostriker et al. 2010](#)). Lyman continuum (LyC) radiation contributes to the dynamical state of the ISM since ionized gas pressure forces from this “early feedback” are believed to destroy most of the self-gravitating clouds where star formation occurs, with radiation pressure on dust becoming more important in the highest density clouds (e.g. [Whitworth 1979](#); [Krumholz & Matzner 2009](#); [Sales et al. 2014](#); [Kim et al. 2016, 2018](#); [Krumholz et al. 2019](#); [Chevance et al. 2023](#); [Menon et al. 2024](#)).

The inclusion of radiation modeling in numerical simulations enables more realistic thermodynamics in a variety of environments where heating and cooling depend on both the radiation itself and the properties of the gas that are sensitive to radiation, such as the chemical and ionic state. In addition to enabling realistic thermodynamic and dynamic responses to stellar feedback, inclusion of radiation makes it possible to create synthetic observables that depend on radiation heating and photochemical reactions, including dust emission.

Only very recently has time-dependent modeling begun to include radiative transfer to follow spatial variations in the FUV and LyC radiation intensities. Many simulations employ approximate radiative transfer treatments such as two-moment/M1 or tree-based methods (e.g. Skinner & Ostriker 2013; Rosdahl et al. 2013; Rosdahl & Teyssier 2015; Kannan et al. 2019; Melon Fuksman & Mignone 2019; Fukushima & Yajima 2021; Wunsch et al. 2021; Wibking & Krumholz 2022; Grudić et al. 2022; Klepitko et al. 2023; Wadsley et al. 2024). Approximate methods are often sufficient for treating FUV radiation (see comparisons of the two-moment implementation of Skinner & Ostriker 2013 with ray-tracing in Kim et al. 2017). However, given the short mean free path $\ell \sim 0.1 \text{ pc}(n_{\text{H}}/\text{cm}^{-3})^{-1}$ for LyC radiation, and corresponding exponential attenuation at optical depth $\tau > 1$, methods with high spatial and angular resolution are crucial to an accurate solution for ionizing radiation. Methods that allow both high spatial and high angular resolution include Monte Carlo (e.g. Harries et al. 2019), variable Eddington tensor (e.g. Jiang et al. 2012; Menon et al. 2022), and adaptive ray tracing (e.g. Abel & Wandelt 2002; Rosen et al. 2017; Kim et al. 2017).

The implementation by Kim et al. (2017) of adaptive ray tracing (ART) in *Athena* has made it possible, for the first time, to follow radiative transfer with very high angular resolution at the same spatial resolution as MHD, at manageable computational cost. The ART solver was first applied to study giant molecular cloud (GMC) evolution under feedback (Kim et al. 2018, 2019, 2021), and subsequently adapted to study the large-scale multiphase ISM with disk geometry and sheared rotation using the TIGRESS framework (Kim & Ostriker 2017; Kim et al. 2023a). This new implementation is now being applied in an extensive simulation survey to study the dependence of star formation regulation under varying metallicity and environmental conditions (Kim et al. 2024).

The multiphase disk simulations presented in Kim et al. (2023a) are similar in their environmental conditions to the Milky Way and other nearby star-forming galaxies. With these simulation results in hand, it is of interest to explore, for the first time, the detailed properties of the FUV and LyC radiation fields. This analysis of radiation fields, for two simulation runs, is the subject of the present paper.

We first summarize the ray-tracing methods used to evolve the UV radiation fields, and the model parameters for the two simulations we will explore (Section 2). In Section 3 we provide an overview of the gas and radiation properties in both simulations. We quantify the

statistical properties of the FUV radiation field in Section 4. In addition, Section 4 compares the simulated FUV radiation field to different approximate models, evaluating them for potential usage as inexpensive alternatives to full radiative transfer. These approximate treatments include (1) the analytic slab model from Ostriker et al. (2010) that was adopted for setting the heating rate in Kim et al. (2020), (2) a plane-parallel model, (3) an analytic model from Bialy (2020), and (4) an estimate of the radiation field taken from a sum over FUV source particles. The FUV radiation field produces IR emission through dust reprocessing (including spectral features due to small grains – Li & Draine 2001; Tielens 2008), so we also use our simulated results to characterize properties of the dust heating rate. We explore potential usage of approximate radiation field models in calibrating PAH emission maps (such as those from *JWST*, e.g. Leroy et al. 2023; Pathak et al. 2023), in order to improve measurement of the gas surface density. Finally, in Section 5, we examine the LyC radiation field and how it directly affects the ionization state of the gas. We present statistics of the radiation field itself and of the ionization parameter. We also consider an approximate model for the LyC radiation on large scales inspired by the model explored in Belfiore et al. (2022). Our main conclusions are summarized in Section 6.

2. NUMERICAL METHODS AND MODELS

This paper focuses on the UV radiation properties from the TIGRESS-NCR simulations for two galactic conditions presented in Kim et al. (2023a). TIGRESS-NCR is an extension of the “TIGRESS-classic” numerical framework (Kim & Ostriker 2017) for modeling local patches of vertically stratified, multiphase ISM disks with resolved star formation and feedback. The methodological enhancements are in the treatment of ISM photochemistry and thermodynamics based on Gong et al. (2017), coupled to explicit UV radiation transfer via the ART method of Kim et al. (2017). This enables us to explicitly model all major phases of the ISM and the UV radiation fields permeating them. Kim et al. (2023b) describe photochemistry in determining time-dependent hydrogen and equilibrium C and O bearing species abundances from which we calculate cooling and heating rates. Kim et al. (2023a) explain physics modules and their numerical algorithms as employed in the TIGRESS-NCR simulations. We refer interested readers to these papers. Here, we summarize the technical details regarding UV radiation that are most relevant to this paper.

2.1. Radiation Transfer Methods

In the TIGRESS-NCR simulations, we evaluate the UV radiation field from luminous point sources (representing star clusters) via ray-tracing. We track three frequency bins: (1) Lyman continuum (LyC) band ($\lambda < 912 \text{ \AA}$) for hydrogen photoionization; (2) Lyman-Werner (LW) band ($912 \text{ \AA} \leq \lambda < 1108 \text{ \AA}$) for H_2 dissociation, C ionization, and grain photoelectric heating; and (3) photoelectric (PE) band ($1108 \text{ \AA} \leq \lambda < 2066 \text{ \AA}$) for grain photoelectric heating. When applied to our simulations, we use “FUV” to refer to the combined PE and LW bands. The input luminosities for these bands from each star cluster particle as a function of age (t_{age}) is determined using Starburst99 (Leitherer et al. 2014; see also Fig 21 in Kim et al. 2023b). Although star cluster particles are active SN hosts for $t_{\text{age}} = 40 \text{ Myr}$, $\sim 90\%$ of the FUV (PE+LW) radiation and essentially all of the LyC radiation are from star clusters younger than 20 Myr. We thus only consider particles with $t_{\text{age}} < 20 \text{ Myr}$ as UV radiation sources to save the computational expense of ray tracing.

Our radiative transfer method tracks frequency-dependent dust and gas absorption (see Appendix B of Kim et al. 2023b, for crosssections), neglecting scattering. In particular, the LyC band is subject to dust absorption and photoionization of atomic and molecular hydrogen; the LW band is subject to dust absorption and photodissociation of H_2 , accounting for self-shielding along rays following Draine & Bertoldi (1996); the PE band is subject to dust absorption.

We adopt $\sigma_{\text{pi,H}} = 3 \times 10^{-18} \text{ cm}^2$ for the SED-averaged H photoionization cross section in the LyC band. The dust absorption cross sections per H are $\sigma_{\text{d}}/(10^{-21} \text{ cm}^2) = (1, 2, 1)$ for the (LyC, LW, PE) bands. In the LW and PE bands, these values are appropriate for dust grains characteristic of the local diffuse ISM (see Table 3 in Kim et al. 2023b). The value in the LyC band is somewhat lower than the estimate based on a theoretical extinction model (Weingartner & Draine 2001a). It should be noted, however, that the dust opacity (and other grain properties) in photoionized gas remains uncertain as grains may suffer collisional- and photo-destruction (Micelotta et al. 2010; Chastenot et al. 2019; Egorov et al. 2023) and rotational disruption (Hoang et al. 2019) in regions with intense UV radiation fields.

2.1.1. Adaptive Ray Tracing

We solve for UV radiation transfer using the ART module implemented in *Athena* (Kim et al. 2017). Given information about the location and luminosity of point sources, photon packets are injected along rays at the location of each source and transported radially outward. The direction of ray propagation is determined by the

HEALPix scheme (Górski et al. 2005), which divides a unit sphere into $12 \times 4^\ell$ equal-area pixels at HEALPix level ℓ . We adopt an initial HEALPix level of $\ell_0 = 4$. A minimum angular resolution of four rays per grid cell per source is maintained by dividing a ray into four sub-rays if the distance from the source becomes greater than $d_{\text{max}}(\ell) = [3/(4\pi)]^{1/2} 2^\ell \Delta x$, where Δx is the grid resolution. As photon packets propagate through the grid, they interact with each intersecting cell based on physical properties of the dusty gas (density; species abundance of H and H_2) and the path length of the ray through the cell. Accordingly, the optical depth through each grid cell and the volume-averaged radiation energy density (\mathcal{E}) and flux (\mathbf{F}) are computed. These in turn are used to evaluate photochemical and photoheating rates and radiation pressure forces.

We apply shearing-periodic boundary conditions to rays crossing horizontal boundaries. For rays crossing the \hat{x} (radial) boundaries, their y -position and source position are shifted by appropriate shear displacement, while the periodic boundary condition is applied to rays crossing the \hat{y} (azimuthal) boundaries.

To alleviate the high computational cost of radiative transfer, we do not perform ray tracing every MHD time step, which is determined by the Courant–Friedrichs–Lewy (CFL) condition for the hot phase. The fastest wave speed in the hot phase can exceed $> 1000 \text{ km s}^{-1}$ easily. Rather, we perform ray tracing at intervals determined by the CFL condition for the cold and warm phases with $T < 2 \times 10^4 \text{ K}$, whose maximum speed remains $\sim 100 \text{ km s}^{-1}$. This choice is justified by the fact that UV radiation has little interaction with the hot gas.

As described in Kim et al. (2023a), we employ the following ray termination conditions:

- (1a) A ray hits the vertical boundaries
- (1b) The horizontal distance travelled from the source becomes larger than $d_{xy,\text{max}}$
- (2a) (FUV only) The ratio between the photon packet luminosity and the total source luminosity in the computational domain falls below a small number ϵ_{PP}
- (2b) (FUV only) A ray in the FUV band is terminated if $|z| > z_{\text{p-p}}$, where $z_{\text{p-p}}$ is the height beyond which the plane-parallel approximation is used (described in Section 2.1.2)
- (3) The optical depth from the source becomes larger than 20.

The adopted values of the termination parameters are summarized in Table 1. We stop following a ray com-

pletely if the condition (1a) or (1b) is met or if photons in all bands are used up, satisfying (2a) or (2b) for FUV and (3) for LyC¹.

By adopting the conditions (1b) and (2a), we ignore contributions to UV radiation fields from distant and/or faint sources. This helps to reduce the cost of ART without significantly reducing its accuracy. A significant fraction of rays are completely terminated before reaching $z = \pm z_{\text{p-p}}$, because both LyC and FUV photons are exhausted by the conditions (3) and (2b), respectively. This further helps to reduce the computational cost of ART.

2.1.2. Plane Parallel Approximation

We adopt the plane-parallel radiative transfer solution for the FUV (PE and LW) band in high-altitude regions with $|z| > z_{\text{p-p}}$ (see Appendix A.1 in Kim et al. 2023a). Whenever a ray reaches the height $z_{\text{p-p}} > 0$ from below, we collect its luminosity as a function of the cosine angle $\mu = \hat{\mathbf{k}} \cdot \hat{\mathbf{z}} > 0$, where $\hat{\mathbf{k}}$ and $\hat{\mathbf{z}}$ are unit vectors along the ray propagation direction and z -axis, respectively. These are used to calculate the area-averaged mean intensity $\langle I \rangle(\mu; z_{\text{p-p}})$ at $z_{\text{p-p}}$ as a function of μ (assuming symmetry of the intensity about the z -axis). The area-averaged radiation energy density and the vertical component of radiation flux at $z > z_{\text{p-p}}$ can then be obtained as

$$\langle \mathcal{E}_{\text{p-p}} \rangle(z) = (2\pi/c) \int_{-1}^1 \langle I \rangle(\mu; z_{\text{p-p}}) e^{-\Delta\tau/\mu} d\mu \quad (1)$$

$$\langle F_{z,\text{p-p}} \rangle(z) = 2\pi \int_{-1}^1 \langle I \rangle(\mu; z_{\text{p-p}}) e^{-\Delta\tau/\mu} \mu d\mu. \quad (2)$$

Here $\Delta\tau(z; z_{\text{p-p}})$ is the area-averaged vertical dust optical depth from $z_{\text{p-p}}$ to z . In evaluating $\langle I \rangle(\mu; z_{\text{p-p}})$ and Equations (1) and (2), we discretize μ uniformly into 64 bins. A similar calculation is done for the high-altitude region below the midplane ($z < -z_{\text{p-p}}$).

We note that a small fraction of rays with non-zero FUV luminosity are terminated before reaching $z_{\text{p-p}}$ by conditions (1b) and (2a). Due to these “lost” photons, our approach somewhat underestimates the true plane-parallel solution by ~ 10 – 15% . We also note that the LyC radiation field is still followed with the ART, to the extent that the restrictions imposed by termination conditions (1b) and (3) allow.

2.2. Simulation Physical and Numerical Parameters

¹ In practice, the condition (3) is hardly met for FUV photons, since the dust optical depth through the computational domain is order unity along most directions.

We analyze the two simulations presented in Kim et al. (2023a): R8-4pc and LGR4-2pc. The key simulation parameters for these models are listed in Table 1 (for full information see Table 1 in Kim et al. 2023a). We analyze ~ 200 snapshots in the time range 250–450 Myr (R8-4pc) and 250–350 Myr (LGR4-2pc), during which star formation/feedback cycles and the ISM multiphase structure are generated self-consistently. These time ranges are used for all time-averaged quantities. The average gas surface densities over these time intervals are $11 M_{\odot} \text{pc}^{-2}$ and $38 M_{\odot} \text{pc}^{-2}$. These values roughly correspond to the area-averaged and molecular mass-weighted conditions representative of nearby star-forming galaxies studies by the PHANGS survey (Sun et al. 2022), which also roughly correspond to the solar neighborhood (R8-4pc) and an inner-galaxy environment (LGR4-2pc). The grid spacing is uniform and is $\Delta x = 4 \text{ pc}$ and 2 pc for R8-4pc and LGR-2pc, respectively.

Columns (6)–(10) in Table 1 give box sizes and parameters for ray termination. The full region extends to $z = \pm 3072 \text{ pc}$ for the R8-4pc simulation, and $z = \pm 1536 \text{ pc}$ for LGR4-2pc. Kim et al. (2023a) performed a convergence test of radiation fields with respect to $d_{xy,\text{max}}$ and ϵ_{pp} for models (R8-8pc and LGR4-4pc). From that test, the midplane mean radiation energy density in both LyC and FUV bands exhibit converging trend when $d_{xy,\text{max}} \gtrsim L_x$ and $\epsilon_{\text{pp}} \lesssim 10^{-8}$ (Fig 14 in Kim et al. 2023a).

3. SIMULATION OVERVIEW

In this section, we provide an overview of the properties of the gas and radiation field. We include snapshots illustrating the morphology and physical relationship of the gas components and UV radiation fields; horizontally-averaged vertical profiles of both gas and radiation; and temporal histories and statistics of key physical parameters. The results we present here highlight the similarities and differences when compared to the radiation field and ionization state of gas from the post-processing ray-tracing results of the TIGRESS-classic solar neighborhood model (Kado-Fong et al. 2020).

3.1. Morphology of Gas Components and UV Radiation Fields

We present individual snapshots of the R8-4pc and LGR4-2pc TIGRESS-NCR simulations in Figure 1–Figure 4 at times of 430 and 298 Myr, respectively. Figure 1 and Figure 2 show vertical slices at either $y = 200$ or 0 pc limited to a region within 1500 and 750 pc of the midplane ($z = 0$) respectively. Figure 3 and Figure 4 present horizontal snapshots in the x-y plane at $z = 0$.

Table 1. Simulation Parameters

Model	R_0	$\Sigma_{\text{gas},0}$	Σ_*	z_*	L_x, L_y	L_z	$d_{xy,\text{max}}$	ϵ_{PP}	$z_{\text{p-p}}$
	(kpc)	($M_\odot \text{pc}^{-2}$)	($M_\odot \text{pc}^{-2}$)	(pc)	(pc)	(pc)	(pc)		(pc)
(1)	(2)	(3)	(4)	(5)	(6)	(7)	(8)	(9)	(10)
R8-4pc	8	12	42	245	1024	6144	2048	10^{-8}	300
LGR4-2pc	4	50	50	500	512	3072	1024	10^{-8}	300

NOTE— Column (1): model name with spatial resolution. Column (2): nominal galactocentric radius. Column (3): initial gas surface density. Column (4): stellar surface density. Column (5): scale height of the stellar disk. Column (6): horizontal box size. Column (7): vertical box size. Column (8): maximum horizontal distance from the source for ray termination. Column (9): fractional photon packet luminosity relative to the source luminosity for ray termination (FUV only). Column (10): height at which FUV photons are collected and above which the plane-parallel radiative transfer solution is applied.

From left to right (and from top to bottom for [Figure 3](#) and [Figure 4](#)), the panels present the ISM phases, fractional abundance of free electrons (x_e)², gas temperature (T), number density of hydrogen (n_{H}), FUV energy density (\mathcal{E}_{FUV}), and LyC energy density (\mathcal{E}_{LyC}). Additionally, locations of radiation source particles (clusters) are shown in the LyC panel as circles.

We focus on the vertical slices first then take a closer look at the midplane structure using the horizontal slices.

Gas Phases—The ISM can be divided into distinct gas phases as determined by the temperature and ionization state of hydrogen. For this analysis, we define four phases as given in [Table 2](#). These include the cold medium and unstable medium (we group this as C+U here), warm neutral medium (WNM), warm ionized medium (WIM), and hot ionized gas (hot). Each cell in the simulation can be divided into one of these four phases, as shown in the first panel of each snapshot. We note that this is a simplified categorization compared to our analysis of the same simulations as presented in [Kim et al. \(2023a\)](#).

The R8-4pc and LGR4-2pc models present similar phase structure. The coldest gas (C+U) is in high density structures found near the midplane, with the majority of the volume within 500 pc of the midplane filled by WNM. Within the WNM are pockets of both hot and WIM gas. The WNM and hot gas are separated by a layer of WIM, of varying thickness. Most of the extraplanar region is filled with hot gas.

Electron Abundance—The second panel of each snapshot shows the electron abundance ($x_e = n_e/n_{\text{H}}$) of the gas. A red contour representing the separation between the hot and WIM phases is also included in this panel. In the WIM phase, $x_e \sim 1$ due to electrons from nearly completely ionized hydrogen, while $x_e \sim 1.2$ in the hot phase due to additional contributions from collisionally ionized helium and metals.³ The WNM and C+U phases are mostly neutral, where the majority of the gas has $x_e \sim 0.1$ and < 0.01 , respectively.

Comparing the first and second panels in [Figure 1](#) and [Figure 2](#), we see that there is a sharp drop in ionization between the WIM and WNM near the midplane, but for higher-altitude gas the ionization transition can be more gradual. The reason for this difference is that the mean free path for LyC photons to photoionize neutral gas becomes very short, $\ell = (n_{\text{H}}\sigma_{\text{pi}})^{-1} = 0.1 \text{ pc } (n_{\text{H}}/1 \text{ cm}^{-3})^{-1}$, at densities comparable to those found in midplane regions, but is longer for lower density, extraplanar gas. Additionally, the recombination timescale $t_{\text{rec}} = (\alpha_{\text{B}}n_e)^{-1} \sim 1 \text{ Myr } (n_e/0.1 \text{ cm}^{-3})^{-1}$ becomes longer at the lower densities that are present at high altitude (see the fourth panel). When this timescale is longer than the dynamical time, gas that is intermittently exposed to radiation (as is often the case – see below) may remain in a partially-ionized state (bright blue). The time-dependent treatment of ionization/recombination and ray-tracing allows us to recover this partially-ionized, low-density gas. We note that this is a new capability of the current simulations compared

² We define the fractional abundance of species s relative to hydrogen nuclei as $x_s = n_s/n_{\text{H}}$ where n_s denotes the number density of species s .

³ Our model assumes collisional ionization equilibrium for helium and metals as a function of temperature in the hot gas. Most helium becomes doubly ionized above $T \sim 10^5 \text{ K}$ by collisional ionization alone.

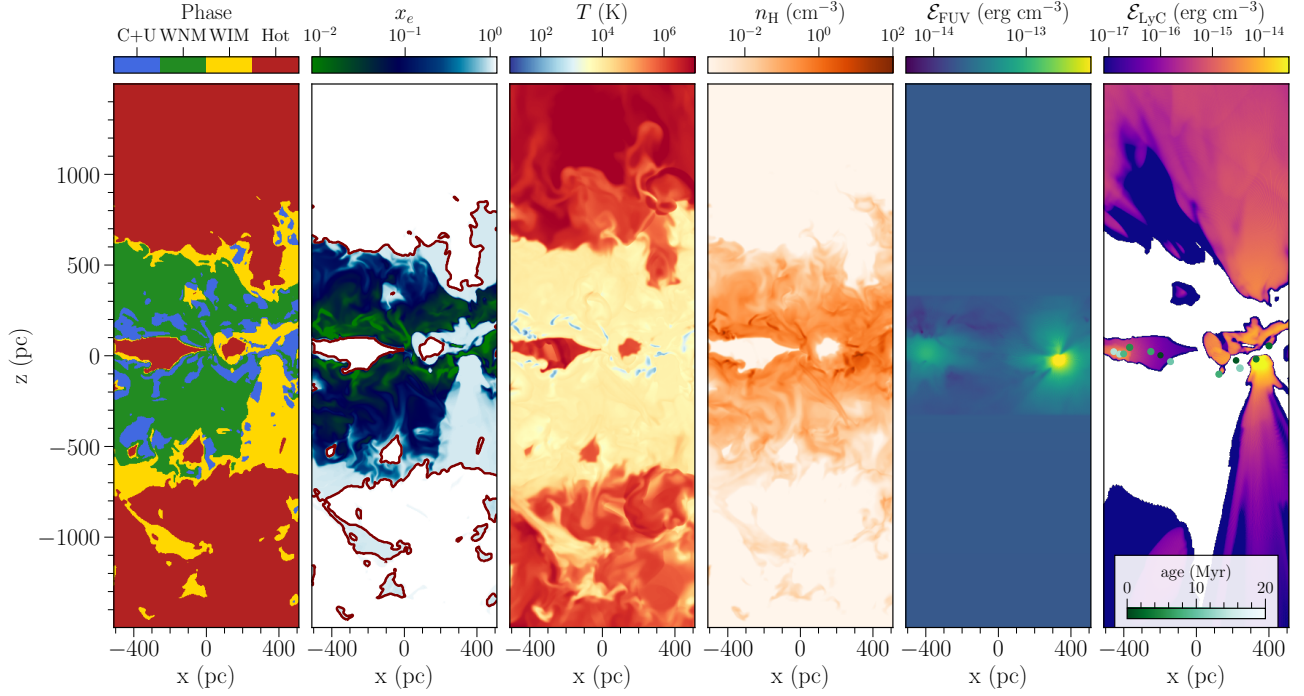


Figure 1. Vertical slices of the R8-4pc simulation at $t = 430$ Myr through $y = 200$ pc. From left to right, the panels show ISM phase (see Table 2 for phase definitions), electron abundance (x_e), temperature (T), number density of hydrogen (n_H), FUV energy density (\mathcal{E}_{FUV}), and LyC energy density (\mathcal{E}_{LyC}). The points in the rightmost panel represent radiation source particles projected onto the $y = 200$ pc plane. The age of each source is given by its color, and the points are limited to sources with ages less than 20 Myr. In the panel showing x_e , the red contour marks the boundary between the hot and WIM phases.

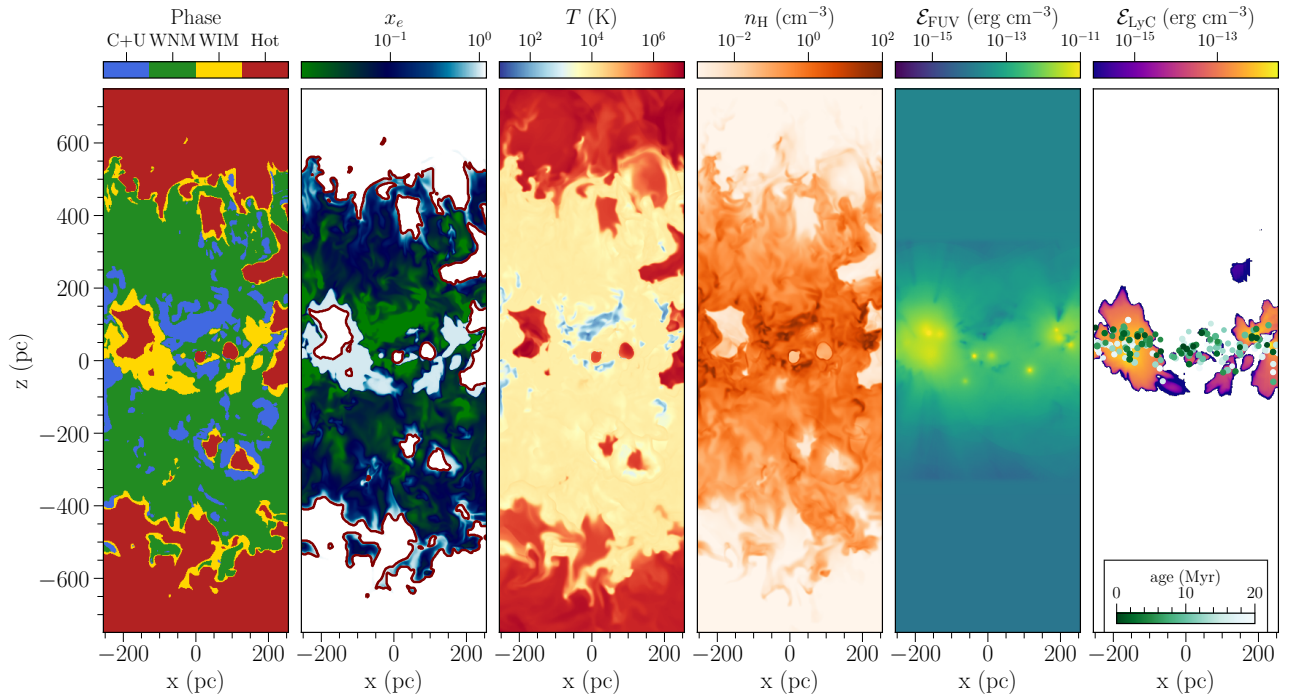


Figure 2. Same as Figure 1 but for the LGR4-2pc model at $t = 298$ Myr through $y = 0$.

Table 2. Phase Definition

Name	Temperature	Abundance	Shorthand
Cold and Unstable Medium	$T < 6 \cdot 10^3 \text{ K}$...	C+U
Warm Neutral Medium	$6 \cdot 10^3 \text{ K} < T < 3.5 \cdot 10^4 \text{ K}$	$x_{\text{H}^0} > 0.5$	WNM
Warm Ionized Medium	$6 \cdot 10^3 \text{ K} < T < 3.5 \cdot 10^4 \text{ K}$	$x_{\text{H}^+} > 0.5$	WIM
Warm-Hot and Hot Ionized Medium	$3.5 \cdot 10^4 \text{ K} < T$...	hot

to our previous post-processing simulations (Kado-Fong et al. 2020), where the ionization state in each location was evolved until equilibrium was attained. With fully time-dependent simulations, more of the gas remains partially ionized (J.-G. Kim et al., in prep.).

Radiation Fields—In the final two panels of Figure 1 and Figure 2 (see also Figure 3 and Figure 4), we show the energy density of FUV and LyC radiation. Individual young cluster particles colored by age are overlaid on the LyC panel. These clusters act as the sources of UV photons. In regions with sources surrounded by hot gas, radiation is essentially unattenuated until it begins to interact with denser gas and dust at larger distance. FUV and LyC photons are absorbed by dust in both neutral and ionized gas; neutral (or partially ionized) gas absorbs LyC only. In addition to a sharp transition between WIM and neutral phases, the photoionization front is also visible as a sharp drop in the \mathcal{E}_{LyC} panel. LyC is strongly attenuated in neutral gas because of the high photoionization crosssection. Therefore, a significant volume is not instantaneously exposed to any ionizing radiation. Nonetheless, as noted above, the recombination timescale in low-density gas can be long enough for intermittently-irradiated gas to remain partially ionized. Thus, there are locations where WIM gas is present without LyC radiation.

Since the dust absorption crosssection is three orders of magnitude lower than the photoionization crosssection, FUV radiation is not attenuated as strongly as the LyC radiation, and therefore fills the whole simulation volume. For TIGRESS-NCR simulations, however, the FUV radiation is followed by ray tracing only within 300 pc of the midplane. Above this height, the plane parallel approximation is used to reduce the computational cost of the simulations (see Section 2.1.2). This can be seen in the vertical slices as a transition from a radiation field that is fully resolved spatially to a horizontally averaged value.

Midplane Structure—In the horizontal slices shown in Figure 3 and Figure 4, there are classical H II regions at approximately $x = -200$ pc, $y = -130$ pc for the R8-4pc simulation, and $x = 85$ pc, $y = 200$ pc for the LGR4-2pc simulation. Both regions are outlined with black contours as defined by the separation between the WIM and C+U phases. Each H II region is marked by a young source in the center which produces the high ionizing radiation density seen in \mathcal{E}_{LyC} . These H II regions are distinct from diffuse ionized gas because they appear as bubbles of WIM embedded in colder gas, unlike the majority of the WIM in our simulations which is generally bounded by WNM and by hot gas. H II regions have sim-

ilar density to the surrounding gas (this is also true for diffuse WIM), as can be seen in the bottom left panel, but they have much higher x_e and radiation density.

The projection of cluster positions shows that radiation sources are primarily found within the hot and warm gas that fills most of the volume. As noted above, LyC is able to propagate unimpeded through the hot gas. In denser warm gas, provided the LyC radiation intensity is sufficient to maintain a highly ionized state, photon packets continue to propagate along rays while being attenuated subject to the rate at which photons are used up by balancing recombinations. If in a given cell the LyC intensity is too low to maintain a fully ionized state, rays will be strongly attenuated. In the midplane slices, we see sharp gradients in x_e separating the WIM and WNM. These sharp gradients in x_e arise due to strong local attenuation of the LyC. The hot regions that contain LyC sources will always be surrounded by a diffuse WIM layer separating the hot gas from the WNM.

The FUV radiation can propagate throughout most of the midplane region. Nevertheless, there are darker regions evident in the FUV energy density slice. Some of these coincide with regions of very high gas density. A few of these low- \mathcal{E}_{FUV} regions correspond to shadows which are created when a dense clump intercepts radiation from a source.

In addition to the midplane slices, we also present one-dimensional cuts of the R8-4pc simulation variables in Figure 5. We plot the simulation variables in the snapshot shown in Figure 3 at $z = 0$ pc, $y = -134$ pc (horizontal dashed line in the bottom-left panel). This cut was chosen such that it passes through the H II region described previously. We include the values of x_e , T , n_{H} , \mathcal{E}_{FUV} , and \mathcal{E}_{LyC} . Along with \mathcal{E}_{FUV} , we also show the value of χ_{FUV} , the FUV radiation density divided by the reference value defined in Draine (1978a), 8.94×10^{-14} erg cm $^{-3}$. Background shading in each panel indicates the defined gas phases.

The values of \mathcal{E}_{LyC} and x_e are highly correlated, as would be expected. The attenuation of LyC in regions of high density can be seen by the absence of \mathcal{E}_{LyC} corresponding to most regions with high n_{H} . One exception to this behavior is at $x \sim -200$ pc where the slice passes through the classical H II region. Both the LyC and FUV radiation are much higher in this region due to the presence of a source particle. The ionization fraction is similarly increased. The density, however, is similar to the surrounding gas ($\sim 10^2$ cm $^{-3}$) and the temperature is $\sim 10^4$ K, as would be expected in a typical H II region.

3.2. Vertical Profiles

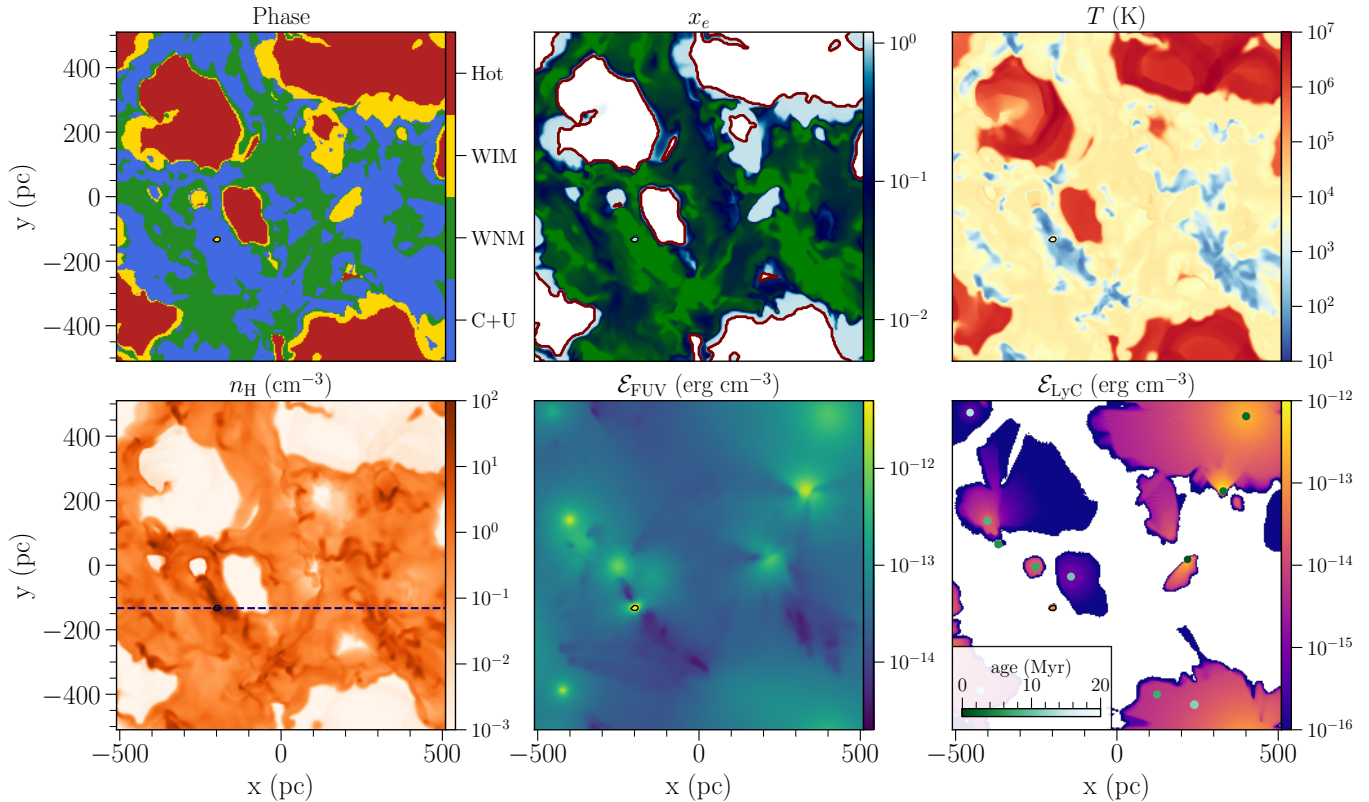


Figure 3. Horizontal slices of the R8-4pc model at $z = 0$ pc and $t = 430$ Myr, with the same quantities shown in Figure 1. Clockwise from top left the panels represent ISM phase, x_e , T , \mathcal{E}_{LYC} , \mathcal{E}_{FUV} , and n_{H} . Source particles are shown in the bottom right panel. The red contour in the x_e panel represents the boundary between hot and WIM. Additionally, the black contour in each panel represents a classical H II region, which contains a star cluster source of mass $1.3 \times 10^3 M_{\odot}$ (this cluster particle is omitted from the \mathcal{E}_{LYC} panel for clarity). The dashed horizontal line shown in the bottom left panel represents the 1D, horizontal ray used in Figure 5.

In this section, we consider the distribution of simulation variables over time as a function of the vertical (z) coordinate. For each snapshot at every height z we take the horizontal (x - y) average of various quantities as in Kim et al. (2023a) defined by

$$\langle q \rangle_{\text{ph}} = \frac{\iint q \Theta(\text{ph}) dx dy}{L_x L_y} \quad (3)$$

where $\Theta(\text{ph}) = 1$ if the gas is in the given phase (as defined by Table 2) and 0 otherwise. The volume filling factor (f_V) is defined similarly as $f_{V,\text{ph}} = \iint \Theta(\text{ph}) dx dy / L_x L_y$. We define the characteristic values of n_{H} , \mathcal{E}_{LYC} , and \mathcal{E}_{FUV} as the average within a phase, $\bar{q}_{\text{ph}} = \langle q \rangle_{\text{ph}} / f_{V,\text{ph}}$. We also include the mass weighted value of $x_e = \langle n_e \rangle / \langle n_{\text{H}} \rangle$. These vertical profiles are shown for the R8-4pc and LGR4-2pc simulations in Figure 6 and Figure 7, respectively. In each panel, the central, dark line represents the median value while the shaded area shows the 25–75th percentile region across all snapshot times. For each phase, results for a given z coordinate are only included if at least 25% of the snapshot times have gas of that phase at that altitude.

Therefore, there are regions at high z where, for example, no C+U gas is shown.

The top left panel represents $\langle n_{\text{H}} \rangle$ for each gas phase. In all phases, the highest density is found close to the midplane, then generally decreasing with increasing z . The C+U gas shows a significant drop in $\langle n_{\text{H}} \rangle$ moving away from the midplane because the averaging is done over the full horizontal area, and this gas has a low volume filling fraction f_V at large altitudes (see top right panel).

Above ~ 1 kpc, the hot gas completely dominates the volume, with the other three phases having $f_V < 10\%$. At even higher z , the filling fraction of the colder phases is further reduced, with each occupying less than $\sim 1\%$ of the volume. Near the midplane, all four phases have more similar values of f_V , between approximately 10–50% for each of the phases defined in Table 2. This can also be seen in the horizontal snapshot (Figure 3). At $z = 0$, the hot gas filling fraction increases while the warm gas occupies less volume because hot gas is generated there via shock heating (Kado-Fong et al. 2020).

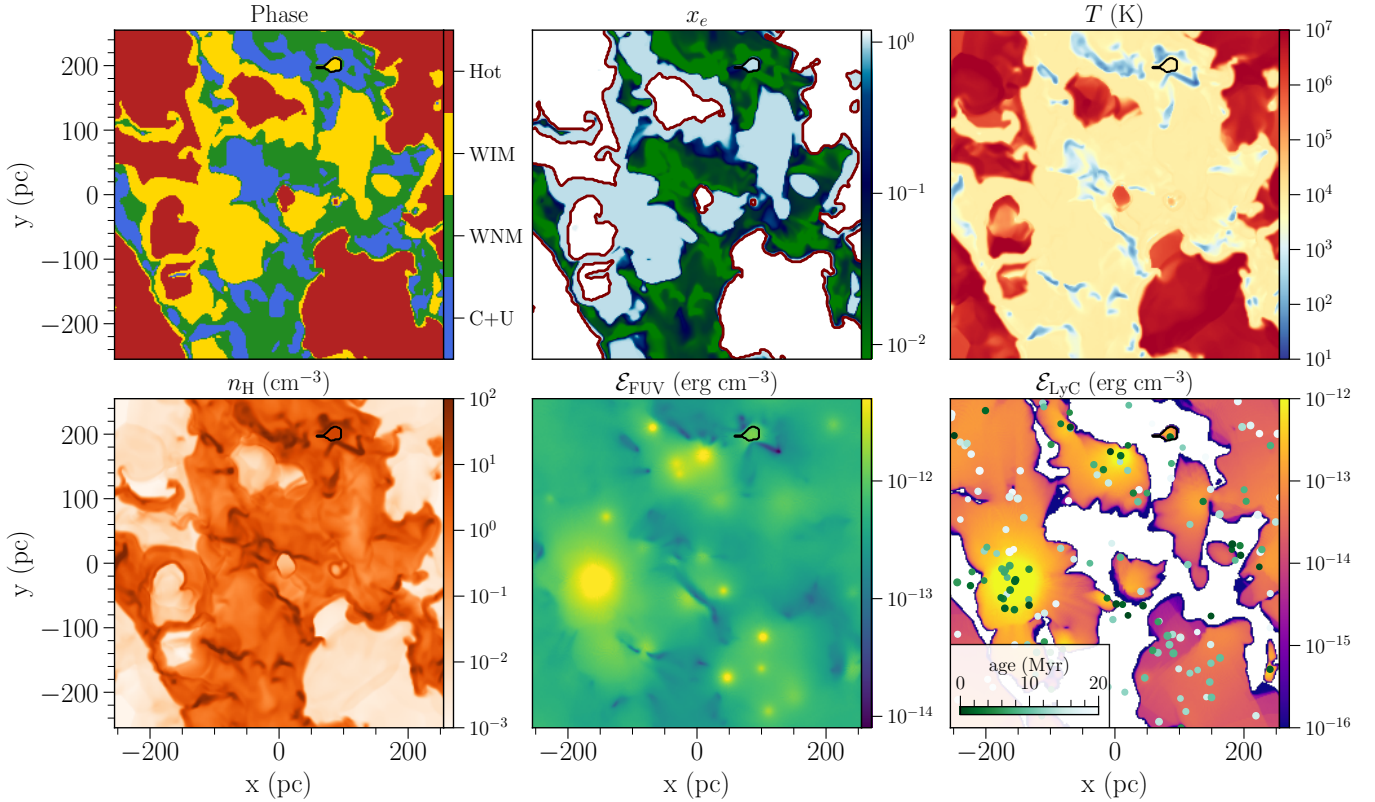


Figure 4. Same as Figure 3 but for the LGR4-2pc model at $t = 298$ Myr. The black contour in each panel represents a classical H II region, which contains a star cluster source of mass $1.2 \times 10^3 M_{\odot}$.

For values of the mass fraction and the volume filling factors of each phase within $|z| < 300$ pc, see Table 4 in Kim et al. (2023a).

The remaining four panels of Figure 6 and Figure 7 show characteristic values of simulation variables within each phase. Like the volume-averaged density, the characteristic density (\bar{n}_{H}) within each phase peaks at the midplane. The value of \bar{n}_{H} in the hot gas drops exponentially over all z . The characteristic densities within the cold and warm gas decline at larger z , until reaching the extraplanar fountain region at $|z| \gtrsim 500$ pc where densities plateau at $\bar{n} \sim 0.01 - 0.1 \text{ cm}^{-3}$. In Appendix B, we explain why the majority of the ionized gas mass in galaxies is expected to be in the diffuse component outside of classical H II regions.

The middle-right panel represents the mass weighted electron abundance $x_e = \langle n_e \rangle / \langle n_{\text{H}} \rangle$ within each phase. The hot gas is completely ionized with $x_e \approx 1.2$ (also seen in Figure 3). The WIM is almost fully ionized with $x_e \approx 1$ at all z values, despite being defined only as gas with $x_{\text{H}^+} > 0.5$. The C+U gas, as well as the WNM, is partially ionized at all heights, but the ionization fraction is low (< 0.1) at the midplane.

The LyC and FUV radiation energy density profiles are presented in the bottom row. These show similar be-

havior, both strongly peaked at the midplane, but the dynamic range in LyC is much larger than FUV. For the LyC radiation, we include only the hot gas and WIM as the other (neutral) phases have much lower radiation density in this wavelength regime due to the high attenuation in regions with higher density. All four phases are shown for the FUV radiation, and each has centrally peaked profiles with lower radiation energy density in the neutral phases compared to the ionized. The FUV profiles flatten at $|z| \gtrsim 300$ pc as gas density is sufficiently low and FUV photons become optically thin. For the FUV profiles, we include a scale normalized to the Draine value ($\chi_{\text{FUV}} = \mathcal{E}_{\text{FUV}} / 8.94 \times 10^{-14} \text{ erg cm}^{-3}$) on the right axis.

We fit the median radiation energy density in both the LyC and FUV bands with an exponential distribution given by

$$\mathcal{E}(z) = \mathcal{E}_0 e^{-|z|/b}. \quad (4)$$

For the FUV radiation, we fit the energy density profile in the WNM since this vertical dependence is most relevant for heating through the photoelectric effect; the profile in the C+U is quite similar. For the LyC radiation, we look at the energy density profile in the WIM as this phase is most relevant for photoionization. In both cases, the fit is limited to $|z| < 300$ pc as above

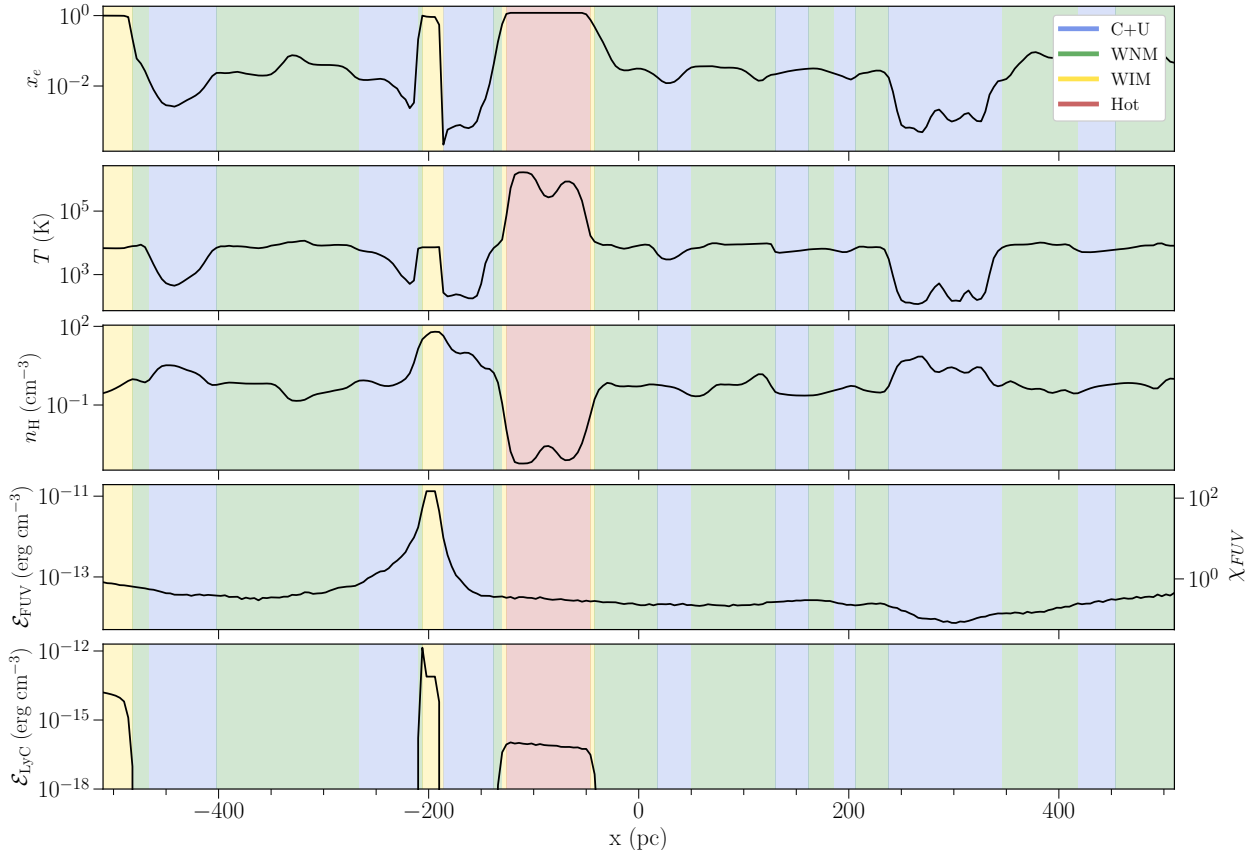


Figure 5. Physical quantities along a 1D, horizontal ray through $z = 0$, $y = -134$ pc of the R8-4pc model at $t = 430$ Myr. From top to bottom, the panels represent x_e , T , n_H , \mathcal{E}_{FUV} , and \mathcal{E}_{LyC} . The gas phase is represented by the background color. Sharp photoionization fronts are clearly seen in the \mathcal{E}_{LyC} and x_e and T panels, which separate WIM from CNM gas. These represent the boundary of the H II region visible in Figure 3 at $x = -200$ pc.

this height we are not performing the full ray-tracing for the FUV radiation and the disk enters an optically thin regime.

The fit to the LyC radiation in the R8-4pc simulation gives an exponential scale height of $b = 60$ pc with normalization $\mathcal{E}_0 = 6.8 \times 10^{-14}$ erg cm $^{-3}$. The FUV radiation has $b = 350$ pc with normalization $\mathcal{E}_0 = 6.6 \times 10^{-14}$ erg cm $^{-3}$, corresponding to $\chi_{\text{FUV}} = 0.74$. That is, the midplane FUV radiation energy density is very close to the Draine value (see Figure 13 for additional comparisons). We note that the peak value of χ_{FUV} is ~ 5 times higher in the WIM than in the WNM, while decreasing to match the value in the WNM at larger z . This is not surprising, since the WIM near the midplane includes H II regions immediately surrounding radiation sources, where the FUV is preferentially enhanced.

The FUV radiation in the LGR4-2pc simulation is best fit by an exponential scale height $b = 90$ pc with normalization $\mathcal{E}_0 = 5.2 \times 10^{-13}$ erg cm $^{-3}$, corresponding to $\chi_{\text{FUV}} = 5.8$. We find the LyC component of the LGR4-2pc simulation to drop rapidly away from $z = 0$ pc. Therefore, we fit only $|z| < 200$ pc and find

the best fit to have an exponential scale height $b = 30$ pc with normalization $\mathcal{E}_0 = 5.7 \times 10^{-13}$ erg cm $^{-3}$.

3.3. History

We present the time evolution and statistics of different physical parameters from the R8-4pc and LGR4-2pc simulations in Figure 8 and Figure 9, respectively. For each quantity, we show temporal histories in the left panel. On the right, we show the same variables but as a histogram representing the distribution of each value over time. Since all quantities represent horizontal averages, and at any given time our box does not fully sample from the conditions appearing over the ISM/star formation lifecycle, the level of temporal variation is subject to the horizontal size of the simulation domain; a larger (smaller) horizontal domain would naturally have less (more) variation. Table 3 summarizes the median values and 16th–84th percentiles of these quantities over time.

The first row represents the surface densities of ionizing photon rate $\Phi_{\text{LyC}} = Q_{\text{i,tot}}/(L_x L_y)$, the star formation rate (SFR) $\Sigma_{\text{SFR},10\text{Myr}}$, and the FUV luminosity

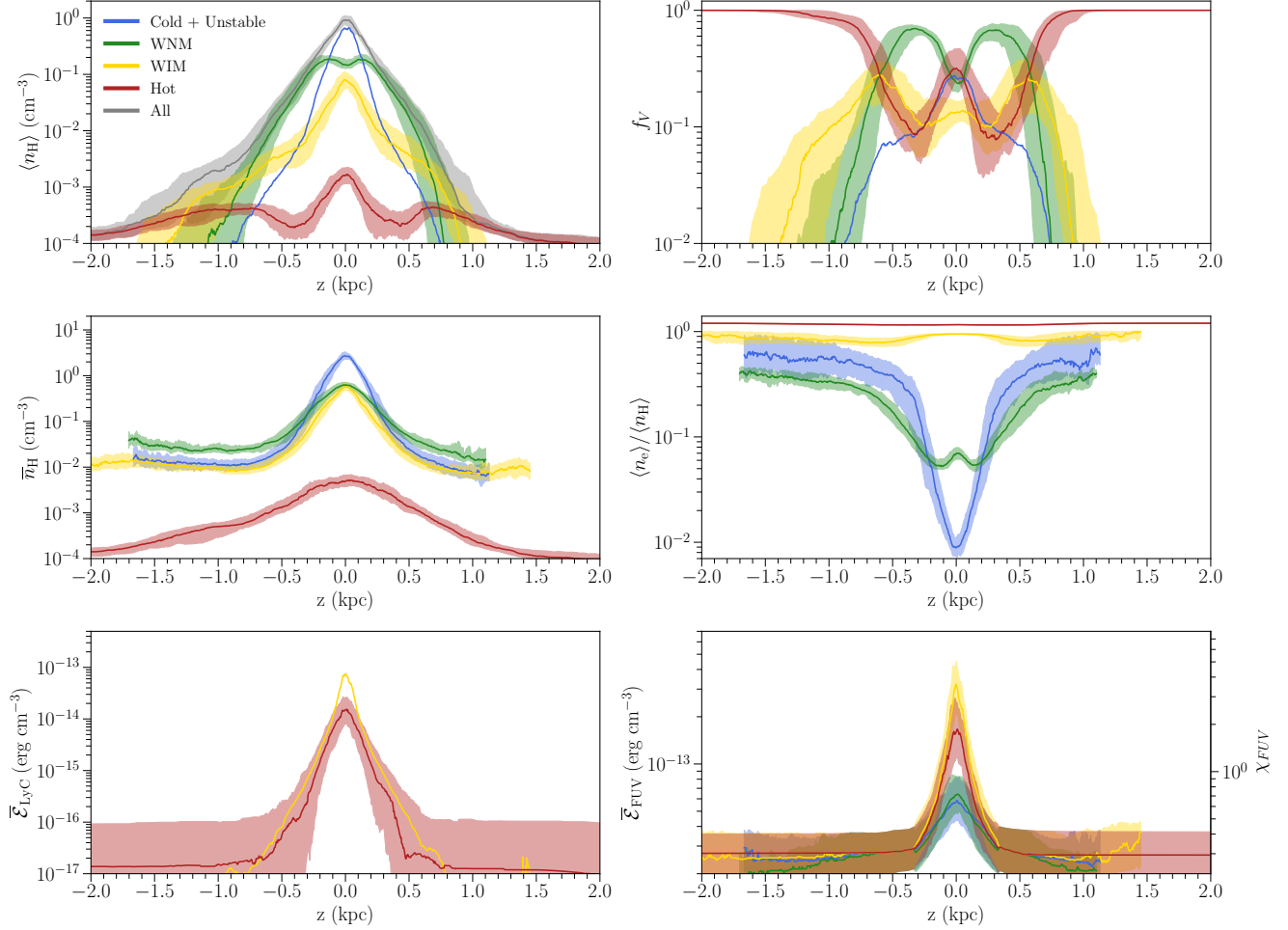


Figure 6. Vertical profiles of contribution to the mean density $\langle n_H \rangle$ and volume filling factor f_V for each of four ISM phases, as well as density \bar{n}_H , mass weighted electron abundance $x_e = \langle n_e \rangle / \langle n_H \rangle$, and LyC and FUV radiation density $\bar{\mathcal{E}}_{\text{LyC}}$ and $\bar{\mathcal{E}}_{\text{FUV}}$ within defined gas phases. Profiles are based on ~ 200 simulation snapshots between 250–450 Myr for the R8-4pc model. The lines represent the median value and the shaded regions indicate 25th–75th percentiles. See text for details.

$\Sigma_{\text{FUV}} = L_{\text{FUV,tot}} / (L_x L_y)$. Here, $Q_{i,\text{tot}}$ and $L_{\text{FUV,tot}}$ are the total ionizing photon rate and FUV luminosity summed over source particles, respectively. The SFR is calculated using only star particles with ages less than 10 Myr. These three values appear to be well correlated in time as would be expected because young stars are the major source of the FUV and LyC radiation. The LyC radiation has greater variation in amplitude because it is coming from even younger stars ($t < 5$ Myr).

The median value of the SFR in R8-4pc is $\Sigma_{\text{SFR},10\text{Myr}} = 0.0028 M_\odot \text{pc}^{-2} \text{Myr}^{-1}$ (Figure 8, top right panel), which is very similar to observed estimates for the solar neighborhood in the Milky Way (e.g. Fuchs et al. 2009; Mor et al. 2019; Zari et al. 2023). The median value of the FUV luminosity per unit area is $\Sigma_{\text{FUV}} = 1.0 \times 10^7 L_\odot \text{kpc}^{-2}$; this is consistent with expectations given the above median $\Sigma_{\text{SFR},10\text{Myr}}$ and the expected FUV luminosity to SFR ratio, which for con-

stant SFR is $L_{\text{FUV}} / \text{SFR} = 4.3 \times 10^3 L_\odot / (M_\odot \text{Myr}^{-1})$ based on our adopted initial mass function and spectral population synthesis choices (see Appendix C in Kim et al. 2023b). The median ionizing photon rate (and the 16th and 84th percentiles) is $\Phi_{\text{LyC}} = 4.3^{+2.6}_{-2.2} \times 10^{50} \text{s}^{-1} \text{kpc}^{-2}$ with a mean (and standard deviation) of $\Phi_{\text{LyC}} = 4.8 \pm 3.0 \times 10^{50} \text{s}^{-1} \text{kpc}^{-2}$. These values are similar to the post-processing results presented in Kado-Fong et al. (2020) and are consistent with the observational estimate for the solar neighborhood of $\Phi_{\text{LyC}} = 5.0 \times 10^{50} \text{s}^{-1} \text{kpc}^{-2}$ (McKee & Williams 1997).

The second row presents the gas mass fraction for the cold gas, total warm gas, and for the WIM alone. For R8-4pc, the majority of the gas mass is contained in the warm phase, with an average of $50 \pm 9\%$. A fraction of this warm gas is WIM, which makes up $9 \pm 5\%$ of the total mass. Most of the remaining gas mass is in the cold and unstable medium, making up an average $49 \pm 9\%$. A

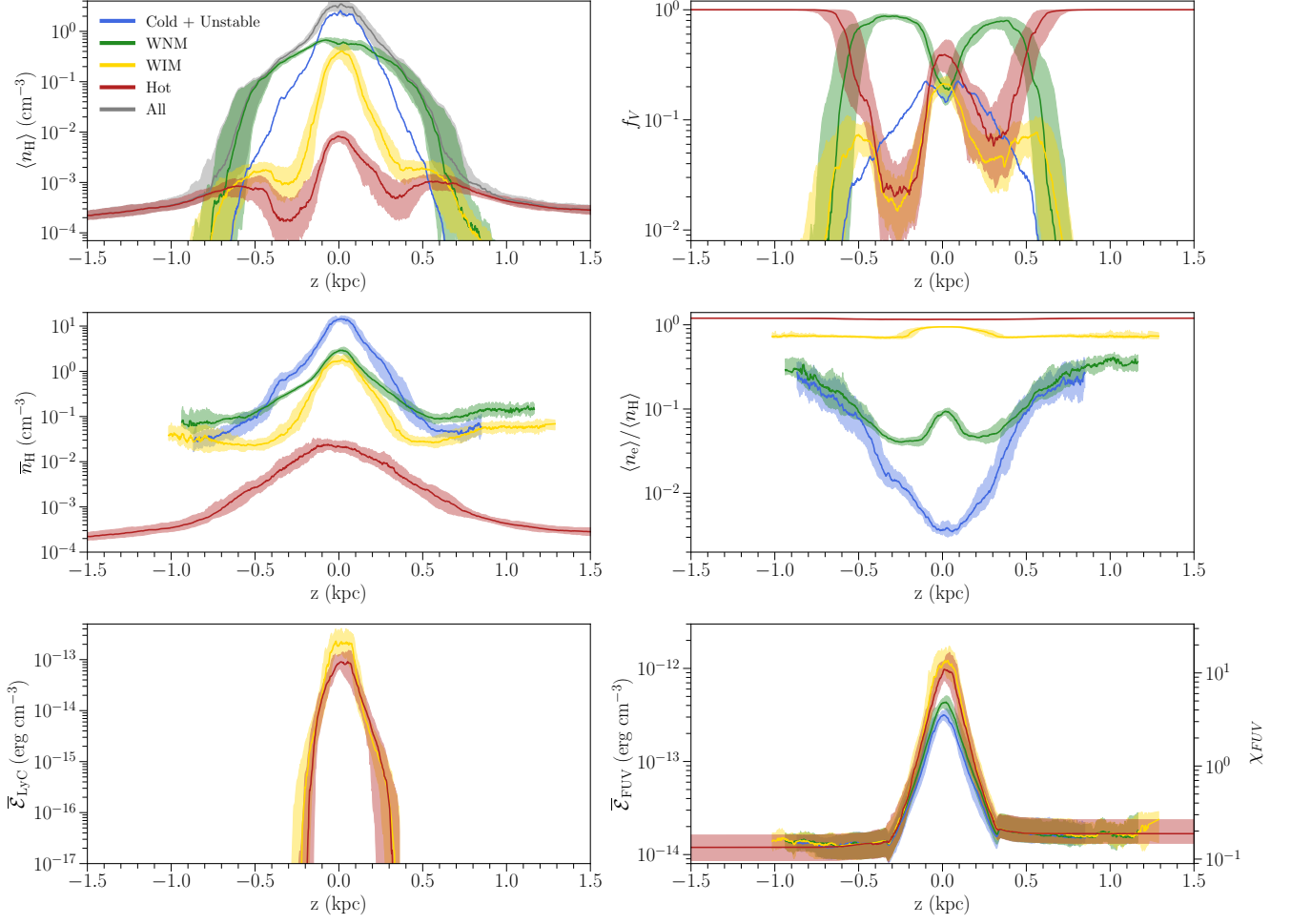


Figure 7. Same as Figure 6 but for the LGR4-2pc model between times 250–350 Myr.

small fraction of the total gas mass is in the hot medium. In the inner-disk LGR4-2pc model, the fraction of cold gas increases compared to R8-4pc. For a more detailed breakdown of the mass distribution by phase refer to Table 4 of Kim et al. (2023a).

The scale heights of the C+U, total warm, and WIM phases are shown in the third row. We also show the scale height of n_e^2 (observable as emission measure EM per unit length along the line of sight), which is proportional to the emissivity of the WIM. The scale height is defined as

$$H = \sqrt{\frac{\int \langle q \rangle_{\text{ph}} z^2 dz}{\int \langle q \rangle_{\text{ph}} dz}} \quad (5)$$

Here $\langle q \rangle_{\text{ph}}$ (Equation 3) defines the horizontal average over a given phase at a given z value. To find the scale height of each phase, we set $q = n_{\text{H}}$. We also find the scale height of n_e^2 by setting $q = n_e^2$. For R8-4pc, the median scale height of the C+U gas is 110 pc. The combined warm gas has a median scale height of 260 pc while WIM alone has a slightly larger median scale height of

280 pc. The warm gas scale height is somewhat smaller (by $\sim 15\%$) in LGR4-2pc owing to the higher surface density and therefore higher gravity. The higher gravity is partly offset by slightly larger velocity dispersion (see Table 2 in Kim et al. 2023a). The median value of the EM scale height is much smaller, approximately 90 pc. As in Kado-Fong et al. (2020), the scale height we measure for the WIM can be much smaller than observational estimates because our definition of the phase does not distinguish between diffuse and dense (H II regions) ionized gas and the emission is dominated by the latter. All of the scale heights vary in time by a factor $\sim 2-3$ from minimum to maximum.

In the final row, we show different source particle scales. The first is the average distance between sources, $\ell_{\star} \equiv N_{\star}^{-1/2}$ where N_{\star} is the surface number density of FUV sources younger than 20 Myr that account for 90% of the total FUV luminosity cumulating downward from the most luminous sources. The median values are $\ell_{\star} = 280$ pc and 65 pc for R8-4pc and LGR4-2pc, respectively. If we consider only ionizing sources, defined

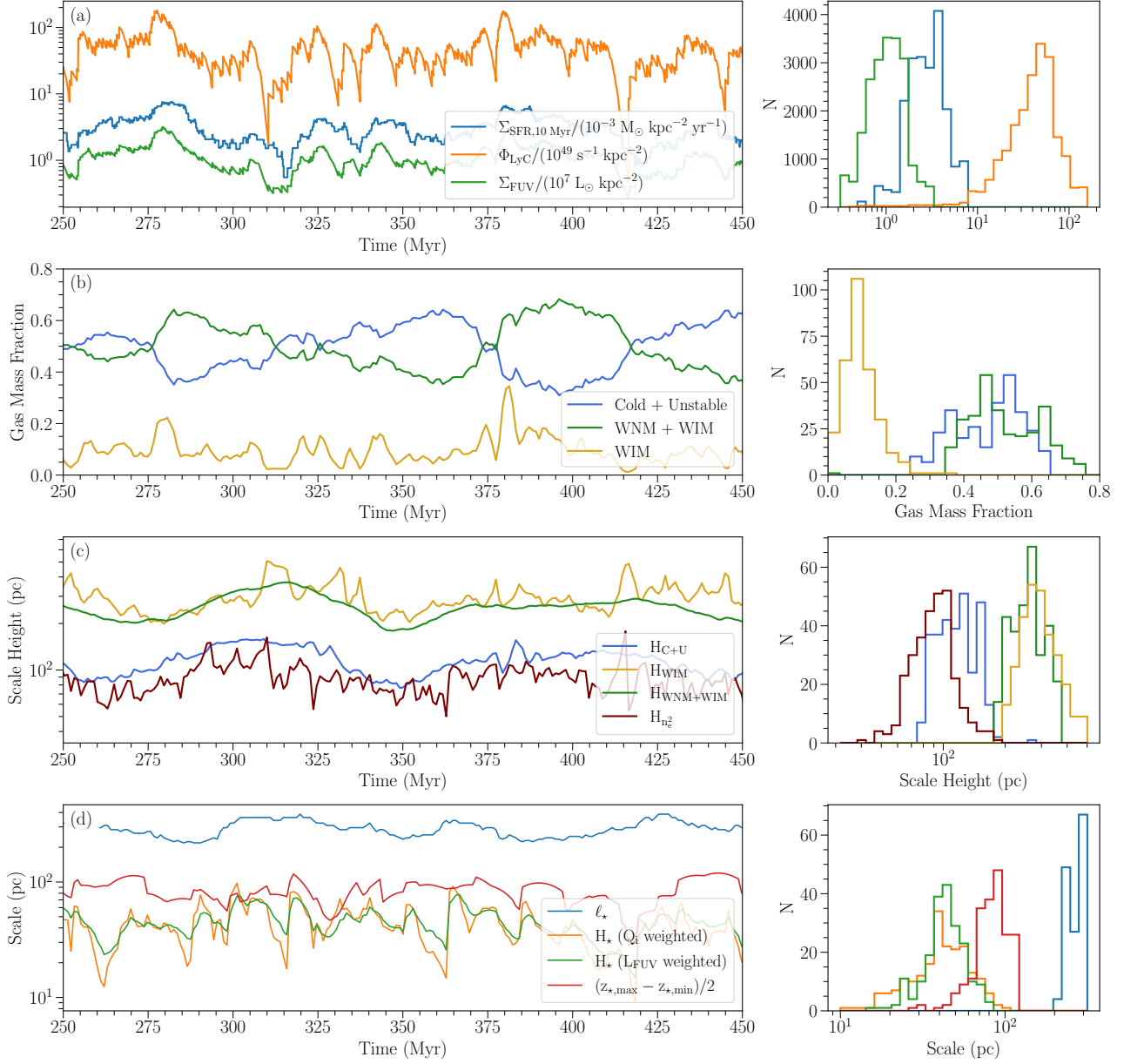


Figure 8. Temporal evolution and statistics of key global simulation quantities, for the R8-4pc model. From top to bottom, the left column shows (a) the LyC (ionizing) photon rate, star formation rate, and FUV energy input rate per unit area averaged over the whole simulation domain, (b) total mass fractions of gas in different thermal phases, (c) scale heights of different phases of gas, as well as n_e^2 (\propto emission measure) (d) mean in-plane separations ℓ_* of cluster particle sources (with $t_{\text{age}} < 20$ Myr) as well as their scale heights and maximum and minimum z locations. The right panels show statistical distributions of these same quantities as histograms including all times.

as the sources which account for more than 90% of the total LyC luminosity, the separation is much larger, averaging approximately 460 pc for R8-4pc and 110 pc for LGR4-2pc. The characteristic source luminosity is then $\Sigma_{\text{FUV}}/N_* \sim 10^6 L_\odot$ and $\Phi_{\text{LyC}}/N_* \sim 10^{50} \text{ s}^{-1}$ for FUV and LyC sources, respectively. The quantity ℓ_* will be used in Section 4.2.3 in testing an estimator of the FUV radiation field.

The figure also includes the scale height of sources (H_*). Similar to gas scale heights, H_* is calculated as the luminosity-weighted rms distance from the mid-plane, using Equation 5. The result for both weightings (FUV and LyC) is comparable, with median value $H_* = 40_{-10}^{+10}$ pc and 50_{-10}^{+10} pc for R8-4pc and LGR4-2pc, respectively. The last measure of the source distribution is the approximate vertical extent of the particles, defined as $(z_{\text{max}} - z_{\text{min}})/2$. Here, z_{max} and z_{min} represent

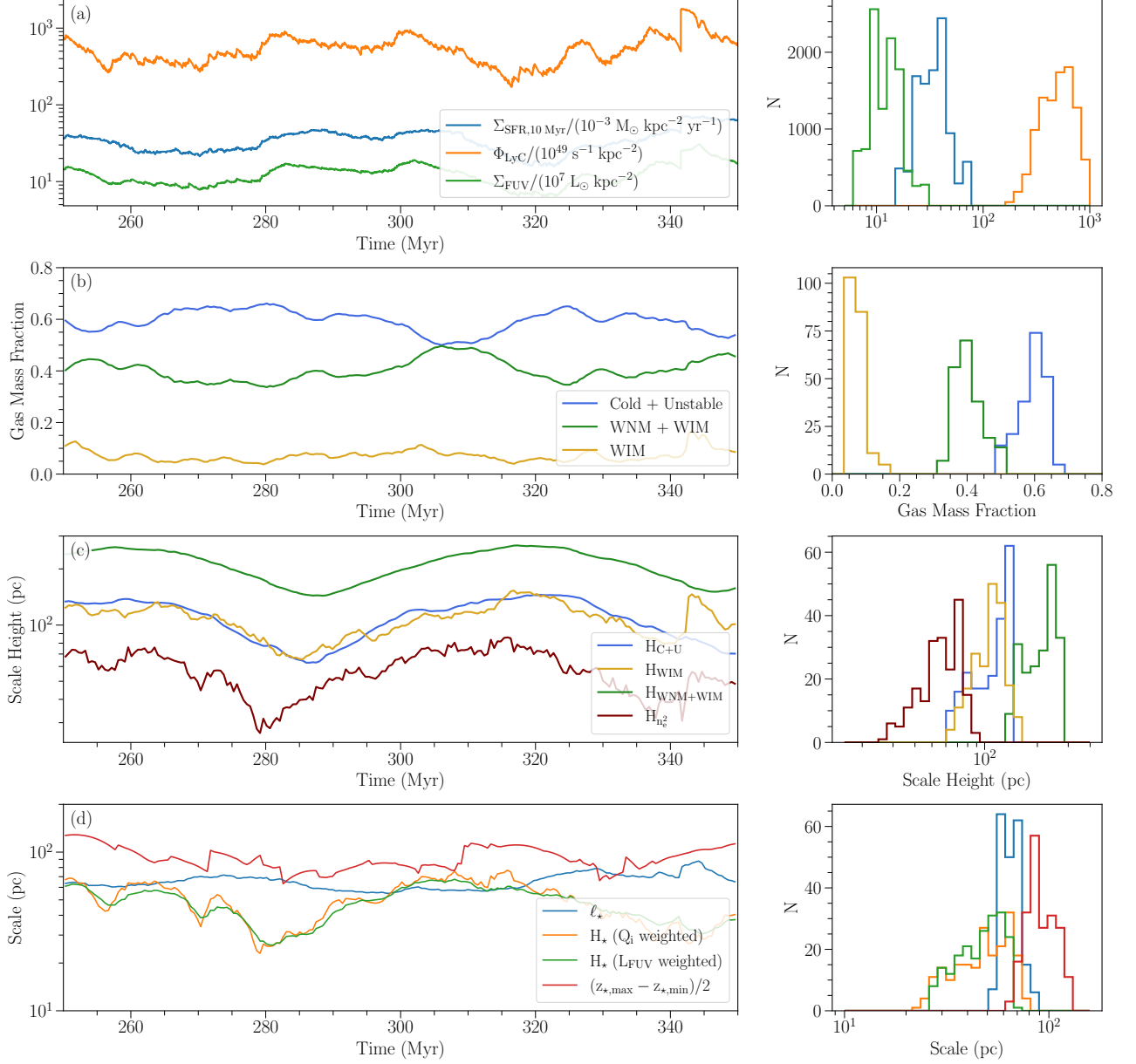


Figure 9. Same as Figure 8, but for the LGR4-2pc model.

the maximum and minimum z values among the sources at each time.

The vertical scale height of the cluster particles (radiation sources) is comparable in the R8-4pc and LGR4-2pc simulations, while the higher SFR in the latter also corresponds to a smaller horizontal separation between sources, ℓ_* . With $\Sigma_{\text{SFR}} \propto N_* = \ell_*^{-2}$, we would expect a ratio of $\ell_*[\text{LGR4-2pc}]/\ell_*[\text{R8-4pc}] \sim 0.29$, which is close to the actual ratio of 0.23.

4. FUV RADIATION FIELD

We now focus on the radiation fields in the TIGRESS-NCR simulations, beginning with FUV radiation. First,

we present the general characteristics of the FUV radiation field. Then, we evaluate a number of simplified models for the FUV radiation which may be used when full ray tracing might not be feasible.

4.1. Radiation Field Distribution

To lowest order, we expect the radiation intensity to vary proportional to the total (time-varying) FUV luminosity per unit area, $\Sigma_{\text{FUV}} = L_{\text{FUV,tot}}/(L_x L_y)$, where $L_{\text{FUV,tot}}$ is the total FUV luminosity from the source

Table 3. Physical Quantities Measured in Simulations

Value	R8-4pc	LGR4-2pc	Description
Σ_{gas}	$10.6^{+0.2}_{-0.2}$	$37.9^{+1.3}_{-0.9}$	Gas surface density in $M_{\odot} \text{pc}^{-2}$
Σ_{SFR}	$2.8^{+1.5}_{-1.0}$	$34.8^{+10.4}_{-10.7}$	10 Myr averaged SFR surface density in $10^{-3} M_{\odot} \text{kpc}^{-2} \text{yr}^{-1}$
Σ_{FUV}	$1.0^{+0.5}_{-0.4}$	$12.3^{+4.5}_{-3.4}$	FUV luminosity per unit area in $10^7 L_{\odot} \text{kpc}^{-2}$
Φ_{LyC}	$4.3^{+2.6}_{-2.2}$	53^{+23}_{-20}	Ionizing photon rate per unit area in $10^{50} \text{photons s}^{-1} \text{kpc}^{-2}$
H_w	260^{+40}_{-50}	220^{+40}_{-60}	Scale height in pc for total warm (WNM+WIM) gas
H_{c+u}	110^{+30}_{-30}	120^{+20}_{-40}	Scale height in pc for C+U phase
l_*	280^{+60}_{-40}	65^{+8}_{-7}	Mean horizontal distance between FUV sources ($t_{\text{age}} < 20 \text{ Myr}$) in pc
H_*	40^{+10}_{-10}	50^{+10}_{-10}	Scale height of FUV sources in pc weighted by FUV luminosity
z_*	80^{+20}_{-20}	90^{+20}_{-11}	Approximate vertical extent of the particles, defined as $(z_{\text{max}} - z_{\text{min}})/2$
$J_{\text{FUV, mid}}$			Midplane FUV intensity in $10^{-4} \text{erg cm}^{-2} \text{sr}^{-1} \text{s}^{-1}$ limited to gas with $T < 3.5 \times 10^4 \text{ K}$
mass weighted	$1.1^{+3.0}_{-0.7}$	$6.5^{+12.0}_{-4.5}$	
volume weighted	$1.2^{+2.2}_{-0.7}$	$9.3^{+11.3}_{-5.2}$	
\mathcal{J}_{mid}			Midplane normalized FUV intensity \mathcal{J} (Equation 6) for gas with $T < 3.5 \times 10^4 \text{ K}$
mass weighted	$0.3^{+0.8}_{-0.2}$	$0.2^{+0.3}_{-0.1}$	
volume weighted	$0.4^{+0.6}_{-0.2}$	$0.2^{+0.3}_{-0.1}$	
$\mathcal{J}_{ z < 300 \text{ pc}}$	$0.5^{+0.1}_{-0.1}$	$0.15^{+0.04}_{-0.03}$	Volume-weighted average of \mathcal{J} within 300 pc of the midplane including all gas

NOTE— The reported values are median and 16th and 84th percentiles over $t = 250\text{--}450 \text{ Myr}$ for R8-4pc and $t = 250\text{--}350 \text{ Myr}$ for LGR4-2pc.

particles and $L_x L_y$ is the horizontal area.⁴ We therefore define a normalized mean intensity in the FUV band by

$$\mathcal{J} \equiv \frac{J_{\text{FUV}}}{\Sigma_{\text{FUV}}/(4\pi)}. \quad (6)$$

where $J_{\text{FUV}} = (c/4\pi)\mathcal{E}_{\text{FUV}}$ is the mean intensity in the FUV band. In Figure 10, we show the mass-weighted distribution of \mathcal{J} at the midplane for model R8-4pc. The figure presents the two-dimensional distribution in \mathcal{J} and n_{H} , as well as the individual, mass-weighted PDF of each. We include all gas in the midplane ($|z| < 4 \text{ pc}$) with $T < 3.5 \times 10^4 \text{ K}$ across all snapshot times. Figure 11 shows the same for model LGR4-2pc at the midplane ($|z| < 2 \text{ pc}$). For both models, there is a unimodal

distribution of \mathcal{J} with a well-defined central peak, but tails extending over more than two orders of magnitude. The modes of each radiation distribution, $\mathcal{J} \approx 0.3$ for R8-4pc and $\mathcal{J} \approx 0.2$ for LGR4-2pc, are quite similar to the mass-weighted means at the midplane reported in Table 3. The peak of the \mathcal{J} distribution shifts to lower values at higher n_{H} , with this shift more pronounced in LGR4-2pc as would be expected given the higher densities and optical depth of this model.

We fit this peak in \mathcal{J} as a function of n_{H} with a local shielding approximation similar to that suggested by Kim et al. (2021)

$$\mathcal{J} = \mathcal{J}_0 e^{-\tau_{\text{FUV, eff}}}, \quad (7)$$

where the value of \mathcal{J}_0 is given by the mode of the (one-dimensional) mass-weighted PDF of \mathcal{J} . At each value of n_{H} in the two-dimensional distribution, we find the local peak in \mathcal{J} . We fit these points to find the optical depth, $\tau_{\text{FUV, eff}}$, as a power-law function of gas density for the R8-4pc model:

$$\tau_{\text{FUV, eff}} = 1.1 \left(\frac{n_{\text{H}}}{10^2 \text{ cm}^{-3}} \right)^{0.7}. \quad (8)$$

For the LGR4-2pc model we find

$$\tau_{\text{FUV, eff}} = 0.8 \left(\frac{n_{\text{H}}}{10^2 \text{ cm}^{-3}} \right)^{1.1}. \quad (9)$$

⁴ In observations, Σ_{FUV} on kpc scales may be obtained directly from (extinction-corrected) UV mapping surveys (e.g. Salim et al. 2007, 2018; Leroy et al. 2019; Hassani et al. 2024), or else estimated from traditional star formation tracers such as extinction-corrected H α emission, radio continuum from bremsstrahlung, or other tracers of photoionized gas (e.g. Kennicutt & Evans 2012). It should be borne in mind, however, that the duration of LyC emission is much shorter than that of FUV for a coeval stellar population, so Φ_{LyC} (and resulting tracers of photoionized gas) will be more variable than Σ_{FUV} (see e.g. Table 5 of Kim et al. 2023b, and Figure 8(a) here). Catalogues of star clusters and associations (e.g. Adamo et al. 2017; Lee et al. 2022) with age and mass measurements can also be combined with theoretical population synthesis to obtain individual source FUV luminosities, averaged over area to obtain Σ_{FUV} .

Equation 7 using these two best fit values is displayed in Figure 10 and Figure 11 as red lines. In Figure 11, we also show Equation 7 using the best fit value of $\tau_{\text{FUV,eff}}$ from the R8-4pc model (Equation 8) with \mathcal{J}_0 given by the LGR4-2pc distribution as a black dashed line.

The distribution of J_{FUV} (or \mathcal{J}) is of interest because FUV radiation is responsible for heating the gas through the photoelectric effect, and variations in J_{FUV} correspond to variations in the heating rate. Since FUV also heats the dust, and the dust reprocesses this emission into the IR, the distribution of FUV radiation is reflected in the spectral energy distributions (SEDs) of thermal IR emission and PAH emission rate. For example, Draine et al. (2007) apply a simplified model of the global FUV intensity distribution with two distinct components to fit the total dust emission in the SINGS galaxy sample. The diffuse radiation has a single uniform value, represented as a delta function distribution, while regions near stars are represented separately with a power law distribution for the radiation intensity.

We fit the distribution of the FUV radiation field in our simulations, considering the mass fraction at the midplane as a function of \mathcal{J} . For both the R8-4pc and LGR4-2pc models, the functional form we adopt for this fit is:

$$\frac{1}{M_{\text{tot}}} \frac{dM}{d\mathcal{J}} = \begin{cases} A_1 \frac{1}{\mathcal{J}\sigma\sqrt{2\pi}} e^{-\frac{(\ln(\mathcal{J})-\mu)^2}{2\sigma^2}} & \mathcal{J} < \mathcal{J}_{\text{trans}} \\ A_2 \mathcal{J}^{-\alpha} & \mathcal{J} \geq \mathcal{J}_{\text{trans}} \end{cases} \quad (10)$$

Here, M_{tot} is the total mass over the whole distribution. For high values of \mathcal{J} , we use a power law with exponent fixed to be $\alpha = 2$ as in Draine et al. (2007), since this value was found to fit most observed galaxies well. We also find $\alpha = 2$ to describe our data well. To represent the peak of the distribution, we use a log-normal function. In our model, the amplitudes, A_1 and A_2 , are determined by the requirement for the piecewise function to be continuous and for the total integral to be equal to one. This leaves three free parameters including the mean and width of the log-normal distribution (μ and σ) as well as the location of the transition from the log-normal to power law distribution ($\mathcal{J}_{\text{trans}}$). In the right panels of Figure 10 and Figure 11, we show the fits together with the PDFs of the normalized intensity \mathcal{J} as measured from the simulations. Parameters for the fits are listed in Table 4.

4.2. Model Comparisons

Ray tracing accurately solves the equations of radiative transfer and resolves the radiation field, but it is computationally intensive. Therefore, it is useful to compare the results of the full TIGRESS-NCR simulations to simplified models of the FUV radiation field,

Table 4. FUV PDF Fit Parameters

Model	μ	σ	$\mathcal{J}_{\text{trans}}$	A_1	A_2	PL Fraction
(1)	(2)	(3)	(4)	(5)	(6)	(7)
R8-4pc	-1.2	0.82	0.6	0.88	0.18	0.3
LGR4-2pc	-1.3	1.5	0.2	1.4	0.08	0.4

NOTE—Columns (2)–(4): best fit values of the function described in Equation 10 for both the R8-4pc and LGR4-2pc models. Columns (5)–(6): normalizations of the log-normal and power law components of the model required for the function to be continuous and integrate to one. Column (7): mass fraction described by the power law component rather than the log-normal.

which potentially may be used when full radiative transfer is not practical. We test four simple models using the R8-4pc model, but we find similar results for LGR4-2pc.

4.2.1. Plane Parallel Model

In the TIGRESS-NCR simulations, a plane parallel approximation is used to calculate the FUV radiation field beyond $|z| = 300$ pc (see Section 2.1.2) as it is too computationally intensive to resolve the full box with ray tracing. In the simulation, this plane-parallel solution has horizontally-averaged intensity as its inner boundary condition (Equation 1 and Equation 2).

A related plane-parallel model can be applied to compute the angle-averaged radiation intensity throughout the domain. For each radiation source particle with luminosity L_{sp} and vertical position z_{sp} , we consider a thin plane-parallel layer that has the source function $S = S_{\text{sp}}\delta(\tau_{\perp})$, where $S_{\text{sp}} = L_{\text{sp}}/(4\pi L_x L_y)$ and $\tau_{\perp}(z; z_{\text{sp}}) = |\int_{z_{\text{sp}}}^z \sigma_{\text{d}} \langle n_{\text{H}} \rangle dz|$ is the dust optical depth measured from z_{sp} in the vertical direction. Solving the plane-parallel radiative transfer equation $\mu dI/d\tau_{\perp} = S - I$ gives the intensity $I(z; \mu) = S_{\text{sp}} e^{-\tau_{\perp}/|\mu|}/|\mu|$ (0 for $\mu \geq 0$ if $z \leq z_{\text{sp}}$) and the mean intensity $J_{\text{p-p}}(z) = S_{\text{sp}} E_1(\tau_{\perp})/2$, where E_1 is the exponential integral. The total FUV mean intensity can be obtained as a superposition of thin layers for individual sources and the summation over frequency bins.

We compare the results of the R8-4pc simulation to the plane parallel approximation in Figure 12. The upper panel shows the horizontally and time averaged FUV mean intensity, $\langle J_{\text{FUV}} \rangle$, as a function of z . The faint gray lines represent individual simulation snapshots and the blue line represents the mean value. We show the mean of the plane parallel model approximation for comparison in orange. The peak of the mean plane-parallel profile agrees well with the full ray-tracing

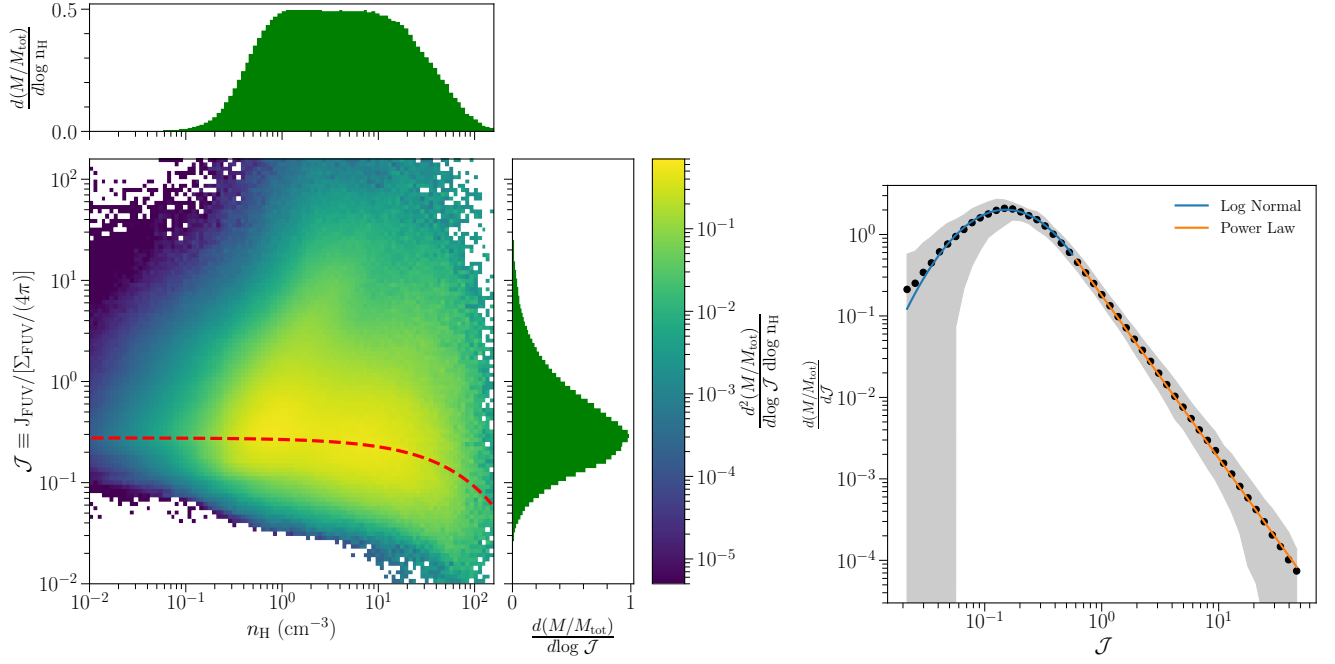


Figure 10. Left: Distribution of mass with normalized mean intensity in the FUV band \mathcal{J} and hydrogen number density n_{H} for the midplane gas in model **R8-4pc** including all snapshots between 250-450 Myr. We limit to gas with $T < 3.5 \times 10^4$ K. Insets show mass-weighted PDFs of $\log \mathcal{J}$ and $\log n_{\text{H}}$. The red dashed line represents the best fit of Equation 7 to the mode of the distribution. Right: The black points represent the mass-weighted PDF of normalized mean intensity \mathcal{J} (rather than $\log \mathcal{J}$ as in the left panel). The overplotted lines represent the best fit of the model given in Equation 10 with the log-normal and power law components represented in blue and orange respectively. The shaded region represents the 16th-84th percentile of the two PDFs of each individual snapshot between 250-450 Myr.

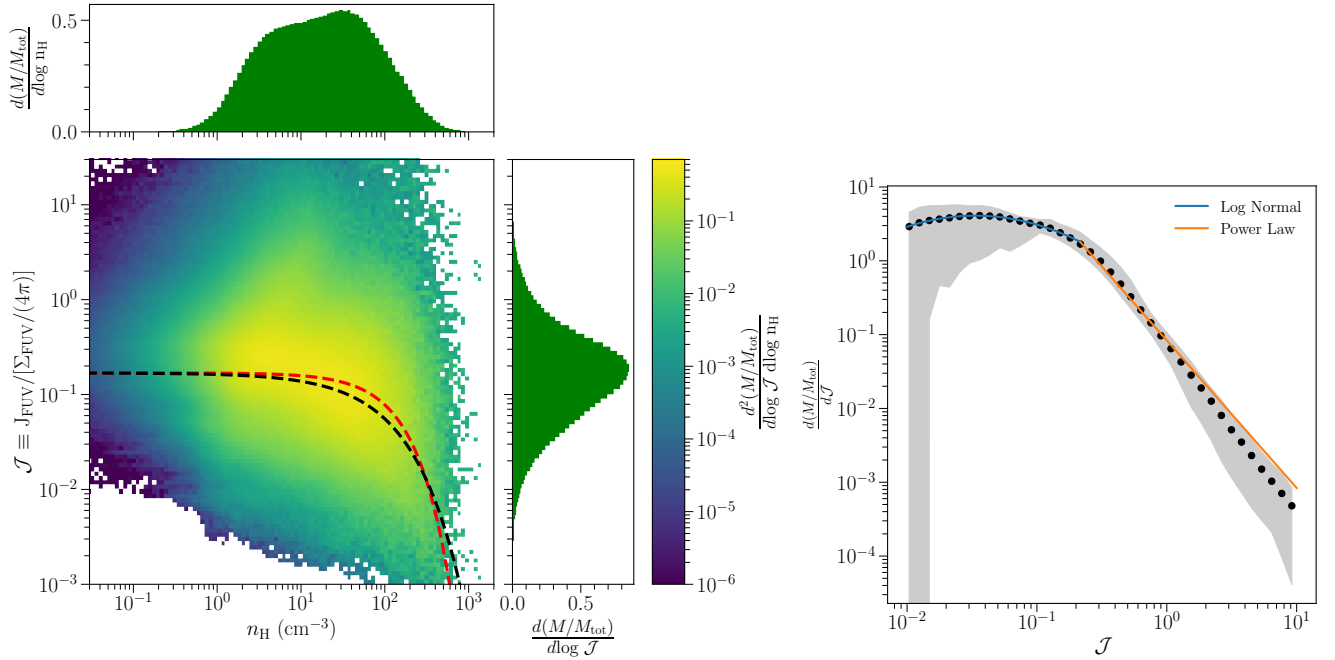


Figure 11. Same as in Figure 10 but for model **LGR4-2pc** over time range 250-350 Myr. The red dashed line represents the best fit of Equation 7 to the mode of the distribution. The black dashed line represents the value of Equation 7 using the value of $\tau_{\text{FUV,eff}}$ fit from the **R8-4pc** model (Equation 8).

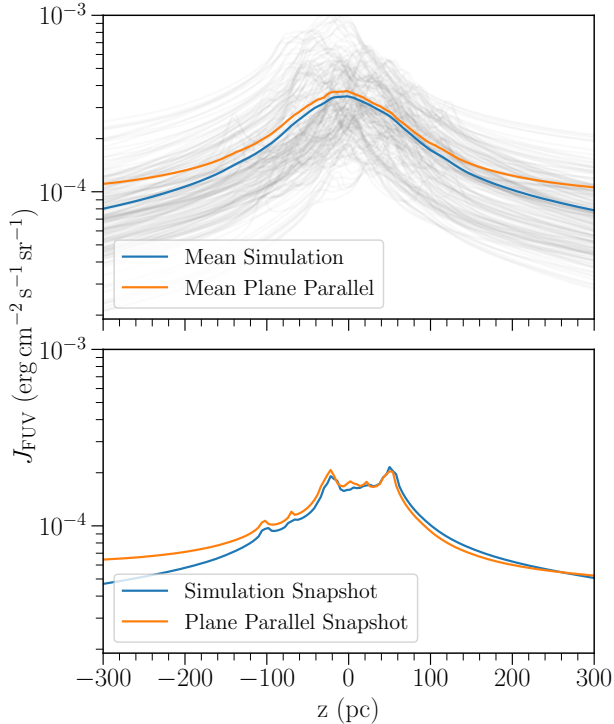


Figure 12. Comparison of the vertical profile of the mean FUV intensity to the plane parallel approximation (see Section 4.2.1) for model R8-4pc. The upper panel shows the average mean intensity as a function of z with individual snapshots shown in gray. The lower panel shows a comparison for a single snapshot at $t = 430$ Myr.

solution. However, by $z = \pm 300$ pc the plane-parallel model exceeds the ray-tracing based result by $\sim 50\%$ averaged in time. This is most likely because 10% of FUV photons are lost due to the ray terminations based on ϵ_{PP} and $d_{xy,max}$ (see Section 2.1.1), meaning that the FUV radiation field is slightly underestimated far from the sources in the ray-tracing based result.

Similar behavior is also seen for individual snapshots rather than the average. This is shown in the lower panel of Figure 12 for $t = 430$ Myr (a radial-vertical slice at the same time is portrayed in Figure 1).

4.2.2. Slab Model

The plane parallel model gives a z -dependent approximation of the FUV radiation field. From Ostriker et al. (2010), an even simpler model is that of a slab with uniform density and opacity such that the total perpendicular optical depth is $\tau_{\perp,FUV}$, and uniform emissivity such that the source function is $S_{FUV} = \Sigma_{FUV}/(4\pi\tau_{\perp,FUV})$. For this system, the intensity at the midplane of the slab is given by $J_{FUV} = S_{FUV}[1 - E_2(\tau_{\perp,FUV}/2)]$ for E_2 the second exponential integral (see Appendix A). The

resulting normalized intensity at the midplane is thus

$$\mathcal{J}_{\text{slab,mid}} \equiv \frac{1 - E_2(\tau_{\perp,FUV}/2)}{\tau_{\perp,FUV}}. \quad (11)$$

The FUV optical depth perpendicular to the slab, $\tau_{\perp,FUV}$ is defined in terms of the gas surface density in the slab, Σ_{slab} , and the FUV opacity, κ_{FUV} , as

$$\tau_{\perp,FUV} = \kappa_{FUV}\Sigma_{\text{slab}} \quad (12)$$

where $\kappa_{FUV} \equiv \sigma_{FUV}/(\mu_H m_H)$ for σ_{FUV} the FUV cross-section and $\mu_H = 1.4$ the mean molecular weight per hydrogen nucleus. The TIGRESS-classic simulations (Kim et al. 2020; Ostriker & Kim 2022) adopt Equation 11 as the radiation model, with $\Sigma_{\text{slab}} = \Sigma_{\text{gas,tot}}$, the total (instantaneous) surface density of all gas.⁵

Using the same uniform-slab model, one can also compute the mean intensity within the slab (as opposed to the midplane). It is straightforward to show that this is:

$$\mathcal{J}_{\text{slab,avg}} \equiv \frac{1}{\tau_{\perp,FUV}} \left[1 - \frac{1}{2\tau_{\perp,FUV}} + \frac{E_3(\tau_{\perp,FUV})}{\tau_{\perp,FUV}} \right], \quad (13)$$

for E_3 the third exponential integral. The functions $\mathcal{J}_{\text{slab,mid}}$ and $\mathcal{J}_{\text{slab,avg}}$ are shown in Figure 26. Both monotonically decrease with increasing optical depth. It is worth noting that both exceed unity at low optical depth.

To get some idea of what the slab model predicts, we can consider typical numbers for these simulations. With a time-averaged gas surface density in the R8-4pc model of $\Sigma_{\text{gas,tot}} = 10.5 M_{\odot} \text{ pc}^{-2}$, and for $\sigma_{FUV} = 10^{-21} \text{ cm}^2$, we find $\tau_{\perp,FUV} = 0.94$, $\mathcal{J}_{\text{slab,mid}} = 0.70$, and $\mathcal{J}_{\text{slab,avg}} = 0.63$. For model LGR4-2pc, $\Sigma_{\text{gas,tot}} = 38.0 M_{\odot} \text{ pc}^{-2}$, $\tau_{\perp,FUV} = 3.4$, $\mathcal{J}_{\text{slab,mid}} = 0.28$, and $\mathcal{J}_{\text{slab,avg}} = 0.25$.

Figure 13 compares the result from full ray tracing to the z -dependent plane parallel approximation (4.2.1) and the simple slab model (Equation 11). Although Equation 13 is nominally more appropriate to compare with the vertically averaged radiation field, we compare with Equation 11 as this was the model adopted for all warm and cold gas in the TIGRESS-classic simulations analyzed in Kim et al. (2020) and Ostriker & Kim (2022). The difference between $\mathcal{J}_{\text{slab,avg}}$ and $\mathcal{J}_{\text{slab,mid}}$ is at most 10% (at $\tau_{\perp} = 2$). The simulation and plane parallel values shown in the upper main panel are volume-weighted averages over all gas within $|z| = 300$ pc of

⁵ In Kim et al. (2020) and Ostriker & Kim (2022), we use the notation f_{τ} for $\mathcal{J}_{\text{slab,mid}}$, and refer to this as an attenuation factor.

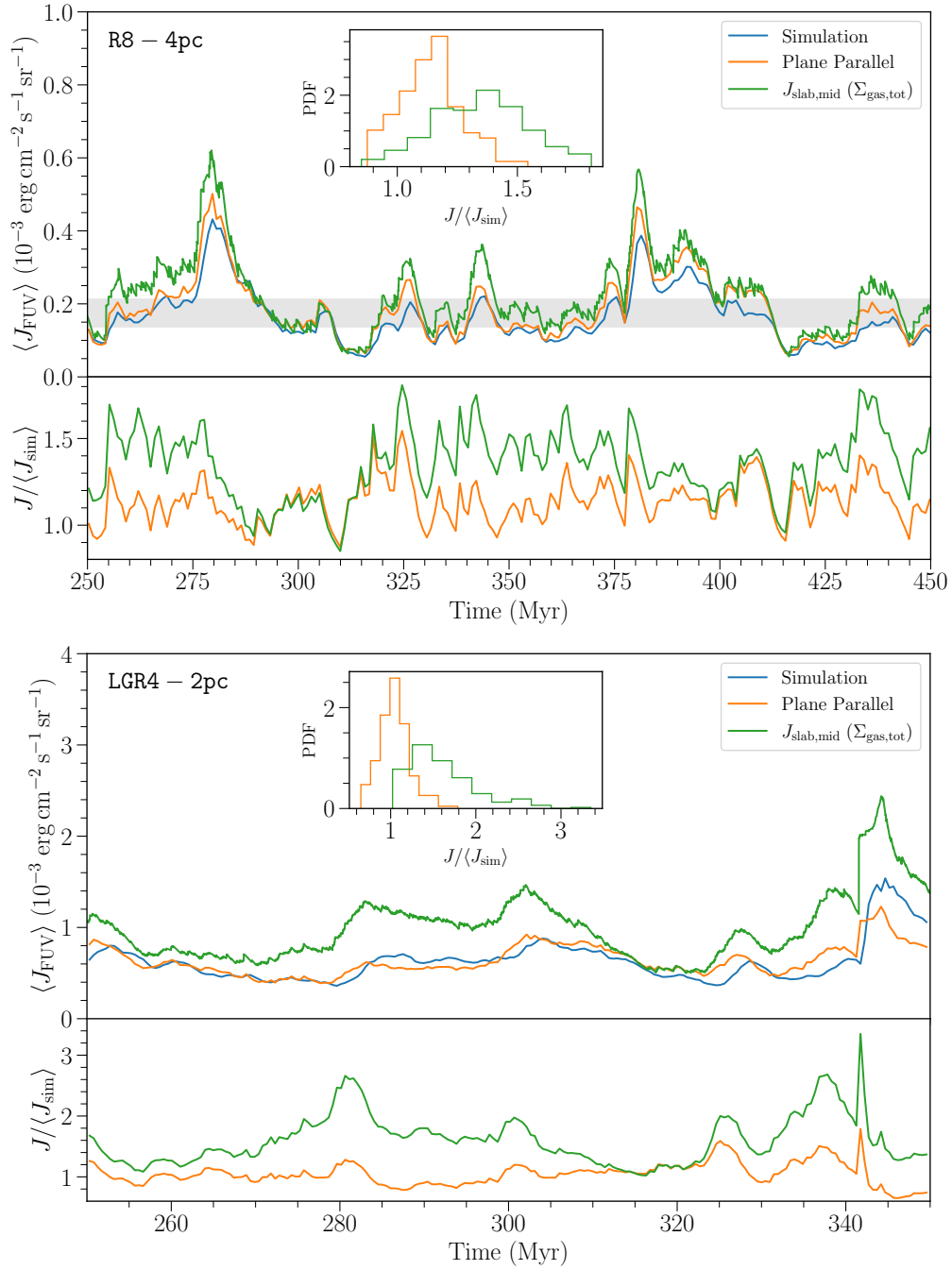


Figure 13. Comparison of the temporal history of the mean FUV intensity from ray tracing to the plane parallel approximation and to the slab approximation (Equation 11) adopted for TIGRESS-classic. The comparison is for the volume-weighted averages within $|z| = 300$ pc of the midplane and is shown for both the R8-4pc model (top) and LGR4-2pc model (bottom). In the upper panel, the gray band represents the range of observed estimates for the solar neighborhood including [Draine \(1978b\)](#), [van Dishoeck & Black \(1982\)](#), and [Mathis et al. \(1983\)](#). The insets show the distributions of the ratio between the model and simulation results.

the midplane (this choice is motivated by the measured scale heights in the simulation – see Table 3). The ratio of the model values, either z -dependent plane parallel or slab, to the simulated values is shown in the lower panel. We include the distribution of these ratios in the inset panel.

Both approximate models track the temporal variations in the mean radiation field well, although the slab model generally exceeds the plane-parallel model, and both exceed the ray-tracing solution. As noted above, the ray-tracing solution will underestimate the true solution at larger $|z|$ due to ray truncation. The plane parallel approximation differs from the simulated value by an average factor of ~ 1.14 (R8-4pc) or ~ 1.05 (LGR4-2pc). The slab model overestimates the simulated value by a mean factor of ~ 1.35 (R8-4pc), or ~ 1.61 (LGR4-2pc). Despite these differences, both approximations do well for being simplified models. Indeed, the slab approximation is remarkably good, considering that it relies only on the average optical depth through the disk and total luminosity per unit area. Since these quantities are straightforward to calculate, the slab approximation could be readily employed for an inexpensive estimate of radiation field in simulations that do not follow radiative transfer and is useful for observational estimates. Our results also show that the radiation prescription adopted for the TIGRESS-classic simulations only modestly overestimated the values that would have been obtained with ray tracing. However, there is substantial local variation in the intensity that cannot be captured by the mean field model, as evidenced by the scatter in the distribution of \mathcal{J} in Figure 10 and Figure 11.

4.2.3. Bialy Model

Bialy (2020) presents another model which estimates the FUV radiation field based on the surface density of FUV luminosity, the mean distance between FUV radiation sources, and the gas density. In the analytic model of Bialy (2020), the average distance between sources in a region is defined as

$$l_* \equiv N_*^{-1/2} \quad (14)$$

for N_* the surface density of source counts. For randomly distributed sources, the median distance between sources is $x_0 l_*$ for $x_0 = 0.47$, which represents the distance to the nearest source from any location. With n_{H} a mean gas number density,

$$\tau_* \equiv l_* n_{\text{H}} \sigma_{\text{d,FUV}} = l_* \rho \kappa_{\text{FUV}} \quad (15)$$

is a characteristic optical depth, and $x_0 \tau_*$ is taken as the optical depth to the nearest source.

In Bialy (2020), the FUV radiation flux at any point is the sum of two terms. The first represents the contribution from the closest point source, and the second represents the total contributions from all other sources treated as a spatially-uniform distribution located at the midplane with a minimum distance $x_0 l_*$. Equation 18 of Bialy (2020) gives the radiation flux F assuming a distribution of Σ_{FUV} that declines exponentially with radius with a scale length $R_d = X l_*$. The flux F can be divided by 4π to obtain \mathcal{J}_{FUV} , or by Σ_{FUV} (Σ_* in the notation of Bialy (2020)) to obtain the normalized intensity,

$$\mathcal{J}_{\text{Bialy}} = \frac{1}{4\pi x_0^2} e^{-x_0 \tau_*} + \frac{1}{2} E_1(x_0 \tau_* + x_0/X). \quad (16)$$

Similar to the slab model, $\mathcal{J}_{\text{Bialy}}$ monotonically decreases with increasing optical depth τ_* (we compare the two functions in Appendix A – see Figure 26). For application to our simulation, X is effectively infinite because we are using a local simulation box. Therefore, we ignore the second term in the argument of the exponential integral. Physically, $1/(\tau_* X) = 1/(n_{\text{H}} \sigma_{\text{FUV}} R_d)$ is equal to the ratio of photon mean free path to disk radial scale length, which is small for massive star-forming galaxies. In Equation 16, the second term is larger than the first term for $\tau_* < 1.6$, but becomes increasingly subdominant for larger τ_* . We note that as N_* increases, τ_* decreases, which leads to an overall increase in $\mathcal{J}_{\text{Bialy}}$ and an increase in the second term relative to the first.

A caveat regarding this model is that for the purpose of making observational estimates, the gas volume density is not directly accessible. Estimating a midplane or volume-weighted value of the density requires dividing a measured gas surface density by an estimate of the gas disk’s thickness, which generally depends on an assumption of vertical dynamical equilibrium and therefore does not track temporal variations in n_{H} . That is, an empirical estimate would be $\tau_* \sim \tau_{\perp, \text{FUV}} l_*/(2H)$. Here, we are able to use measured values of n_{H} which are available from the simulation, and we also compare to the case where n_{H} is estimated from the surface density.

In our simulation, we determine N_* by dividing the number of star cluster particles in the simulation box by the horizontal area of the region. We limit the number of sources to those which contribute 90% of the total FUV luminosity. This results in a time-averaged source density $N_* = 12.7 \text{ kpc}^{-2}$ for the R8-4pc model, and an average value of $l_* = 290 \text{ pc}$ (Figure 8(d) shows temporal variations of l_*). For Equation 15 we either set the gas number density equal to the mean midplane value or to the mean value within $|z| < H$, where H is the scale height at each time (with an average value of $220 \pm 40 \text{ pc}$). As for the slab model we include all gas,

and we average over the whole horizontal area. Respectively, this yields $n_{\text{H}} = 0.93 \text{ cm}^{-3}$ so that $\tau_* = 0.84$, or $n_{\text{H}} = 0.57 \text{ cm}^{-3}$ so that $\tau_* = 0.51$, averaging over time. Using midplane (or $|z| < H$) numbers, the first term in Equation 16 is equal to 0.24 (0.28), the second term is equal to 0.36 (0.54), and their sum is $\mathcal{J}_{\text{Bialy}} = 0.60$ (0.82). This total is $\sim 14\%$ smaller ($\sim 30\%$ larger) than $\mathcal{J}_{\text{slab,mid}}$ ($\mathcal{J}_{\text{slab,avg}}$) for the same model.

For a more detailed comparison, in Figure 14 we show for model R8-4pc both the midplane and volume-weighted mean normalized intensity, \mathcal{J} , in the simulation, in comparison to the three approximate models. These averages are done including all gas. As noted above, the temporal tracking of variations in the radiation field seen here in $\mathcal{J}_{\text{Bialy}}$ is possible in large part because n_{H} is directly measured. If we instead use $\tau_* = \tau_{\perp,\text{FUV}} l_*/(2H)$ for H an estimated mean disk thickness (adopting 220 pc here), the majority of variation in the radiation would be due to the changing value of $l_* = N_*^{-1/2}$. This does not track the variations in the simulated \mathcal{J} as closely, as shown in the dashed curves in Figure 14.

Considering $\mathcal{J}_{|z|<300\text{pc}}$ with directly measured values of n_{H} , the Bialy (2020) model overestimates the ray-tracing value by an average factor of approximately 1.6. Although this approximation still does well as a simplified estimate, the slab approximation (Equation 13) is somewhat closer in mean value (a factor 1.2 times the simulation value, on average). For the prediction of Equation 16 to more closely match the intensity found with full radiative transfer, τ_* would have to be larger by a factor of two. This would require a much lower source density, $N_* \sim 4 \text{ kpc}^{-2}$, i.e. four sources in the simulation domain. If we instead consider only the midplane, the average value of n_{H} is greater so the modeled value of $\mathcal{J}_{\text{Bialy}}$ is smaller. At the same time, the simulated \mathcal{J}_{sim} is larger at the midplane. These effects compound so that $\mathcal{J}_{\text{Bialy}} \sim 0.6 \mathcal{J}_{\text{sim}}$. The mean value of $\mathcal{J}_{\text{Bialy}}$ using the measured midplane density is similar to that from Equation 11.

The plane parallel model follows the simulation very closely, both at the midplane and volume-averaged, and for this reason we recommend it as an inexpensive alternative when full radiative transfer is not practical but close tracking of the mean radiation field is desirable.

4.2.4. FUV Sum of Sources Model

The previous models of the FUV radiation field are useful in describing the average intensity across the simulation volume. To find an estimate for the FUV radiation at any point when the locations and luminosities of sources are known, we can instead model the contribu-

tion of each individual source particle to the total flux. In this case, the approximate FUV intensity is given by

$$J_{\text{FUV,src}} = \frac{1}{4\pi} \sum_{\text{sources } i,b} \frac{L_{i,b}}{4\pi r_i^2} e^{-r_i \langle n_{\text{H}} \rangle \sigma_{\text{d},b}}, \quad (17)$$

where $L_{i,b}$ is the luminosity of source i in band b (LW and PE), r_i is the distance to the source, $\langle n_{\text{H}} \rangle$ is the mean ambient ISM density within one scale height of the midplane (Equation 5), and $\sigma_{\text{d},b}$ is the dust absorption cross section in band b . For this comparison, we include only the sources with $t_{\text{age}} < 20 \text{ Myr}$ and horizontal distance less than $d_{xy,\text{max}}$ from each cell, consistent with our practice for ray-tracing. We consider sources from a horizontally extended domain by applying the shearing-periodic boundary conditions. For $\langle n_{\text{H}} \rangle$, we take the average density within one scale height of the midplane.

Equation 17 models geometric attenuation correctly, but it is approximate because it uses a single average density $\langle n_{\text{H}} \rangle$ rather than allowing the density to vary along rays. This may lead to an overestimation of J_{FUV} in dense regions, where the density exceeds $\langle n_{\text{H}} \rangle$ and the photon mean free path decreases. To address this issue, we also consider a model including local attenuation

$$J_{\text{src,att}} = J_{\text{FUV,src}} e^{-\tau_{\text{eff,local}}}, \quad (18)$$

where $\tau_{\text{eff,local}}$ is given by the best fit relationship between \mathcal{J} and density in Equation 7, using the local value of n_{H} in each cell in Equation 8.

An example of the midplane intensity from ray-tracing compared to the sum of sources models for the R8-4pc simulation is given in Figure 15 for $t = 430 \text{ Myr}$. Qualitatively, the model described in Equation 17 matches the simulated values well, especially in the warm-phase diffuse gas. In particular, for the snapshot shown here, $\sim 82\%$ of cells are within a factor of two of the true FUV radiation value; this is true for $\sim 83 \pm 9\%$ of cells including all snapshots. The distribution of the ratio between the approximate and simulated values of J_{FUV} is shown in the left panel of Figure 16.

With the addition of local attenuation in the model given by Equation 18, some high density regions show significantly more attenuation, and now $\sim 84\%$ of cells are within a factor of two of the true FUV radiation value. However, there are still significant differences between the true FUV radiation and the model in regions with higher than average density. This can be seen for one snapshot in the far right panel of Figure 15, and across all snapshots in Figure 16.

Even at lower density, the true intensity is lower than Equation 18 ($J_{\text{sim}} \sim 0.79 J_{\text{src,att}}$ averaged over the warm phase for a single snapshot, or a factor of ~ 0.76 more

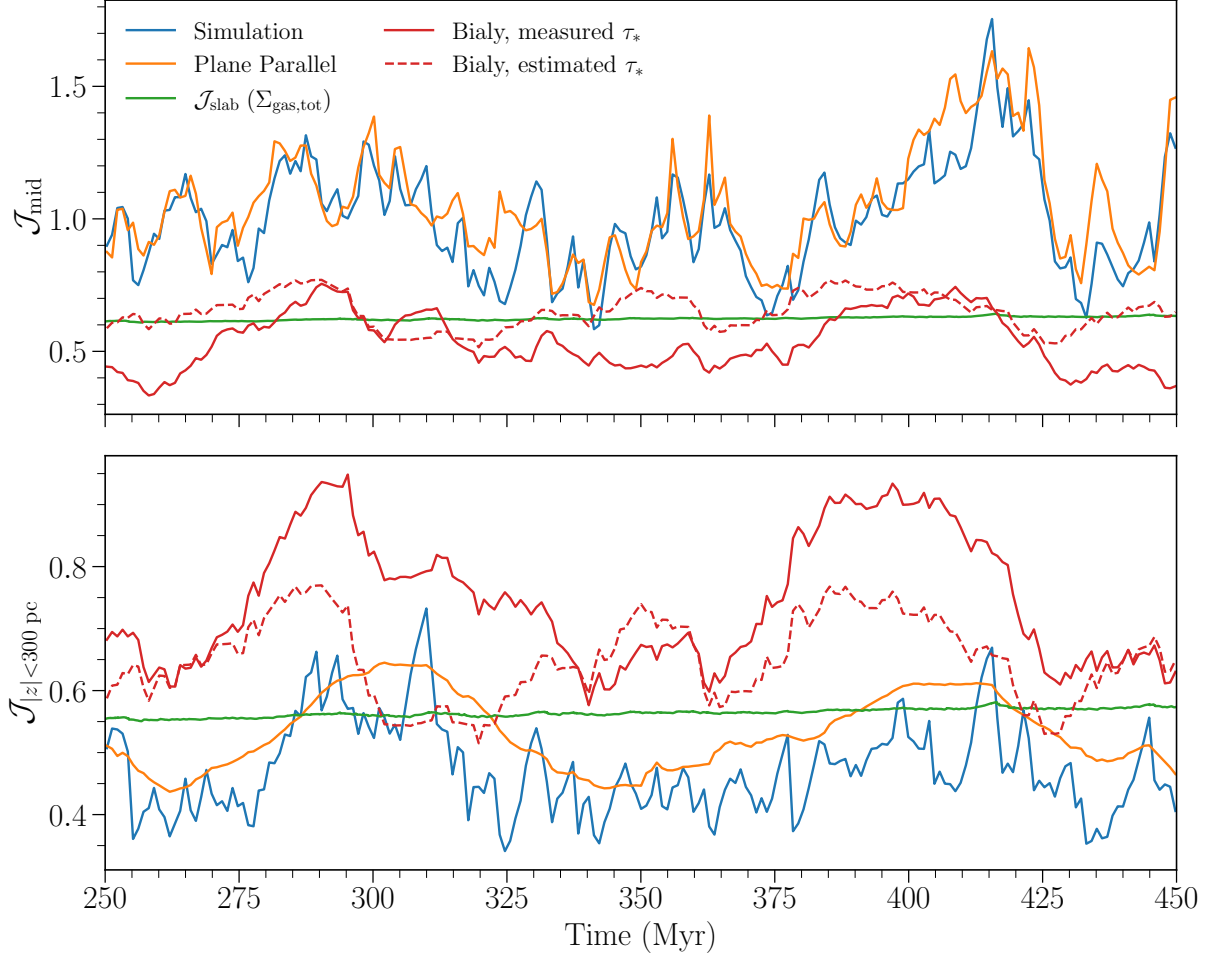


Figure 14. Comparison of the normalized mean FUV radiation intensity \mathcal{J} from the simulation (R8-4pc) with different approximate models, as described in Section 4.2.1- Section 4.2.3. *Top:* Values are computed at the midplane. *Bottom:* Values represent a volume weighted average within 300 pc of the midplane. In the upper panel, $\mathcal{J}_{\text{slab}}$ uses Equation 11; in the lower panel, $\mathcal{J}_{\text{slab}}$ uses Equation 13. The solid red curves use measured midplane or volume-averaged densities to evaluate $\tau_* = l_* \rho \kappa_{\text{FUV}}$, while the dashed curves use the measured surface density and the mean value of $\langle H \rangle$ to estimate $\tau_* = l_* \Sigma_{\text{gas}} \kappa_{\text{FUV}} / (2 \langle H \rangle)$.

generally), because of the higher-than average attenuation in dense gas around sources. Still, the local attenuation factor is helpful in reducing the bias toward overestimating the radiation field in dense regions, as comparison of the right with the left of Figure 16 shows.

4.3. FUV Heating Rate and Dust Emission

Interstellar dust is heated by stellar FUV radiation⁶, and re-radiates the energy that is absorbed over a wide range of wavelengths. Dust SEDs therefore reflect both the distribution of physical properties of grains (which

vary in size over orders of magnitude, with composition including both hydrocarbons and silicates – see e.g. Hensley & Draine (2023) and references therein), and the radiation intensity J_ν over a range of frequencies that the grains are exposed to. Additionally, the spatial distribution of dust emission at any given wavelength depends not only on the distribution of the dust but also of the radiation field.

Considering a given grain type with abundance q , the observed emission at a given wavelength per unit area per unit time will be proportional to an integral over path length and frequency of $qn_{\text{H}}J_\nu$. If we take our simulations as representing a patch of the ISM in a face-on disk galaxy, the dust emission due to FUV absorption will therefore be proportional to a dust heating parameter

$$\mathcal{N}_d(x, y) \equiv \int \mathcal{J} n_{\text{H}} dz \quad (19)$$

⁶ Stellar optical (and near-UV) radiation also contributes to dust heating, although in the present work we do not consider optical radiative transfer since the optical does not heat the gas. In the local interstellar medium, the dust heating of larger grains by optical photons is at a level of $\sim 50\%$ of the FUV (e.g., see Fig. 26 in Kim et al. 2023b)

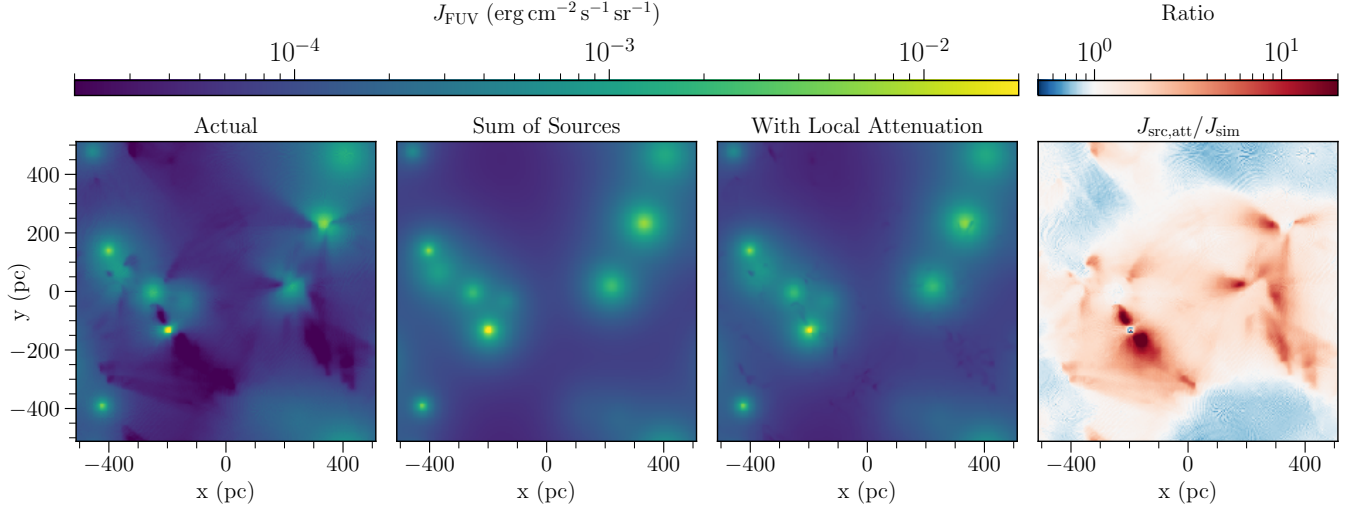


Figure 15. From left to right, the midplane FUV intensity J_{FUV} for model R8-4pc at $t = 430$ Myr in comparison to the model based on the contribution from a sum over attenuated FUV sources (Equation 17) and the same model with local attenuation (Equation 18). The far right panel represents the ratio of the attenuated sum of sources model to the true FUV radiation field.

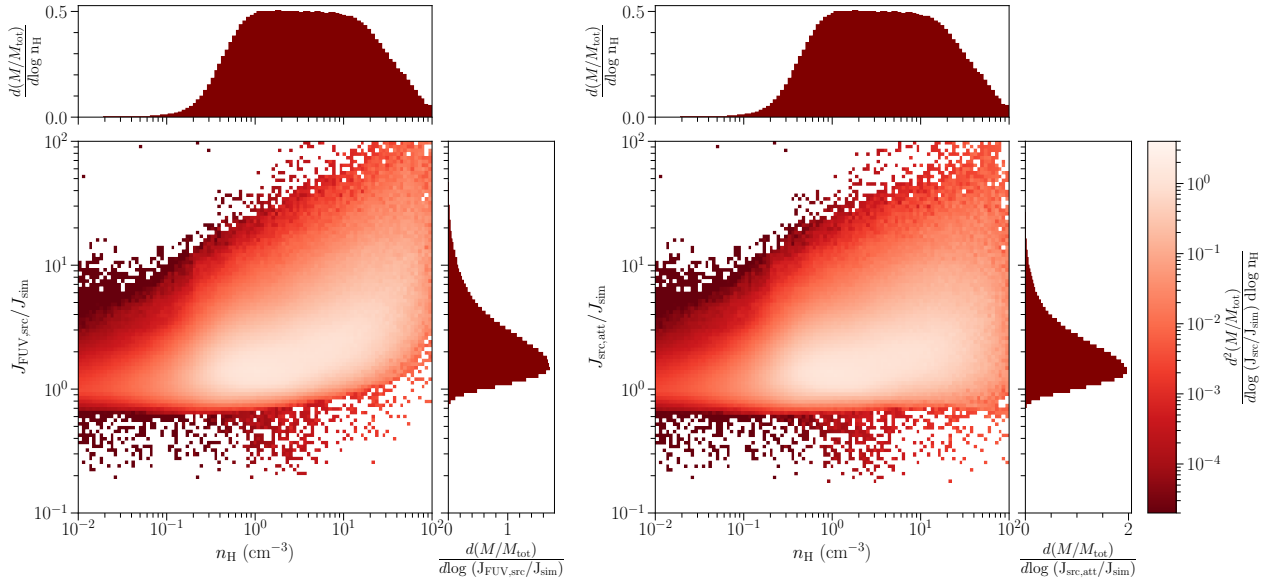


Figure 16. Distribution of mass as a function of the ratio of the true FUV radiation field to the estimate based on attenuated sum over sources models and the local density. On the left is the model given by Equation 17 and on the right is the model with additional local attenuation given by Equation 18. Results are based on ~ 200 snapshots from the R8-4pc model between $t = 250$ –450 Myr considering only the midplane ($z = 2$ pc).

where we use the normalized FUV intensity \mathcal{J} of Equation 6. That is, the dust emission at (x, y) will convolve over $n_{\text{H}}(x, y, z)$ and $\mathcal{J}(x, y, z)$. To obtain the FUV-induced dust emission at a given frequency and location, one would multiply \mathcal{N}_d by the dust abundance, by the mean local UV production rate $\Sigma_{\text{FUV}}/(4\pi)$, and by factors for FUV absorption crosssection and emissivity at the frequency of interest. While larger grains absorb essentially all radiation and emit primarily at far-IR wavelengths, PAHs are believed to be excited primarily

by absorption of FUV and have strong mid-IR emission (Tielens 2008; Hensley & Draine 2023). Mid-IR emission maps, as are now available at high resolution with *JWST* (e.g. Leroy et al. 2023; Pathak et al. 2024), are therefore sensitive to a similar radiation distribution (in space, time, and frequency) to the radiation field that heats the gas via PE.

Figure 1–Figure 4 show that there are large spatial variations in both density and the FUV radiation field. The variation in the gas density, however, is larger over-

all than the variation in normalized radiation intensity (see [Figure 10](#) and [Figure 11](#)), so the spatial structure in dust emission may potentially be employed as a proxy of spatial structure in the gas (e.g. [Pathak et al. 2024](#)).

Based on our simulations, in the first two rows of [Figure 17](#) we compare the spatial structure of gas column density $N_{\text{H}}(x, y) \equiv \int n_{\text{H}} dz$ with [Equation 19](#), for the same snapshots shown in [Figure 3](#) and [Figure 4](#). We remove the hot gas by restricting to $T < 3.5 \times 10^4$ K. In hot gas, the PAH lifetime would be short so we would not expect significant dust emission (e.g. [Bocchio et al. 2012](#)). We renormalize the dust heating parameter (\mathcal{N}_d) by a constant (ϕ_s) such that it has the same median value as N_{H} for $N_{\text{H}} < 10^{21} \text{ cm}^{-2}$; operationally this divides [Equation 19](#) by the typical \mathcal{J} of atomic regions.⁷ Evidently, \mathcal{N}_d/ϕ_s shows small-scale structures in the gas column density quite well but is systematically elevated compared to N_{H} in the neighborhood of sources, as would be expected from the enhancement of the radiation field in these regions (see also [Figure 15](#)).

Considering the potential of using high-resolution dust emission maps to trace gas column, it is interesting to test whether approximate radiation solutions can be used to correct for varying heating. To this end, the third row of [Figure 17](#) shows

$$N_{\text{H,est}} \equiv \frac{\mathcal{N}_d}{\mathcal{J}_{\text{src},\perp} \phi_s}, \quad (20)$$

where $\mathcal{J}_{\text{src},\perp} \equiv J_{\text{src},\perp}/(\Sigma_{\text{FUV}}/4\pi)$ for $J_{\text{src},\perp}$ as in [Equation 17](#), but with r_i the projection of distance onto the (x, y) plane at a z value representing the average height of a source particle above the midplane ($z = 45 \text{ pc}$). We again renormalize by a value of ϕ_s such that the median value of $N_{\text{H,est}}$ is the same as N_{H} for $N_{\text{H}} < 10^{21} \text{ cm}^{-2}$.

Compared to the map of \mathcal{N}_d/ϕ_s , the map of $N_{\text{H,est}}$ shows reduced elevation around the source particles particularly in the R8-4pc model. The distributions of both \mathcal{N}_d/ϕ_s and $N_{\text{H,est}}$ compared to N_{H} are shown in the final row [Figure 17](#) as contours. Both proxies of dust emission probe N_{H} well at low column densities. This would be expected as the values are normalized for $N_{\text{H}} < 10^{21} \text{ cm}^{-2}$ and the radiation field is relatively uniform in low-density gas. At higher column, \mathcal{N}_d/ϕ_s is more biased towards overestimating N_{H} when compared to $N_{\text{H,est}}$.

⁷ In observations, the equivalent would be to renormalize mid-IR maps such the median value matches the median column of N_{H} from 21 cm emission in atomic-dominated regions; this empirically calibrates for dust abundance as well as UV absorption and IR emission coefficients and the mean J_{FUV} . [Lenz et al. \(2017\)](#), for example, find a linear relation between N_{H} and dust reddening for $N_{\text{H}} < 4 \times 10^{20} \text{ cm}^{-2}$.

More generally, in [Figure 18](#) and [Figure 19](#) we show the distributions of gas column N_{H} vs. \mathcal{N}_d/ϕ_s and $N_{\text{H,est}}$, considering all times for both models. We see that overall, both versions of the dust heating parameter follow the total gas column with an approximately linear relationship. Below a column density of $2 \times 10^{20} \text{ cm}^{-2}$, the standard deviation in \mathcal{N}_d/ϕ_s at fixed N_{H} is only $\sim 10 - 30\%$ of the mean for R8-4pc. This increases to much larger variance in \mathcal{N}_d at high N_{H} , however. We conclude that dust emission statistically traces gas column well, but it should be borne in mind that there will be significant scatter about the mean at high column. The scatter in $N_{\text{H,est}}$ is similar at low column, and reduced compared to \mathcal{N}_d at high N_{H} .

We fit a log-normal to the PDFs of N_{H} , \mathcal{N}_d/ϕ_s , and $N_{\text{H,est}}$. For R8-4pc, the standard deviation in the distribution of $\ln(\mathcal{N}_d/\phi_s)$ is 0.94 for R8-4pc, which is larger than that in $\ln(N_{\text{H}})$ of 0.71. The standard deviation of $\ln(N_{\text{H,est}})$ is smaller at 0.67. For LGR4-2pc, the standard deviations are 1.2, 0.66, and 0.88 for $\ln(\mathcal{N}_d/\phi_s)$, $\ln(N_{\text{H}})$, and $\ln(N_{\text{H,est}})$ respectively. Thus, we expect that the varying radiation field will enhance the appearance of structure within the ISM based on dust maps, compared to what is present in the gas itself (if comparable resolution were available). Some of this excess variation can be reduced if a model radiation field is applied, as correction by our simple sum of sources model demonstrates. We note that since [Equation 17](#) uses the mean density in computing optical depth, this method would need to be applied iteratively, with the density obtained from the mean column density of the previous iteration and an estimate of the disk scale height.

Finally, we note that to determine the total dust emission at a given frequency, one would need to take into account optical (OPT), near-UV (NUV), and LyC radiation that emitting grains absorb, in addition to FUV. Optical radiation from older stars is important in heating larger grains. Because the older stellar population is relatively smooth, an approximate estimate of J_{OPT} may be able make use of the slab model outlined in [Section 4.2.2](#) and [Appendix A](#).

5. LYC RADIATION FIELD

We now discuss the properties of the simulated LyC radiation field. Unlike the FUV radiation, these photons are strongly attenuated by neutral hydrogen and are responsible for ionization of the gas. Therefore, we will explore the ionization state of the WIM in relation to the LyC radiation field. We will also compare the LyC radiation field in the simulations with approximate models.

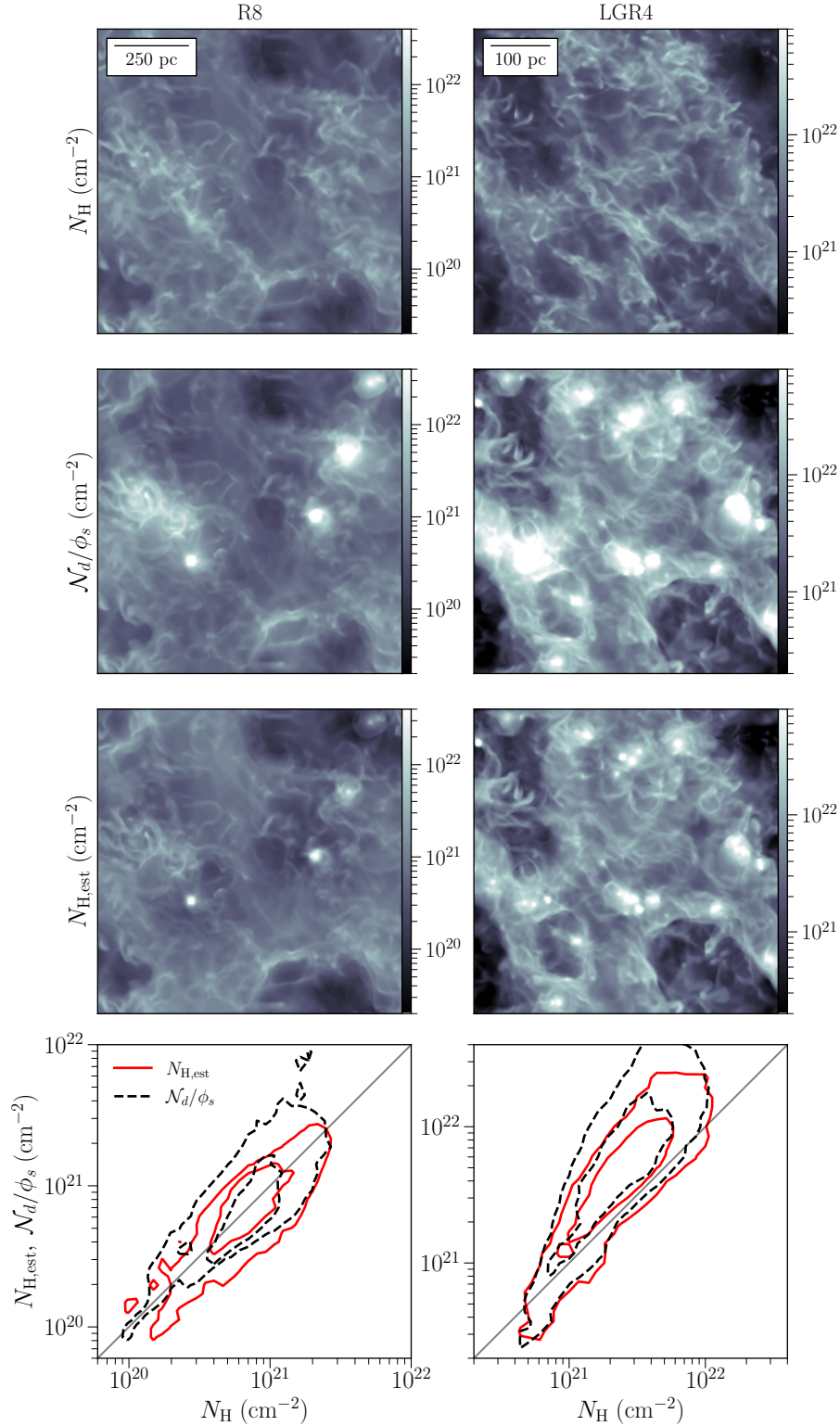


Figure 17. Snapshots of the column density, N_H (first row) and the dust heating parameter \mathcal{N}_d from Equation 19 renormalized by a constant factor ϕ_s (second row), and the estimate $N_{H,\text{est}}$ from Equation 20 that applies a correction based on the sum of sources radiation map (third row). The final row gives contours of both $N_{H,\text{est}}$ and \mathcal{N}_d/ϕ_s compared to N_H representing the 50th and 90th percentiles by area. These are shown for the R8-4pc simulation at time $t = 430$ Myr (left), and for the LGR4-2pc simulation at time $t = 298$ Myr (right). The gray lines in the final row show where \mathcal{N}_d/ϕ_s or $N_{H,\text{est}}$ are equal to N_H .

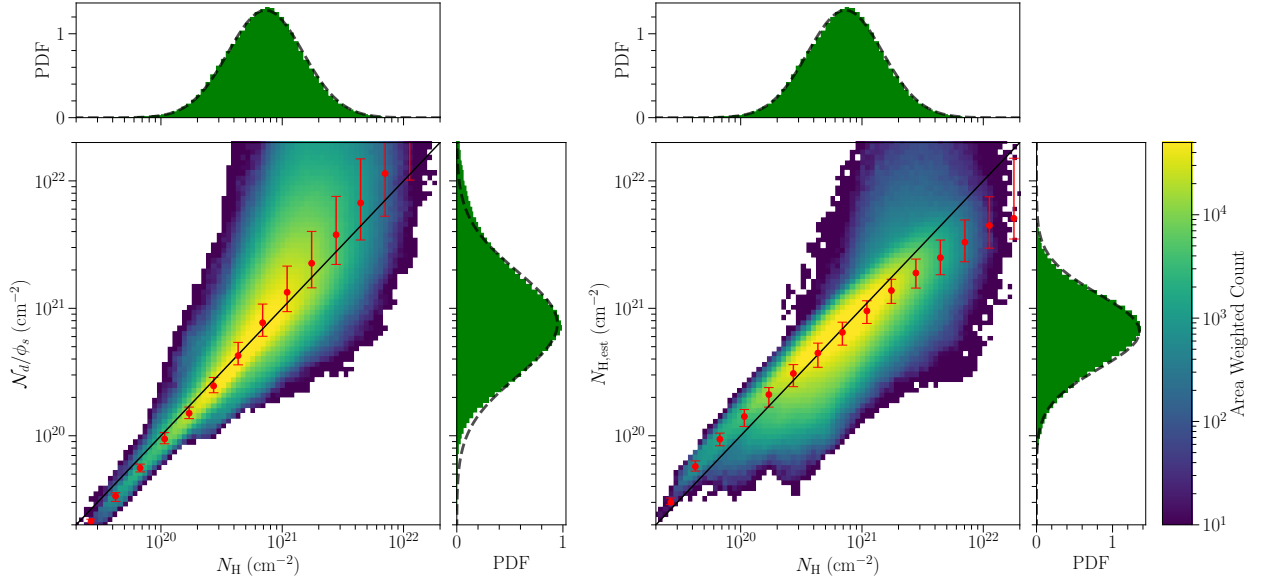


Figure 18. Distribution of the renormalized dust heating parameter \mathcal{N}_d/ϕ_s (left, see Equation 19) and $N_{H,\text{est}}$ (right, see Equation 20) vs. gas column N_H . Both distributions include all snapshots from the R8-4pc simulation between 250–450 Myr. The inset axes represent the projections of the two dimensional histogram into one dimension. A log-normal fit is plotted over each of the one dimensional distributions. The red points represent the median and 25th-75th percentile values of \mathcal{N}_d/ϕ_s or $N_{H,\text{est}}$ within individual N_H bins. The black lines show where \mathcal{N}_d/ϕ_s or $N_{H,\text{est}}$ are equal to N_H .

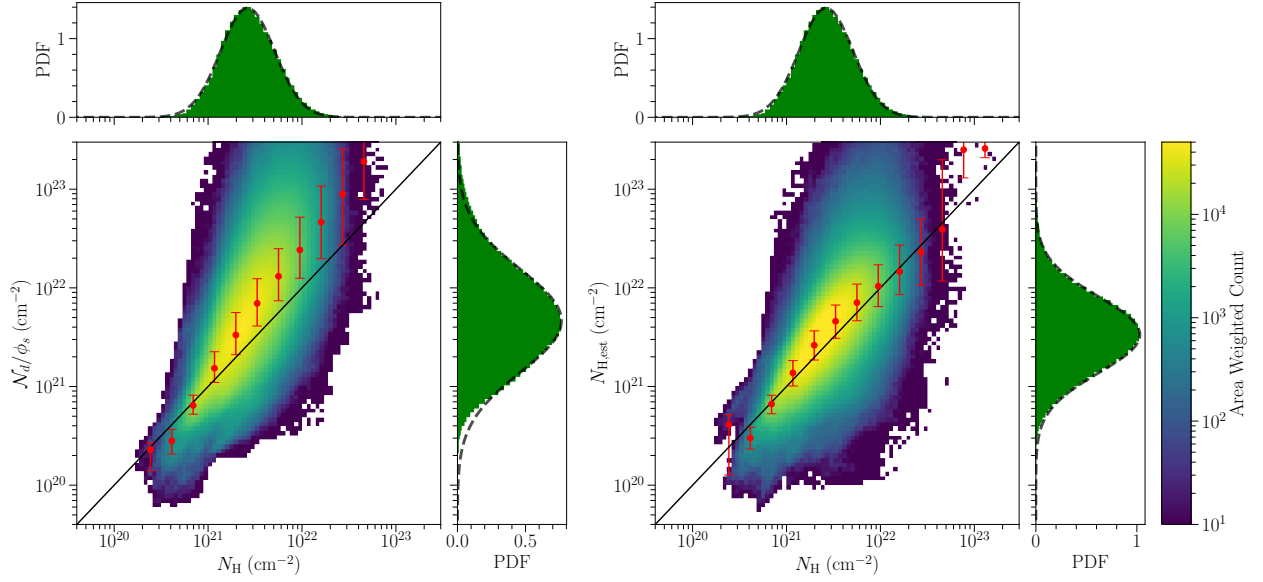


Figure 19. Same as Figure 18 but for the LGR4-2pc simulation between 250–350 Myr.

5.1. Ionization Equilibrium and the Ionization Parameter U

We can determine the extent to which gas is in ionization equilibrium using the energy density of the ionizing radiation. The ionization parameter, U , is defined as:

$$U = \frac{n_{\text{ph}}}{n_{\text{H}}} = \frac{\mathcal{E}_{\text{LyC}}/(h\nu_{\text{LyC}})}{n_{\text{H}}}, \quad (21)$$

where n_{ph} is the number density of ionizing photons, n_{H} is the total number density of hydrogen, \mathcal{E}_{LyC} is the energy density of the ionizing radiation field, and $h\nu_{\text{LyC}}$ is the average photon energy of a single ionizing photon (a blackbody with $T = 3.5 \times 10^4$ K has $h\nu_{\text{LyC}} = 18$ eV and we adopt this as a typical value). In ionization-recombination equilibrium, we would expect

$$\alpha_B n_e n_{\text{H}^+} = n_{\text{HI}} \sigma_{\text{pi}} \frac{c\mathcal{E}_{\text{LyC}}}{h\nu_{\text{LyC}}} = n_{\text{HI}} \zeta_{\text{pi}} \quad (22)$$

where $\alpha_B \approx 3.12 \times 10^{-13} (T/8000 \text{ K})^{-0.83} \text{ cm}^3 \text{ s}^{-1}$ is the case B recombination rate coefficient, σ_{pi} is the photoionization cross section, and ζ_{pi} is the photoionization rate (the probability per unit time of photoionization of a hydrogen atom) (Kim et al. 2023b). This ignores collisional ionization and cosmic ray ionization, which are unimportant unless the LyC radiation field is very weak, and grain-assisted recombination, which is insignificant in warm ionized gas (Weingartner & Draine 2001b). Assuming that the molecular fraction is small so that all hydrogen is either H I or H II ($x_n = x_{\text{HI}} \approx 1 - x_{\text{H}^+}$) and that most free electrons come from hydrogen ($x_e \approx x_{\text{H}^+}$), this can be rewritten in terms of x_n and U :

$$\frac{(1 - x_n)^2}{x_n} \approx \frac{x_{\text{H}^+} x_e}{x_{\text{HI}}} = \frac{U}{U_{\text{crit,pi}}}. \quad (23)$$

Here,

$$U_{\text{crit,pi}} \equiv \frac{\alpha_B}{\sigma_{\text{pi}} c} = 3.34 \times 10^{-6} \times \left(\frac{\alpha_B}{3 \times 10^{-13} \text{ cm}^3 \text{ s}^{-1}} \right) \left(\frac{\sigma_{\text{pi}}}{3 \times 10^{-18} \text{ cm}^2} \right)^{-1} \quad (24)$$

is the critical ionization parameter defined such that the warm ionized gas would be fully ionized ($x_n \ll 1$) as long as $U \gg U_{\text{crit,pi}}$. If $U/U_{\text{crit,pi}} = 1/2$, then $x_n = 1/2$.

In Figure 20, we present a two-dimensional histogram of the ionization parameter, $U/U_{\text{crit,pi}}$, in relation to $x_{\text{H}^+} x_e / x_{\text{HI}}$. We show the total distribution for both models across time, restricting to gas at the midplane. We include only warm gas with temperature between $T = 6 \times 10^3$ and 3.5×10^4 K, and further limit to

gas with $\mathcal{E}_{\text{LyC}} > 0$. With this distribution, we include a black dashed line defined by Equation 23. For $x_{\text{H}^+} x_e / x_{\text{HI}} > 10$ (corresponding to $x_n \lesssim 0.1$), the density peak in the histogram closely follows this line and we conclude that the gas near the midplane is close to ionization-recombination equilibrium.

The absorption rate of LyC photons by dust is $\sigma_d n_{\text{H}} c \mathcal{E}_{\text{LyC}} / (h\nu_{\text{LyC}})$, so we can define a second critical ionization parameter as the maximum value such that the photoionization rate exceeds the dust absorption rate. For well-ionized gas, this is

$$U_{\text{crit,d}} \equiv \frac{\alpha_B}{\sigma_d c} = 0.01 \times \left(\frac{\alpha_B}{3 \times 10^{-13} \text{ cm}^3 \text{ s}^{-1}} \right) \left(\frac{\sigma_d}{10^{-21} \text{ cm}^2} \right)^{-1}. \quad (25)$$

For $U_{\text{crit,pi}} < U < U_{\text{crit,d}}$, the gas will be well ionized and most of the ionizing photons will be absorbed by hydrogen rather than dust.

In Figure 21 we show the two-dimensional distributions of U and n_{H} at $t = 430$ Myr for the R8-4pc simulation and $t = 298$ Myr for LGR4-2pc. We include only the WIM within $|z| < 300$ pc. Each cell is weighted by mass. Figure 22 shows the same values for each model but includes all snapshots, while being limited to gas at the midplane ($|z| < 4$ pc or $|z| < 2$ pc respectively). All of the distributions have a single primary peak, as well as an extension to lower value of U . Physically, this extension represents the edges of ionized regions, where the radiation field drops off sharply and gas becomes neutral.

The red and black horizontal lines in these figures represent $U_{\text{crit,pi}}$ (Equation 24) and $U_{\text{crit,d}}$ (Equation 25), respectively. Most of the distribution falls between the two critical ionization parameters, meaning that it is well ionized and that the photoionization rate exceeds the dust absorption rate.

The diagonal lines represent constant values of the LyC energy density \mathcal{E}_{LyC} for a given photon energy (18 eV) (see Equation 22). Note that for $\mathcal{E}_{\text{LyC}} = 10^{-14} \text{ erg cm}^{-3}$ and $\sigma_{\text{pi}} = 3 \times 10^{-18} \text{ cm}^2$, the corresponding photoionization rate is $\zeta_{\text{pi}} = 3.1 \times 10^{-11} \text{ s}^{-1}$. Along each axis, we show projections of the two-dimensional distribution into distributions of n_{H} and U alone. In Figure 21, the overall peaks of the distributions occur at $U \sim 4 \times 10^{-4}$ and $n_{\text{H}} \sim 0.4 \text{ cm}^{-3}$ in the R8-4pc snapshot and $U \sim 1 \times 10^{-3}$ and $n_{\text{H}} \sim 2.2 \text{ cm}^{-3}$ in the LGR4-2pc snapshot.

Based on the theory of pressure-regulated, feedback-modulated star formation (see Ostriker & Kim 2022, and references therein), we expect thermal pressure and therefore the density of the warm (WNM and WIM)

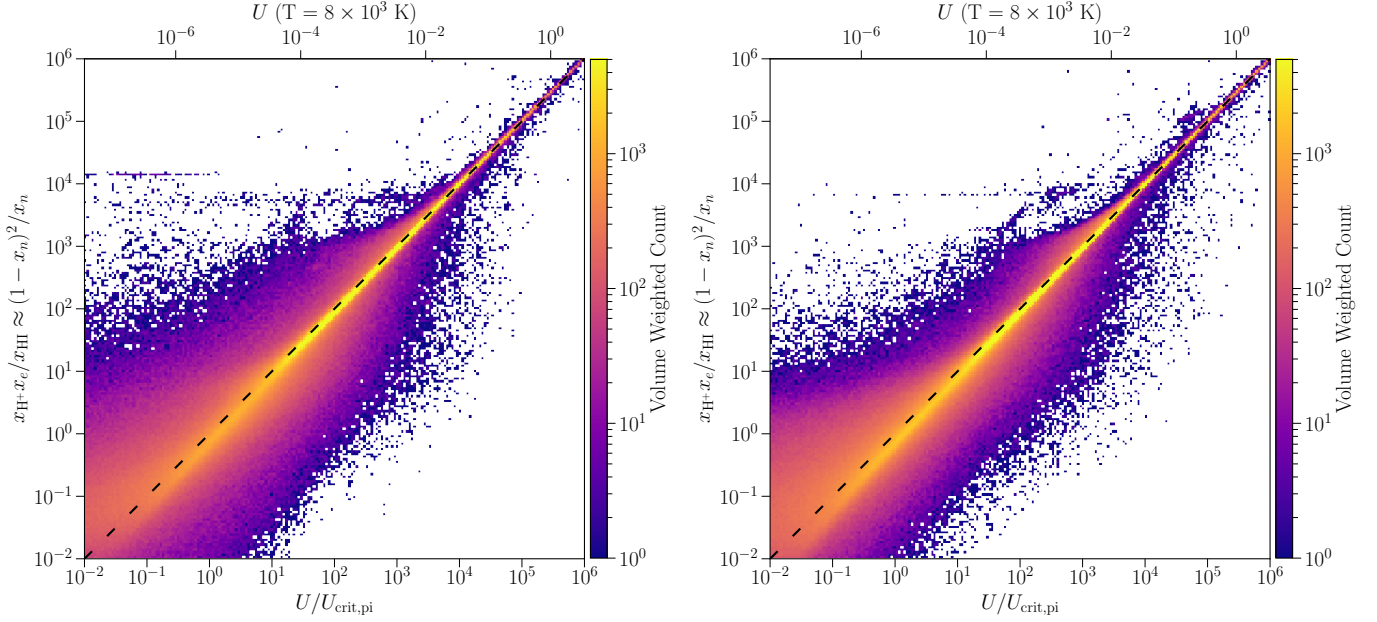


Figure 20. Distribution from R8-4pc (left) and LGR4-2pc (right) of volume as functions of $U/U_{\text{crit,pi}}$ and $x_{\text{H}}+x_{\text{e}}/x_{\text{HI}}$ (Equation 23). This includes all warm gas (between 6×10^3 and 3.5×10^4 K) with non-zero \mathcal{E}_{LyC} and within $|z| < 4$ pc or $|z| < 2$ pc respectively. $U_{\text{crit,pi}}$ is defined in Equation 24. The black dashed line represents photoionization equilibrium (see Equation 23); most locations with $x_{\text{H}}+x_{\text{e}}/x_{\text{HI}} > 10$ ($x_{\text{n}} \lesssim 0.1$) are consistent with this. Top axes indicate the ionization parameter U for $T = 8000$ K.

gas, n_{H} , to vary approximately linearly with Σ_{SFR} when comparing different galactic environments. Additionally, we would expect a roughly linear dependence of \mathcal{E}_{LyC} on Σ_{SFR} . This argues that the mean value of $U \propto \mathcal{E}_{\text{LyC}}/n_{\text{H}}$ (Equation 21) would be independent of galactic environment. Figure 22 confirms that the peak of the distributions, based on all snapshots, is at $U \approx 2 \times 10^{-3}$ in both the R8-4pc and LGR4-2pc models. We can understand the typical value of U in R8-4pc based on the photon rate per unit area, $\Phi_{\text{LyC}} \sim 4 \times 10^{50} \text{ s}^{-1} \text{ kpc}^{-2}$ from Table 3, and the typical density in the warm gas at the midplane, $\bar{n}_{\text{H}} \sim 0.4$. With l_*^{-2} the number of sources per unit area, we can estimate the mean photon rate per source to be $L_*/(h\nu) = \Phi_{\text{LyC}} l_*^2$. If the nearest source is at a distance of $\sim l_*/2$, the photon flux is roughly $F = L_*/(4\pi(l_*/2)^2) = \Phi_{\text{LyC}}/\pi$. Therefore, the photon number density is $n_{\text{ph}} = F/c \approx \Phi_{\text{LyC}}/(\pi c)$. We can then estimate $U = n_{\text{ph}}/n_{\text{H}} \sim \Phi_{\text{LyC}}/(\pi c n_{\text{H}}) \sim 10^{-3}$. A similar calculation in LGR4-2pc would lead to the prediction $U \sim \Phi_{\text{LyC}}/(\pi c n_{\text{H}}) \sim 3 \times 10^{-3}$.

Along any given line of sight, the total optical depth in the LyC band can be written as

$$\begin{aligned} \tau_{\text{LyC}} &= \int n_{\text{H}} (\sigma_{\text{d}} + x_{\text{n}} \sigma_{\text{pi}}) ds \\ &= \sigma_{\text{pi}} \int n_{\text{H}} \frac{U_{\text{crit,pi}}}{U} \left(\frac{U}{U_{\text{crit,d}}} + 1 \right) ds. \end{aligned} \quad (26)$$

In the second line we assume that ionization equilibrium holds with $U/U_{\text{crit,pi}} > 1$ so $x_{\text{e}} \approx 1$. Equation 26 shows that provided that $U/U_{\text{crit,d}} < 1$, the dust absorption term may be neglected, i.e. $\tau_{\text{LyC}} \approx \sigma_{\text{pi}} \int n_{\text{H}} x_{\text{n}} ds$. Equation 26 also allows us to write the mean free path for LyC photons within photoionized gas as

$$\begin{aligned} \ell_{\text{LyC}} &= \frac{1}{\sigma_{\text{pi}} \langle n_{\text{H}} U_{\text{crit,pi}}/U \rangle} = \frac{c/\alpha_{\text{B}}}{\langle n_{\text{H}}/U \rangle} \\ &\sim 100 \text{ pc} \left\langle \left(\frac{n_{\text{H}}}{0.5 \text{ cm}^{-3}} \right) \left(\frac{2 \times 10^{-3}}{U} \right) \right\rangle^{-1}, \end{aligned} \quad (27)$$

where the angle brackets indicate a volume-weighted average, and in the second line we have normalized n_{H} and U to typical diffuse ISM values for solar neighborhood conditions. This shows that within diffuse ionized gas (DIG), LyC photons are expected to be able to traverse distances approaching the disk scale height – while still not photoionizing the whole ISM, which would require larger U . At large $|z|$, the density drops and the ionization parameter remains roughly constant which would lead to an increase in the mean free path. Given that a significant volume fraction in the ISM is occupied by hot gas with which the LyC photons do not interact, we can understand how LyC radiation escapes from near the disk midplane and is able to maintain an extended photoionized layer at high altitude (see also Kado-Fong et al. 2020).

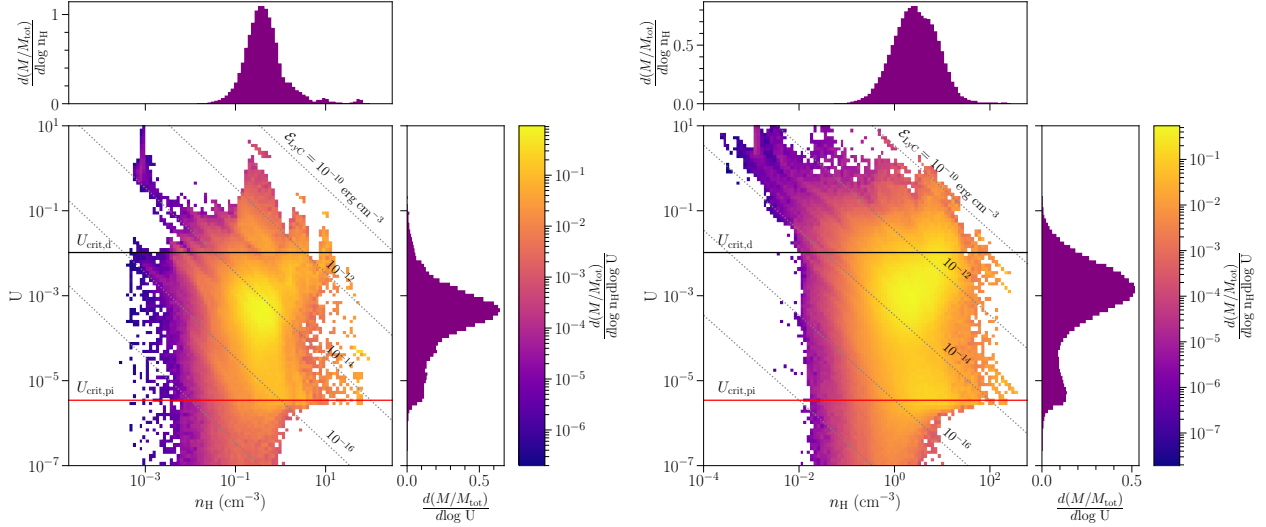


Figure 21. The mass weighted distribution of ionization parameter U and gas density n_{H} for all WIM at $|z| < 300$ pc. The left panel shows the R8-4pc simulation at $t = 430$ Myr. The right panel shows the LGR4-2pc at $t = 298$ Myr. The top and side panels show the projection of this distribution into distributions of U and n_{H} alone. Dotted diagonal lines show the corresponding value of the LyC energy density at each gas density under the assumption of ionization equilibrium (Equation 22). Below $U_{\text{crit},d}$, absorption by neutral hydrogen exceeds dust absorption (see Equation 25). The black and red horizontal lines show the critical ionization parameters for $\alpha_{\text{B}} = 3 \times 10^{-13} \text{ cm}^3 \text{ s}^{-1}$ (Equation 24 and Equation 25).

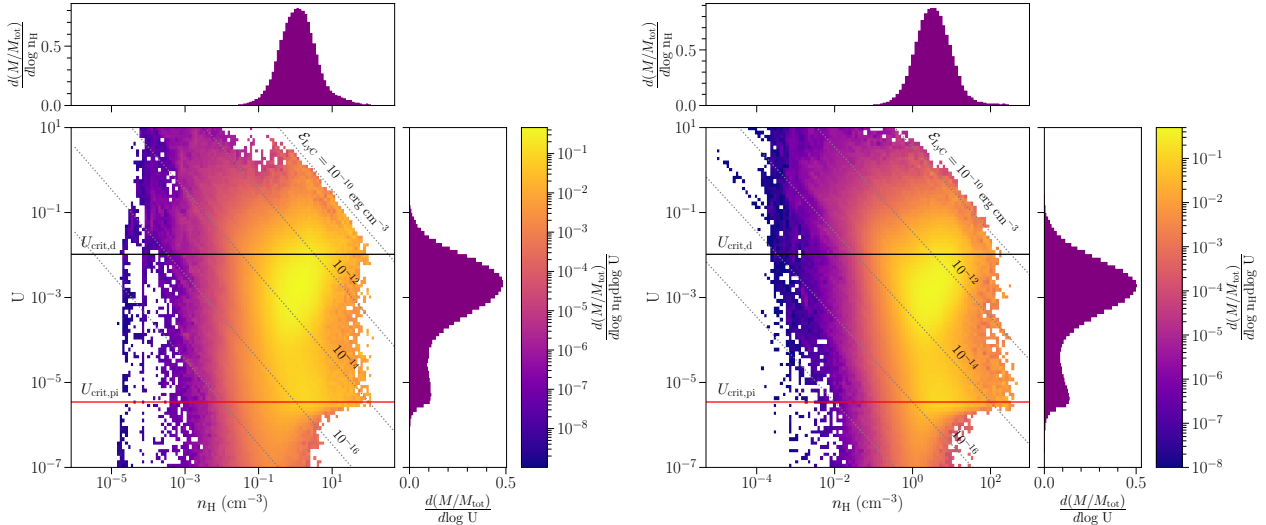


Figure 22. The same as Figure 21 but for midplane WIM across all snapshots. The left panel shows the R8-4pc simulation for $t = 250$ –450 Myr. The right panel shows the LGR4-2pc simulation for $t = 250$ –350 Myr. The gas is limited to that within $|z| < 4$ pc or $|z| < 2$ pc respectively.

5.2. LyC Sum of Sources Model

In this section, we compare a simple model to the solution of the ray-tracing for the LyC radiation. The model we explore is similar to that described in Section 4.2.4 for FUV radiation, and also to the model presented in Belfiore et al. (2022) with some modifications. As in these models, we estimate the LyC radiation field at each point by summing the contribution from each of the source particles. For the LyC radiation, we must

include the absorption by both neutral hydrogen and dust. The angle-averaged estimated radiation field at each point is then described by

$$J_{\text{LyC,src}} = \frac{1}{4\pi} \sum_{\text{sources } i} \frac{L_i}{4\pi r_i^2} e^{-r_i \langle n_{\text{H}} \rangle (\sigma_{\text{pi}} x_{\text{n,eff}} + \sigma_{\text{d}})}. \quad (28)$$

In this expression, L_i is the LyC luminosity of source i and r_i is the distance from the source to a given point. As in Section 4.2.4, we sum over sources in a horizontally

extended domain with positions determined by shearing-periodic boundary conditions. In the exponent, the average density is set equal to total mean hydrogen number density within one scale height of the midplane for each snapshot. Attenuation comes from both dust, represented with the cross section σ_d , and photoionization, represented by the product of the cross section σ_{pi} and the effective neutral fraction, $x_{\text{n,eff}}$, since only neutral hydrogen absorbs photons. All values in this expression are taken directly from the simulation outputs except for $x_{\text{n,eff}}$, which is left as a free parameter. This can be used to fit the model to the simulation.

After calculating $J_{\text{LyC,src}}$ at each point with Equation 28, we want to use this to create an observable; since LyC produces ionized gas, the most natural observable is the emission measure, most commonly obtained from H α . In terms of the electron and proton number density, the emission measure is calculated as

$$\text{EM} = \int_{-H}^H n_e n_{\text{H}^+} dz. \quad (29)$$

This expression can be used to calculate EM directly from the simulation, in which both n_e and n_{H^+} are known at each point based on the ray-tracing and (time-dependent) photochemistry. For the model, we treat $n_e n_{\text{H}^+}$ as unknown. We rewrite Equation 29 under the assumption that the gas is in ionization equilibrium, which from Equation 22 yields

$$\text{EM} = \frac{4\pi\sigma_{\text{pi}}}{\alpha_B h\nu_{\text{LyC}}} \int_{-H}^H n_{\text{H}} x_{\text{n,eff}} J_{\text{LyC}} dz. \quad (30)$$

In Equation 30, we use the constant value $\langle n_{\text{H}} \rangle$ for n_{H} ; $x_{\text{n,eff}}$ is also treated as a constant (this is the fitting parameter of the model), and we use Equation 28 for J_{LyC} . The value of α_B is for $T = 8000$ K. We restrict our model to within one scale height of the midplane.

For any given simulation snapshot, for both the simulation and the model, we find EM at each (x, y) coordinate using Equation 29 and Equation 30 respectively. We find the distributions of EM across all cells, then compare the model and simulation distributions $f(\text{EM})$ for different values of the fitting parameter $x_{\text{n,eff}}$. To compare the model and data, we define an error function

$$\text{error} = \sqrt{\frac{\sum_i (f_{\text{model}}(\text{EM}_i) - f_{\text{sim}}(\text{EM}_i))^2 \text{EM}_i}{\sum_i \text{EM}_i}} \quad (31)$$

where the sum is over bins of EM in log space.

We omit points within a projected distance of 50 pc from each source, as an approximate approach to masking out classical H II regions. We compare the distributions of EM rather than comparing cell by cell so that

differences in regions with very low EM do not dominate. Our method weights the error towards high EM so that the model fits the brightest regions best. By varying $x_{\text{n,eff}}$ we can then find the model which best fits the simulation.

The model in Belfiore et al. (2022) is similar to ours, except that rather than $\langle n_{\text{H}} \rangle (\sigma_{\text{pi}} x_{\text{n,eff}} + \sigma_d)$ in the exponent of Equation 28, they assume a single galaxy-wide constant k_0 (which has units 1/distance), and in computing the EM they adopt an overall scaling factor for the product of the disk thickness and the ratio $f_{\text{esc}}/(1 - f_{\text{esc}})$, which is normalized from the data; this f_{esc} represents the escape fraction from H II regions. They use their model to compute a predicted H α emission per unit area, which is proportional to EM (they note that their model does not correct for extinction in the diffuse gas). The overall best-fit value of k_0 is obtained by taking a ratio of model H α to data H α (which does not correct for extinction), after masking the H II regions. While they present the ratio of model to data as a function of H α emission, they do not weight by emission in selecting the best-fit value of k_0 .

The comparison of the simulated EM to the best fit model for one snapshot from R8-4pc is shown in Figure 23. The first panel (a) represents the map of EM determined from the simulated values of n_e and n_{H^+} . The second panel (b) represents the modeled EM with the best fit value of $x_{\text{n,eff}} = 0.004$, which minimizes the error for this snapshot (see Figure 24). In the modeled EM, contributions from individual sources are spherically symmetric, unlike in the simulated EM where complex structures are visible. For example, the large-scale moderate-brightness regions that appear in panel (a) are generally associated with photoionized gas on the inner surfaces of hot bubbles; these hot bubbles can be seen in the midplane slices of Figure 3.

In Figure 23, we also include comparisons using values of $x_{\text{n,eff}}$ obtained in alternate ways. One method to find $x_{\text{n,eff}}$ is by using the ionization parameter, U , through Equation 23. As $x_{\text{n,eff}}$ is small, we find $x_{\text{n,eff}} \approx U_{\text{crit,pi}}/U$. The motivation for this approach is that U can be obtained in observations from line ratios. For a given snapshot, we find the distribution of ionization parameter including only the WIM (as in Figure 21). We take the mass weighted median value of U and use this to calculate $x_{\text{n,eff}}$. This value can be applied in Equation 28 as before to obtain $J_{\text{LyC,src}}$, and then the distribution of $J_{\text{LyC,src}}$ is used to compute the EM map from Equation 30. For the snapshot shown, the median $U = 4 \times 10^{-4}$ (from the distribution shown in Figure 22) corresponds to $x_{\text{n,eff}} = 0.009$, similar to the value we obtained through fitting the model to the data. The model

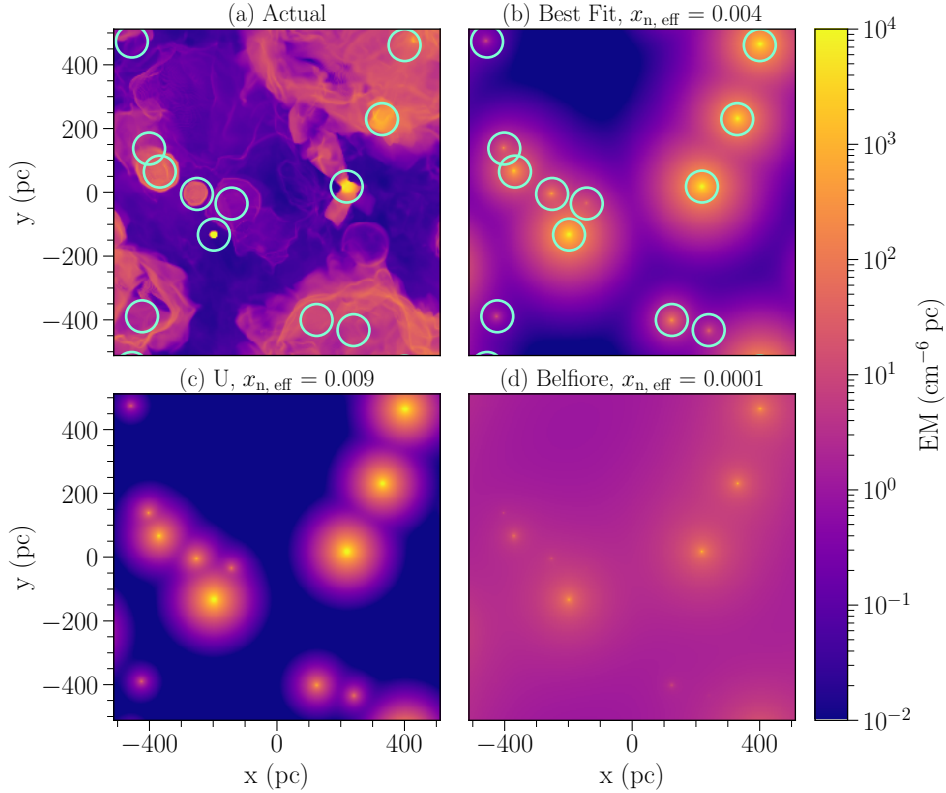


Figure 23. Projection on the disk midplane of the EM from the simulation at $t = 430$ Myr, panel (a), in comparison to model EM determined from the attenuated ionizing multi-source model, using different values of $x_{n,\text{eff}}$ in Equation 28 and Equation 30. In panel (b), we show the best fit value based on minimizing the difference in EM as illustrated in Figure 24 ($x_{n,\text{eff}} = 0.004$). In the first two panels, we include blue circles representing the regions around each source which are masked for the fit. The value based on the peak of the emission pdf in U and n_{H} in Figure 21 ($x_{n,\text{eff}} = 0.009$) is shown in panel (c). A value consistent with a similar modeling approach reported in Belfiore et al. (2022) ($x_{n,\text{eff}} = 0.0001$) is shown in panel (d).

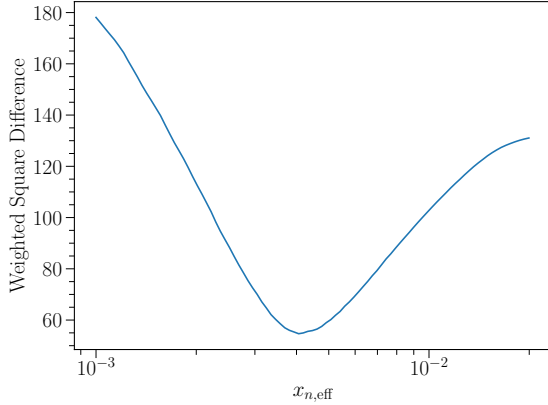


Figure 24. Weighted square difference (Equation 31), summed over the map, between the simulation value of EM and the EM calculated with the attenuated ionizing multi-source model, for different values of the parameter x_n in Equation 28 and Equation 30. The snapshot is at $t = 430$ Myr. This allows us to identify the best-fit value as $x_{n,\text{eff}} = 0.004$. See text in Section 5.2 for model details.

using the value of $x_{n,\text{eff}}$ derived from the ionization parameter is shown in the third panel (c) of Figure 23.

Finally, we include an EM map using the results from Belfiore et al. (2022). They found a typical $k_0 = 0.52 \text{ kpc}^{-1}$ (i.e. mean free path of 1.9 kpc), which for our mean density of $\langle n_{\text{H}} \rangle = 0.6 \text{ cm}^{-3}$ in the snapshot shown translates to $x_{n,\text{eff}} = 0.52 \text{ kpc}^{-1} / (\langle n_{\text{H}} \rangle \sigma_{\text{pi}}) \approx 0.0001$. The EM map using this value of $x_{n,\text{eff}}$ is shown in panel (d) of Figure 23. Because the constant in the attenuation law is nearly two orders of magnitude lower than our best fit or the U -derived map, the appearance is very different. There is significantly more diffuse emission because attenuation by neutral hydrogen is underestimated.

Although the values of $x_{n,\text{eff}}$ from both the best fit of the model and as determined with U are similar, they do not completely agree. We repeat this process for many simulation snapshots of the R8-8pc model to find the distribution of $x_{n,\text{eff}}$. We find that the two methods do not give values of $x_{n,\text{eff}}$ that are well correlated, but both fall in a limited range. The fitted value is in the range $x_{n,\text{eff}} = 10^{-3} - 10^{-2}$ for almost all snapshots, as shown in

the left panel of Figure 25. Most values derived from U are in the same range, although some are as large as $\sim 10^{-1}$. These snapshots tend to have low values of Φ_{LyC} and very little WIM gas. The corresponding mean free path for ionizing radiation is $\ell_{\text{LyC}} = (\sigma_{\text{pi}} \langle n_{\text{H}} \rangle x_{\text{n,eff}})^{-1}$, which we show in the lower panel of Figure 25. The mean free path from our fits is $\ell_{\text{LyC}} \sim 20 - 300$ pc.

As a comparison, we apply this model to the LGR4-2pc model at $t = 298$ Myr. We cannot mask 50 pc around each source in this case because the majority of the area is removed. Without the mask, we find $x_{\text{n,eff}} = 0.002$. This is of the same magnitude as the value of $x_{\text{n,eff}}$ from the R8-4pc model. The estimated value of $x_{\text{n,eff}}$ from the ionization parameter, U , is also similar between the two models. For the LGR4-2pc snapshot we find $x_{\text{n,eff}} = 0.003$. We expect the ionization parameter to be relatively insensitive to galactic environmental conditions, as discussed in Section 5.1, and therefore the value of $x_{\text{n,eff}}$ estimated from U would be similar between the two models.

We note that the smaller attenuation constant (or larger mean free path) obtained by Belfiore et al. (2022) would correspond to an order of magnitude higher ionization parameter than we typically find in the R8-4pc model. One possibility is that the parameter regime for their sample of galaxies is simply somewhat different from what we are exploring in our simulations. However, as noted above, we expect similar values of U and $x_{\text{n,eff}}$ in different environments. For a given $x_{\text{n,eff}}$, we would expect shorter, rather than longer mean free path for LyC photons in environments at higher density, which may be more similar to those explored by Belfiore et al. (2022). Another alternative is that the details of our respective fitting methods are responsible for the differences in our conclusions. In particular, it is interesting that when Belfiore et al. (2022) set $k_0 = 10 \text{ kpc}^{-1}$ (similar to our best-fit value for $\langle n_{\text{H}} \rangle \sigma_{\text{pi}} x_{\text{n,eff}}$), their Fig. 6 shows the model is quite close to the data relatively near spiral arms where H II regions are concentrated, with a departure only in very low density regions. For their preferred value, $k_0 \sim 1 \text{ kpc}^{-1}$, the model exceeds the data relatively near to spiral arms, indicating that radiation is insufficiently attenuated. It is possible that if their fit had given more weight to the regions with higher EM, as we do, they would have obtained more similar results to ours.

6. SUMMARY

In this work, we analyze characteristics of the FUV and LyC radiation fields in TIGRESS-NCR simulations with ray tracing and explore applications of our results to observations and other theoretical modeling. We fo-

cus on one model with conditions similar to the solar neighborhood and another similar to the inner galaxy.

Key results are as follows:

- The time-averaged midplane FUV radiation intensity for our solar neighborhood model is very similar to observational estimates for the local Milky Way. For both the solar neighborhood and inner galaxy models, the FUV intensity decreases exponentially with distance from the midplane.
- The statistical distribution of the FUV intensity is well characterized by a model similar to that presented in Draine & Li (2007). This combines a strong power law component near sources with a diffuse component, which we find is well fit by a lognormal. We fit expressions for the local FUV attenuation that depend just on density.
- We introduce a normalized FUV radiation intensity, \mathcal{J} , by factoring out the total FUV luminosity per unit area per unit solid angle from all radiation sources in the disk and compare simulation values to three approximate models for \mathcal{J} . We find the plane parallel approximation follows the simulated values closely, and therefore represents an attractive approach in simulations when full ray tracing is infeasible but an accurate radiation field is required to compute the photoelectric heating rate. The other two approximations are within 50% of the simulation value, and are useful for simple estimates of the radiation field.
- We convolve the FUV radiation with density to make synthetic maps of dust heating in external galaxies. To the extent that the dust abundance and emissivity are spatially uniform, these heating maps are a proxy for IR dust emission. We demonstrate that given the spatial distribution and luminosities of star clusters, it is straightforward to correct for nonuniform heating to obtain an estimator of the gas column, $N_{\text{H,est}}$. The estimator is linear in N_{H} up to columns exceeding 10^{22} cm^{-2} , and has small scatter. This approach has potential applications in calibrating PAH emission observations to obtain high resolution maps of gas surface density.
- For both of our simulations, the majority of warm ionized gas is diffuse, with densities $< 1 \text{ cm}^{-3}$. We show that ionization-recombination equilibrium is satisfied for gas in the midplane that is exposed to LyC radiation and has $x_{\text{n}} < 0.1$. The ionization parameter has a typical value $U \sim 10^{-3}$ in both

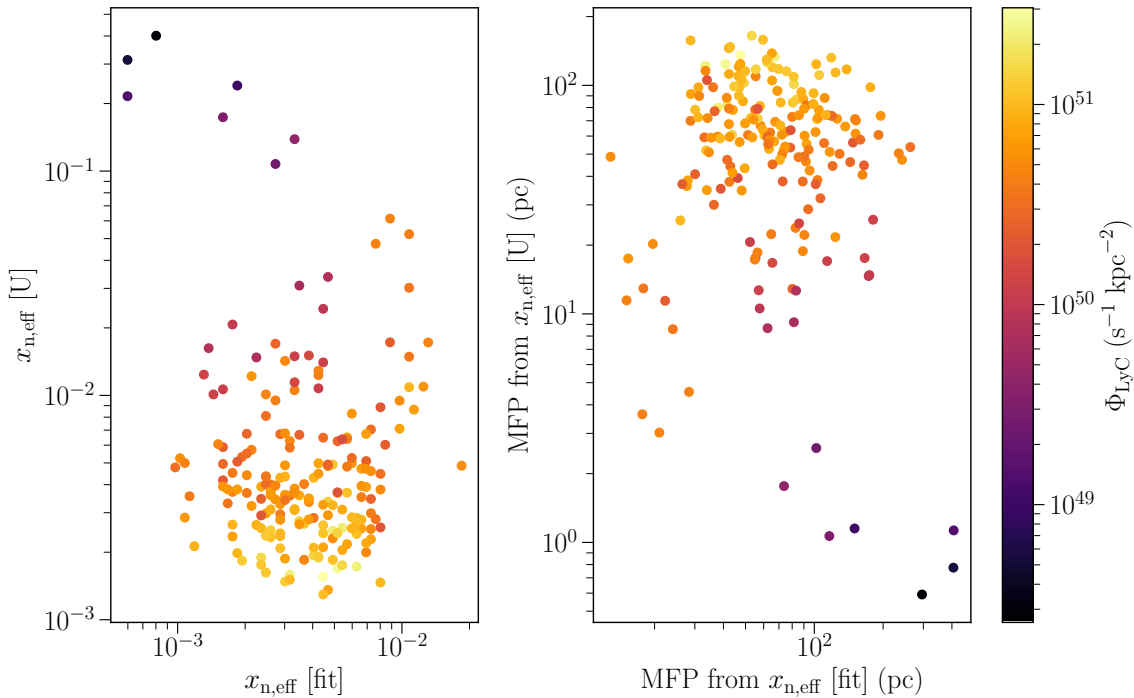


Figure 25. For 200 different snapshots of model R8–8pc, the *left panel* shows a comparison of $x_{n,\text{eff}}$ from minimizing the difference between EM from the simulation and EM calculated via the attenuated ionizing multi-source model ($x_{n,\text{eff}}$ [fit]; see Section 5.2), and the most likely value of $x_{n,\text{eff}}$ based on the ionization parameter and density distribution ($x_{n,\text{eff}}$ [U]; see Section 5.1). The *right panel* shows the corresponding mean free path of ionizing photons $\ell_{\text{LyC}} = (\langle n_{\text{H}} \rangle \sigma_{\text{pi}} x_{\text{n}})^{-1}$ for each value of $x_{n,\text{eff}}$ [fit] or $x_{n,\text{eff}}$ [U].

simulations. This result is consistent with the theoretical expectation that U in diffuse gas will be independent of galactic environment.

- We model the LyC radiation field using a sum of sources model accounting for attenuation by neutral gas and dust similar to that in Belfiore et al. (2022), using this model to create EM maps. While these maps do not reproduce the full structure of the EM from our ray-tracing simulations, the fitted value of the neutral fraction, $x_{n,\text{eff}}$, is comparable to the true value within the diffuse ionized gas. The corresponding value of the effective mean free path for ionizing photons is of order 100 pc.

Beyond the many interesting individual results from the two simulations we have analyzed here, our presentation bears witness to the value of implementing accurate and efficient radiative transfer methods in numerical simulations of the multiphase ISM. The TIGRESS-NCR framework with ART has now been applied to a much wider range of galactic conditions, including en-

vironments with far lower metallicity (Kim et al. 2024). These new simulations will provide a diverse testbed in which to investigate connections between the radiation field and the physical state and observational diagnostics of interstellar material.

ACKNOWLEDGMENTS

This work was supported in part by grant 510940 from the Simons Foundation to E. C. Ostriker. The work of C.-G.K. was supported in part by NASA ATP grant No. 80NSSC22K0717. J.-G.K. acknowledges support from the EACOA Fellowship awarded by the East Asia Core Observatories Association. Computational resources were provided by the Princeton Institute for Computational Science and Engineering (PICSciE) and the Office of Information Technology’s High Performance Computing Center at Princeton University.

Software: Athena (Stone et al. 2008; Stone & Gardiner 2009), Matplotlib (Hunter 2007), NumPy (Harris et al. 2020), SciPy (Virtanen et al. 2020), Astropy (Astropy Collaboration et al. 2013, 2018, 2022), xarray (Hoyer & Hamman 2017), pandas (McKinney 2010)

REFERENCES

- Abel, T., & Wandelt, B. D. 2002, *MNRAS*, 330, L53, doi: [10.1046/j.1365-8711.2002.05206.x](https://doi.org/10.1046/j.1365-8711.2002.05206.x)
- Adamo, A., Ryon, J. E., Messa, M., et al. 2017, *ApJ*, 841, 131, doi: [10.3847/1538-4357/aa7132](https://doi.org/10.3847/1538-4357/aa7132)
- Astropy Collaboration, Robitaille, T. P., Tollerud, E. J., et al. 2013, *A&A*, 558, A33, doi: [10.1051/0004-6361/201322068](https://doi.org/10.1051/0004-6361/201322068)
- Astropy Collaboration, Price-Whelan, A. M., Sipőcz, B. M., et al. 2018, *AJ*, 156, 123, doi: [10.3847/1538-3881/aabc4f](https://doi.org/10.3847/1538-3881/aabc4f)
- Astropy Collaboration, Price-Whelan, A. M., Lim, P. L., et al. 2022, *ApJ*, 935, 167, doi: [10.3847/1538-4357/ac7c74](https://doi.org/10.3847/1538-4357/ac7c74)
- Bakes, E. L. O., & Tielens, A. G. G. M. 1994, *ApJ*, 427, 822, doi: [10.1086/174188](https://doi.org/10.1086/174188)
- Belfiore, F., Santoro, F., Groves, B., et al. 2022, *A&A*, 659, A26, doi: [10.1051/0004-6361/202141859](https://doi.org/10.1051/0004-6361/202141859)
- Bialy, S. 2020, *ApJ*, 903, 62, doi: [10.3847/1538-4357/abb804](https://doi.org/10.3847/1538-4357/abb804)
- Bocchio, M., Micelotta, E. R., Gautier, A. L., & Jones, A. P. 2012, *A&A*, 545, A124, doi: [10.1051/0004-6361/201219705](https://doi.org/10.1051/0004-6361/201219705)
- Chastenet, J., Sandstrom, K., Chiang, I.-D., et al. 2019, *ApJ*, 876, 62, doi: [10.3847/1538-4357/ab16cf](https://doi.org/10.3847/1538-4357/ab16cf)
- Chevance, M., Krumholz, M. R., McLeod, A. F., et al. 2023, in *Astronomical Society of the Pacific Conference Series*, Vol. 534, *Protostars and Planets VII*, ed. S. Inutsuka, Y. Aikawa, T. Muto, K. Tomida, & M. Tamura, 1
- Draine, B. T. 1978a, *ApJS*, 36, 595, doi: [10.1086/190513](https://doi.org/10.1086/190513)
- . 1978b, *ApJS*, 36, 595, doi: [10.1086/190513](https://doi.org/10.1086/190513)
- Draine, B. T., & Bertoldi, F. 1996, *ApJ*, 468, 269, doi: [10.1086/177689](https://doi.org/10.1086/177689)
- Draine, B. T., & Li, A. 2007, *ApJ*, 657, 810, doi: [10.1086/511055](https://doi.org/10.1086/511055)
- Draine, B. T., Dale, D. A., Bendo, G., et al. 2007, *ApJ*, 663, 866, doi: [10.1086/518306](https://doi.org/10.1086/518306)
- Egorov, O. V., Kreckel, K., Sandstrom, K. M., et al. 2023, *ApJL*, 944, L16, doi: [10.3847/2041-8213/acac92](https://doi.org/10.3847/2041-8213/acac92)
- Fuchs, B., Jahreiß, H., & Flynn, C. 2009, *AJ*, 137, 266, doi: [10.1088/0004-6256/137/1/266](https://doi.org/10.1088/0004-6256/137/1/266)
- Fukushima, H., & Yajima, H. 2021, *MNRAS*, 506, 5512, doi: [10.1093/mnras/stab2099](https://doi.org/10.1093/mnras/stab2099)
- Gong, M., Ostriker, E. C., & Wolfire, M. G. 2017, *ApJ*, 843, 38, doi: [10.3847/1538-4357/aa7561](https://doi.org/10.3847/1538-4357/aa7561)
- Górski, K. M., Hivon, E., Banday, A. J., et al. 2005, *ApJ*, 622, 759, doi: [10.1086/427976](https://doi.org/10.1086/427976)
- Grudić, M. Y., Guszejnov, D., Offner, S. S. R., et al. 2022, *MNRAS*, 512, 216, doi: [10.1093/mnras/stac526](https://doi.org/10.1093/mnras/stac526)
- Harries, T. J., Haworth, T. J., Acreman, D., Ali, A., & Douglas, T. 2019, *Astronomy and Computing*, 27, 63, doi: [10.1016/j.ascom.2019.03.002](https://doi.org/10.1016/j.ascom.2019.03.002)
- Harris, C. R., Millman, K. J., van der Walt, S. J., et al. 2020, *Nature*, 585, 357, doi: [10.1038/s41586-020-2649-2](https://doi.org/10.1038/s41586-020-2649-2)
- Hassani, H., Rosolowsky, E., Koch, E. W., et al. 2024, *ApJS*, 271, 2, doi: [10.3847/1538-4365/ad152c](https://doi.org/10.3847/1538-4365/ad152c)
- Hensley, B. S., & Draine, B. T. 2023, *ApJ*, 948, 55, doi: [10.3847/1538-4357/acc4c2](https://doi.org/10.3847/1538-4357/acc4c2)
- Herrera-Camus, R., Bolatto, A., Wolfire, M., et al. 2017, *ApJ*, 835, 201, doi: [10.3847/1538-4357/835/2/201](https://doi.org/10.3847/1538-4357/835/2/201)
- Hoang, T., Tram, L. N., Lee, H., & Ahn, S.-H. 2019, *Nature Astronomy*, 3, 766, doi: [10.1038/s41550-019-0763-6](https://doi.org/10.1038/s41550-019-0763-6)
- Hoyer, S., & Hamman, J. 2017, *Journal of Open Research Software*, 5, doi: [10.5334/jors.148](https://doi.org/10.5334/jors.148)
- Hunter, J. D. 2007, *Computing in Science & Engineering*, 9, 90, doi: [10.1109/MCSE.2007.55](https://doi.org/10.1109/MCSE.2007.55)
- Jiang, Y.-F., Stone, J. M., & Davis, S. W. 2012, *ApJS*, 199, 14, doi: [10.1088/0067-0049/199/1/14](https://doi.org/10.1088/0067-0049/199/1/14)
- Kado-Fong, E., Kim, J.-G., Ostriker, E. C., & Kim, C.-G. 2020, *ApJ*, 897, 143, doi: [10.3847/1538-4357/ab9abd](https://doi.org/10.3847/1538-4357/ab9abd)
- Kannan, R., Vogelsberger, M., Marinacci, F., et al. 2019, *MNRAS*, 485, 117, doi: [10.1093/mnras/stz287](https://doi.org/10.1093/mnras/stz287)
- Kennicutt, R. C., & Evans, N. J. 2012, *ARA&A*, 50, 531, doi: [10.1146/annurev-astro-081811-125610](https://doi.org/10.1146/annurev-astro-081811-125610)
- Kim, C.-G., Kim, J.-G., Gong, M., & Ostriker, E. C. 2023a, *ApJ*, 946, 3, doi: [10.3847/1538-4357/acbd3a](https://doi.org/10.3847/1538-4357/acbd3a)
- Kim, C.-G., & Ostriker, E. C. 2017, *ApJ*, 846, 133, doi: [10.3847/1538-4357/aa8599](https://doi.org/10.3847/1538-4357/aa8599)
- Kim, C.-G., Ostriker, E. C., Somerville, R. S., et al. 2020, *ApJ*, 900, 61, doi: [10.3847/1538-4357/aba962](https://doi.org/10.3847/1538-4357/aba962)
- Kim, C.-G., Ostriker, E. C., Kim, J.-G., et al. 2024, *arXiv e-prints*, arXiv:2405.19227, <https://arxiv.org/abs/2405.19227>
- Kim, J.-G., Gong, M., Kim, C.-G., & Ostriker, E. C. 2023b, *ApJS*, 264, 10, doi: [10.3847/1538-4365/ac9b1d](https://doi.org/10.3847/1538-4365/ac9b1d)
- Kim, J.-G., Kim, W.-T., & Ostriker, E. C. 2016, *ApJ*, 819, 137, doi: [10.3847/0004-637X/819/2/137](https://doi.org/10.3847/0004-637X/819/2/137)
- . 2018, *ApJ*, 859, 68, doi: [10.3847/1538-4357/aabe27](https://doi.org/10.3847/1538-4357/aabe27)
- . 2019, *ApJ*, 883, 102, doi: [10.3847/1538-4357/ab3d3d](https://doi.org/10.3847/1538-4357/ab3d3d)
- Kim, J.-G., Kim, W.-T., Ostriker, E. C., & Skinner, M. A. 2017, *ApJ*, 851, 93, doi: [10.3847/1538-4357/aa9b80](https://doi.org/10.3847/1538-4357/aa9b80)
- Kim, J.-G., Ostriker, E. C., & Filippova, N. 2021, *ApJ*, 911, 128, doi: [10.3847/1538-4357/abe934](https://doi.org/10.3847/1538-4357/abe934)
- Klepitko, A., Walch, S., Wunsch, R., et al. 2023, *Monthly Notices of the Royal Astronomical Society*, 521, 160
- Krumholz, M. R., & Matzner, C. D. 2009, *ApJ*, 703, 1352, doi: [10.1088/0004-637X/703/2/1352](https://doi.org/10.1088/0004-637X/703/2/1352)
- Krumholz, M. R., McKee, C. F., & Bland-Hawthorn, J. 2019, *ARA&A*, 57, 227, doi: [10.1146/annurev-astro-091918-104430](https://doi.org/10.1146/annurev-astro-091918-104430)

- Lee, J. C., Whitmore, B. C., Thilker, D. A., et al. 2022, *ApJS*, 258, 10, doi: [10.3847/1538-4365/ac1fe5](https://doi.org/10.3847/1538-4365/ac1fe5)
- Leitherer, C., Ekström, S., Meynet, G., et al. 2014, *ApJS*, 212, 14, doi: [10.1088/0067-0049/212/1/14](https://doi.org/10.1088/0067-0049/212/1/14)
- Leitherer, C., Schaerer, D., Goldader, J. D., et al. 1999, *ApJS*, 123, 3, doi: [10.1086/313233](https://doi.org/10.1086/313233)
- Lenz, D., Hensley, B. S., & Doré, O. 2017, *ApJ*, 846, 38, doi: [10.3847/1538-4357/aa84af](https://doi.org/10.3847/1538-4357/aa84af)
- Leroy, A. K., Sandstrom, K. M., Lang, D., et al. 2019, *ApJS*, 244, 24, doi: [10.3847/1538-4365/ab3925](https://doi.org/10.3847/1538-4365/ab3925)
- Leroy, A. K., Sandstrom, K., Rosolowsky, E., et al. 2023, *ApJL*, 944, L9, doi: [10.3847/2041-8213/acaf85](https://doi.org/10.3847/2041-8213/acaf85)
- Li, A., & Draine, B. T. 2001, *ApJ*, 554, 778, doi: [10.1086/323147](https://doi.org/10.1086/323147)
- Mathis, J. S., Mezger, P. G., & Panagia, N. 1983, *A&A*, 128, 212
- McKee, C. F., & Williams, J. P. 1997, *ApJ*, 476, 144, doi: [10.1086/303587](https://doi.org/10.1086/303587)
- McKinney, W. 2010, in *Proceedings of the 9th Python in Science Conference*, ed. Stéfan van der Walt & Jarrod Millman, 56 – 61
- Melon Fuksman, J. D., & Mignone, A. 2019, *ApJS*, 242, 20, doi: [10.3847/1538-4365/ab18ff](https://doi.org/10.3847/1538-4365/ab18ff)
- Menon, S. H., Federrath, C., Krumholz, M. R., et al. 2022, *MNRAS*, 512, 401, doi: [10.1093/mnras/stac485](https://doi.org/10.1093/mnras/stac485)
- Menon, S. H., Lancaster, L., Burkhart, B., et al. 2024, *arXiv e-prints*, arXiv:2405.00813, doi: [10.48550/arXiv.2405.00813](https://doi.org/10.48550/arXiv.2405.00813)
- Micelotta, E. R., Jones, A. P., & Tielens, A. G. G. M. 2010, *A&A*, 510, A37, doi: [10.1051/0004-6361/200911683](https://doi.org/10.1051/0004-6361/200911683)
- Mor, R., Robin, A. C., Figueras, F., Roca-Fàbrega, S., & Luri, X. 2019, *A&A*, 624, L1, doi: [10.1051/0004-6361/201935105](https://doi.org/10.1051/0004-6361/201935105)
- Ostriker, E. C., & Kim, C.-G. 2022, *ApJ*, 936, 137, doi: [10.3847/1538-4357/ac7de2](https://doi.org/10.3847/1538-4357/ac7de2)
- Ostriker, E. C., McKee, C. F., & Leroy, A. K. 2010, *ApJ*, 721, 975, doi: [10.1088/0004-637X/721/2/975](https://doi.org/10.1088/0004-637X/721/2/975)
- Parravano, A., Hollenbach, D. J., & McKee, C. F. 2003, *ApJ*, 584, 797, doi: [10.1086/345807](https://doi.org/10.1086/345807)
- Pathak, D., Leroy, A. K., Thompson, T. A., et al. 2023, *The Astronomical Journal*, 167, 39
- Pathak, D., Leroy, A. K., Thompson, T. A., et al. 2024, *AJ*, 167, 39, doi: [10.3847/1538-3881/ad110d](https://doi.org/10.3847/1538-3881/ad110d)
- Rosdahl, J., Blaizot, J., Aubert, D., Stranex, T., & Teyssier, R. 2013, *MNRAS*, 436, 2188, doi: [10.1093/mnras/stt1722](https://doi.org/10.1093/mnras/stt1722)
- Rosdahl, J., & Teyssier, R. 2015, *MNRAS*, 449, 4380, doi: [10.1093/mnras/stv567](https://doi.org/10.1093/mnras/stv567)
- Rosen, A. L., Krumholz, M. R., Oishi, J. S., Lee, A. T., & Klein, R. I. 2017, *Journal of Computational Physics*, 330, 924
- Sales, L. V., Marinacci, F., Springel, V., & Petkova, M. 2014, *Monthly Notices of the Royal Astronomical Society*, 439, 2990
- Salim, S., Boquien, M., & Lee, J. C. 2018, *ApJ*, 859, 11, doi: [10.3847/1538-4357/aabf3c](https://doi.org/10.3847/1538-4357/aabf3c)
- Salim, S., Rich, R. M., Charlot, S., et al. 2007, *ApJS*, 173, 267, doi: [10.1086/519218](https://doi.org/10.1086/519218)
- Skinner, M. A., & Ostriker, E. C. 2013, *ApJS*, 206, 21, doi: [10.1088/0067-0049/206/2/21](https://doi.org/10.1088/0067-0049/206/2/21)
- Stone, J. M., & Gardiner, T. 2009, *NewA*, 14, 139, doi: [10.1016/j.newast.2008.06.003](https://doi.org/10.1016/j.newast.2008.06.003)
- Stone, J. M., Gardiner, T. A., Teuben, P., Hawley, J. F., & Simon, J. B. 2008, *ApJS*, 178, 137, doi: [10.1086/588755](https://doi.org/10.1086/588755)
- Sun, J., Leroy, A. K., Rosolowsky, E., et al. 2022, *AJ*, 164, 43, doi: [10.3847/1538-3881/ac74bd](https://doi.org/10.3847/1538-3881/ac74bd)
- Tielens, A. G. G. M. 2008, *ARA&A*, 46, 289, doi: [10.1146/annurev.astro.46.060407.145211](https://doi.org/10.1146/annurev.astro.46.060407.145211)
- van Dishoeck, E. F., & Black, J. H. 1982, *ApJ*, 258, 533, doi: [10.1086/160104](https://doi.org/10.1086/160104)
- Virtanen, P., Gommers, R., Oliphant, T. E., et al. 2020, *Nature Methods*, 17, 261, doi: [10.1038/s41592-019-0686-2](https://doi.org/10.1038/s41592-019-0686-2)
- Wadsley, J. W., Baumschlager, B., & Shen, S. 2024, *Monthly Notices of the Royal Astronomical Society*, 528, 3767
- Weingartner, J. C., & Draine, B. T. 2001a, *ApJ*, 548, 296, doi: [10.1086/318651](https://doi.org/10.1086/318651)
- . 2001b, *ApJ*, 563, 842, doi: [10.1086/324035](https://doi.org/10.1086/324035)
- Whitworth, A. 1979, *MNRAS*, 186, 59, doi: [10.1093/mnras/186.1.59](https://doi.org/10.1093/mnras/186.1.59)
- Wibking, B. D., & Krumholz, M. R. 2022, *MNRAS*, 512, 1430, doi: [10.1093/mnras/stac439](https://doi.org/10.1093/mnras/stac439)
- Wolfire, M. G., Hollenbach, D., McKee, C. F., Tielens, A. G. G. M., & Bakes, E. L. O. 1995, *ApJ*, 443, 152, doi: [10.1086/175510](https://doi.org/10.1086/175510)
- Wolfire, M. G., McKee, C. F., Hollenbach, D., & Tielens, A. G. G. M. 2003, *ApJ*, 587, 278, doi: [10.1086/368016](https://doi.org/10.1086/368016)
- Wünsch, R., Walch, S., Dinnbier, F., et al. 2021, *Monthly Notices of the Royal Astronomical Society*, 505, 3730
- Zari, E., Frankel, N., & Rix, H.-W. 2023, *A&A*, 669, A10, doi: [10.1051/0004-6361/202244194](https://doi.org/10.1051/0004-6361/202244194)

APPENDIX

A. APPROXIMATE FUV RADIATION MODELS

Ostriker et al. (2010) provided an expression for the angle-averaged radiation field at the midplane of a uniformly emitting slab with uniform FUV dust opacity κ , given by

$$J = \frac{\Sigma_{\text{FUV}}}{4\pi\tau_{\perp}} [1 - E_2(\tau_{\perp}/2)], \quad (\text{A1})$$

where Σ_{FUV} is the FUV luminosity per unit area from all sources, $\tau_{\perp} = \Sigma_{\text{slab}}\kappa$ is the FUV optical depth through the slab for Σ_{slab} its gas surface density, and E_2 is the second exponential integral. Note that in this appendix we streamline the notation from the main text, dropping ‘‘FUV’’ subscripts for all variables where there is no ambiguity. The expressions given here would also apply for any other continuum band (e.g. OPT, NUV) at frequency ν , with appropriate substitutions $\Sigma_{\text{FUV}} \rightarrow \Sigma_{\nu}$, $\kappa \rightarrow \kappa_{\nu}$, etc. (e.g., Appendix C of Kim et al. 2023b).

To derive Equation A1, first note that the emissivity per unit gas mass is $j = \Sigma_{\text{FUV}}/\Sigma_{\text{slab}}$, so that the source function is $S \equiv j/(4\pi\kappa) = \Sigma_{\text{FUV}}/(4\pi\tau_{\perp})$. In the direction $\theta = \arccos(\mu)$ with respect to vertical, the midplane intensity is

$$I(z=0; \mu) = \int_0^{\tau_{\perp}/(2\mu)} S e^{-\tau'} d\tau' = S[1 - e^{-\tau_{\perp}/(2\mu)}]. \quad (\text{A2})$$

The angle-averaged midplane intensity is then, considering the symmetry above and below the midplane,

$$\begin{aligned} J &= S \int_0^1 [1 - e^{-\tau_{\perp}/(2\mu)}] d\mu = S \left[1 - \int_1^{\infty} e^{-y\tau_{\perp}/2} y^{-2} dy \right] \\ &= S [1 - E_2(\tau_{\perp}/2)]; \end{aligned} \quad (\text{A3})$$

here we have changed variables to $y = 1/\mu$ and used the definition of E_2 . Substituting in for S , we obtain Equation A1. If we further divide by $\Sigma_{\text{FUV}}/(4\pi)$, we obtain the normalized midplane intensity $\mathcal{J}_{\text{slab,mid}}$ given by Equation 11 of the text.

For the vertically-averaged mean intensity, a similar calculation to Equation A2 gives

$$I(z; \mu) = S \begin{cases} 1 - e^{-\tau_{\perp}(1-z/H)/(2\mu)} & \mu > 0 \\ 1 - e^{\tau_{\perp}(1+z/H)/(2\mu)} & \mu < 0, \end{cases} \quad (\text{A4})$$

where $2H$ is the thickness of the slab. Averaging over z and over μ then leads to the expression for $\mathcal{J}_{\text{slab,avg}}$ given in Equation 13 of the text. In Figure 26 we show the comparison between $\mathcal{J}_{\text{slab,mid}}$ (Equation 11) and $\mathcal{J}_{\text{slab,avg}}$ (Equation 13) as a function of τ_{\perp} .

The Bialy (2020) model depends on the product of the separation of sources l_{\star} , the midplane density n_{H} , and the FUV cross-section σ_{FUV} . The characteristic optical depth in Equation 15 can also be written as $\tau_{\star} \equiv l_{\star} n_{\text{H}} \sigma_{\text{FUV}} = \tau_{\perp} l_{\star}/(2H)$. Thus, given the parameter τ_{\perp} for the slab model, an additional parameter entering the Bialy (2020) model is the ratio $l_{\star}/(2H)$.

For the R8-4pc model, the mean $l_{\star} = 290$ pc while $H = \Sigma_{\text{slab}}/(2n_{\text{H}}\mu_{\text{H}}m_{\text{p}}) \rightarrow 270$ pc if we use the mean total gas surface density $10.5 M_{\odot} \text{ pc}^{-2}$ for Σ_{slab} and $n_{\text{H}} = 0.57 \text{ cm}^{-3}$, which yields $x_0\tau_{\star} = 0.24\tau_{\perp}l_{\star}/H \sim 0.26\tau_{\perp}$ as the argument of $\mathcal{J}_{\text{Bialy}}$ in Equation 16. In Figure 26, we compare the slab model scaled mean intensity to $\mathcal{J}_{\text{Bialy}}$, assuming this factor (see upper axis). The value of $\mathcal{J}_{\text{Bialy}}$ is above that of $\mathcal{J}_{\text{slab,mid}}$ and $\mathcal{J}_{\text{slab,avg}}$. As noted in the text, a larger value of $l_{\star} \sim 2H$ would be required for the estimates to yield similar values.

B. MASS OF DIFFUSE IONIZED GAS COMPARED TO CLASSICAL HII REGIONS

For photoionized gas, ionization-recombination equilibrium in a given component of the ISM requires

$$Q_{\text{i,eff}} \approx \alpha_{\text{B}} n_{\text{i,rms}}^2 V_{\text{i}}, \quad (\text{B5})$$

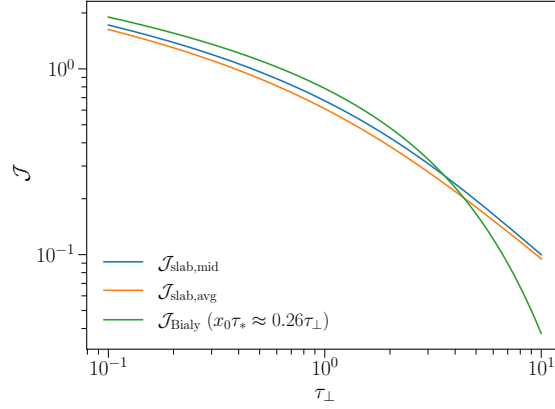


Figure 26. Comparison of the normalized FUV radiation field using different approximations as a function of τ_{\perp} . For the $\mathcal{J}_{\text{Bialy}}$ model, τ_{\perp} is defined using average values from the R8-4pc simulation such that $x_0\tau_* = 0.26\tau_{\perp}$.

where for that component $Q_{i,\text{eff}}$ is the photon rate that goes into ionization, V_i is the volume, and $n_{i,\text{rms}}$ is the rms density of ionized gas. The mass of ionized gas in that component is then

$$M_i = \mu_{\text{H}} m_{\text{H}} n_{i,\text{mean}} V_i = \mu_{\text{H}} m_{\text{H}} f_{\text{ion}} Q_{i,\text{eff}} t_{\text{rec}} \mathcal{C}_{n_e} \quad (\text{B6})$$

where $\mu_{\text{H}} m_{\text{H}} = 2.34 \times 10^{-24}$ g, $n_{i,\text{mean}}$ is the mean density, $t_{\text{rec}} = 1/(\alpha_{\text{B}} n_{i,\text{rms}})$ is the recombination time scale, and $\mathcal{C}_{n_e} \equiv n_{i,\text{mean}}/n_{i,\text{rms}} \leq 1$ is the clumping correction factor (e.g. Kado-Fong et al. 2020).

Under the assumption that all diffuse ionized gas (DIG) is photoionized, the mass ratio between DIG and classical H II regions would then be

$$\frac{M_{\text{DIG}}}{M_{\text{II}}} = \frac{(Q_{i,\text{eff}})_{\text{DIG}} t_{\text{rec,DIG}} \mathcal{C}_{n_e,\text{DIG}}}{(Q_{i,\text{eff}})_{\text{II}} t_{\text{rec,II}} \mathcal{C}_{n_e,\text{II}}} \quad (\text{B7})$$

For DIG, we assume that the source of ionizing photons is those escaping from classical H II regions which are not absorbed by dust, $Q_{i,\text{eff,DIG}} = (1 - f_{\text{dust,DIG}}) f_{\text{esc,II}} Q_i$, for Q_i the total injected photons. For H II regions, $Q_{\text{eff,i,II}} = (1 - f_{\text{dust,II}} - f_{\text{esc,II}}) Q_i$, so that

$$\frac{M_{\text{DIG}}}{M_{\text{II}}} \approx \frac{(1 - f_{\text{dust,DIG}}) f_{\text{esc,II}}}{(1 - f_{\text{dust,II}} - f_{\text{esc,II}})} \times \frac{n_{i,\text{rms,II}}}{n_{i,\text{rms,DIG}}} \times \frac{\mathcal{C}_{n_e,\text{DIG}}}{\mathcal{C}_{n_e,\text{II}}} \quad (\text{B8})$$

The escape fraction, dust absorption fraction, and clumping factors for DIG and classical H II regions can be quantified from TIGRESS and cloud-scale simulations, respectively. The first and third terms are expected to be of order unity (Kim et al. 2019; Kado-Fong et al. 2020), but $n_{i,\text{rms,II}} \gg n_{i,\text{rms,DIG}}$. We therefore conclude that $M_{\text{DIG}} \gg M_{\text{II}}$ is expected.